LIBRARY
Te Tumu Herenga
THE UNIVERSITY OF AUCKLAND

RESEARCHSPACE@AUCKLAND

http://researchspace.auckland.ac.nz

ResearchSpace@Auckland

Copyright Statement

The digital copy of this thesis is protected by the Copyright Act 1994 (New Zealand).

This thesis may be consulted by you, provided you comply with the provisions of the Act and the following conditions of use:

- Any use you make of these documents or images must be for research or private study purposes only, and you may not make them available to any other person.
- Authors control the copyright of their thesis. You will recognise the author's right to be identified as the author of this thesis, and due acknowledgement will be made to the author where appropriate.
- You will obtain the author's permission before publishing any material from their thesis.

To request permissions please use the Feedback form on our webpage. http://researchspace.auckland.ac.nz/feedback

General copyright and disclaimer

In addition to the above conditions, authors give their consent for the digital copy of their work to be used subject to the conditions specified on the Library Thesis Consent Form and Deposit Licence.

Note : Masters Theses

The digital copy of a masters thesis is as submitted for examination and contains no corrections. The print copy, usually available in the University Library, may contain corrections made by hand, which have been requested by the supervisor.

Waves in mathematical models of intracellular calcium and other excitable systems

Wenjun Zhang

A thesis submitted in fulfilment of the requirements for the degree of
Doctor of Philosophy in Applied Mathematics,
The University of Auckland, 2012.

Abstract

Oscillations in cytoplasmic calcium concentration are a crucial control mechanism in almost every cell type. Two important classes of oscillation are of particular interest: solitary and periodic waves. Both types of waves are commonly observed in physical experiments and found in mathematical models of calcium dynamics and other excitable systems. In this thesis, we try to understand these two classes of wave solutions.

We first investigate wave solutions of the canonical excitable model, the FitzHugh-Nagumo (FHN) equations. We analyze the FHN equations using geometric singular perturbation theory and numerical integration, and find some new codimension-two organizing centres of the overall dynamics. Many analytical results about the FHN model in its classical form have already been established. We devise a transformation to change the form of the FHN equations we study into the classical form to make use of the results. This enables us to show how basic features of the bifurcation structure of the FHN equations arise from the singular limit.

We then study waves of a representative calcium model. We analyze the dynamics of the calcium model in the singular limit, and show how homoclinic and Hopf bifurcations of the full system arise as perturbations of singular homoclinic and Hopf bifurcations. We compare the wave solutions in the FHN model and the calcium model, and show that the dynamics of the two models differ in some respects (most importantly, in the way in which diffusion enters the equations). We conclude that the FHN model should not uniformly be used as a prototypical model for calcium dynamics.

Motivated by phenomena seen in the FHN and calcium models, we then investigate reduction techniques for excitable systems, including the quasi-steady state approximation and geometric singular perturbation theory, and show that criticality of Hopf bifurcations may be changed when applying these reduction methods to slow-fast biophysical systems. This suggests that great care should be taken when using reduction techniques such as these, to ensure that spurious conclusions about the dynamics of a model are not drawn from the dynamics of a reduced version of the model.

Finally, we describe the class of numerical algorithms used to compute features of the detailed bifurcation sets for the FHN and calcium models, and show how these were used to locate a non-structurally stable heteroclinic connection between periodic orbits in a calcium model; this is the first time such a global bifurcation has been computed.

Acknowledgements

During the course of my Ph.D I have been extremely fortunate to receive the guidance and support of many wonderful people.

First of all, I would like to express the most sincere thanks to my supervisor Dr. Vivien Kirk for her guidance, patience, encouragement, understanding and many other aspects throughout the time when I was doing my Ph.D study.

My co-supervisor Prof. James Sneyd has always been extremely encouraging towards me and has made himself available for a lot of discussions. He also contributed a lot of useful suggestions to my thesis.

I would like to express my gratitude towards our collaborators Prof. Alan Champneys, Prof. Bernd Krauskopf, Dr. Bart Oldeman, Dr. Je-Chiang Tsai and Dr. Martin Wechselberger for providing valuable suggestions and support. I enjoyed my visit to the Department of Mathematics at the University of Sydney where part of my work was carried out.

As a platform of presenting our work, the calcium group at Auckland has weekly meetings. I would like to thank the organizers and members of this group for offering support and stimulating discussions on many aspects of my work. In addition to the above mentioned people I would also like to thank my fellow Ph.D students Wen Duan, Yousaf Habib, Emily Harvey, Amer Qureshi, Inga Wang and many others with whom I have enjoyed lengthy discussions about my research.

It is my pleasure to thank the University of Auckland for offering me a International Ph.D scholarship for the three years of my Ph.D study, the Postgraduate Research Student Support (PReSS) account for financial support towards my overseas conference travel, as well as Dr. Vivien Kirk and Prof. James Sneyd's joint Marsden Fund project funded by the Royal Society of New Zealand for supporting my overseas conference travel and supplying for one year of stipend.

Finally, I owe my loving thanks to my parents and extended family. Without their encouragement and understanding it would have been impossible for me to finish this work.

Contents

List of Figures

List of Tables

Chapter 1

Introduction

The modulation of the concentration of free intracellular calcium in the cytoplasm of a cell is a crucial control mechanism in many physiological processes, including smooth muscle contraction (Stephens, 2001; Wang et al., 2008, 2010), fluid secretion (Evans et al., 2000; Gin et al., 2007, 2009; Palk et al., 2010), cardiac electrophysiology (Franzini-Armstrong et al., 1999; Higgins et al., 2007) and neuron communication (Spergel et al., 1999; Constantin and Charles, 1999; Lee et al., 2010). Since the variation of calcium concentration plays such an important role in cell physiology, many experiments have been conducted to measure how intracellular calcium varies in different cell types (Bai and Sanderson, 2006; Perez and Sanderson, 2005b; Sneyd et al., 2004, 2006). In many of these experiments, cytoplasmic calcium concentration is stimulated to oscillate by the application of external agents like agonists and hormones. Fig. 1.1 displays a few typical examples of cytoplasmic calcium oscillation for a variety of cell types. The calcium oscillation acts as a messenger to transmit signals in the cell, with the signal being thought to be encoded in the frequency of the oscillation in many cases (Berridge and Galione, 1998; Perez and Sanderson, 2005a). Such cells interpret these frequency-encoded signals and then change their functioning according to the changes of the frequency. Hence, it is very helpful to understand in detail how and why these intracellular calcium oscillations occur.

Even though the experimental technology has advanced dramatically, it is still quite difficult and expensive to conduct a large number of experiments to measure the cytoplasmic calcium concentration inside a cell, and direct measurement of some chemicals in the cytoplasm for some cell types is still impossible. These experimental difficulties have motivated the development of other methods for determining the mechanisms underlying the intracellular calcium oscillations. In particular, mathematical modeling and model analysis have proven to be very helpful in understanding the dynamics inside the cell environment and in giving insight into the underlying mechanisms of intracellular calcium oscillations (Atri et al., 1993; Sneyd, 2005; Pate, 2005; Politi et al.,

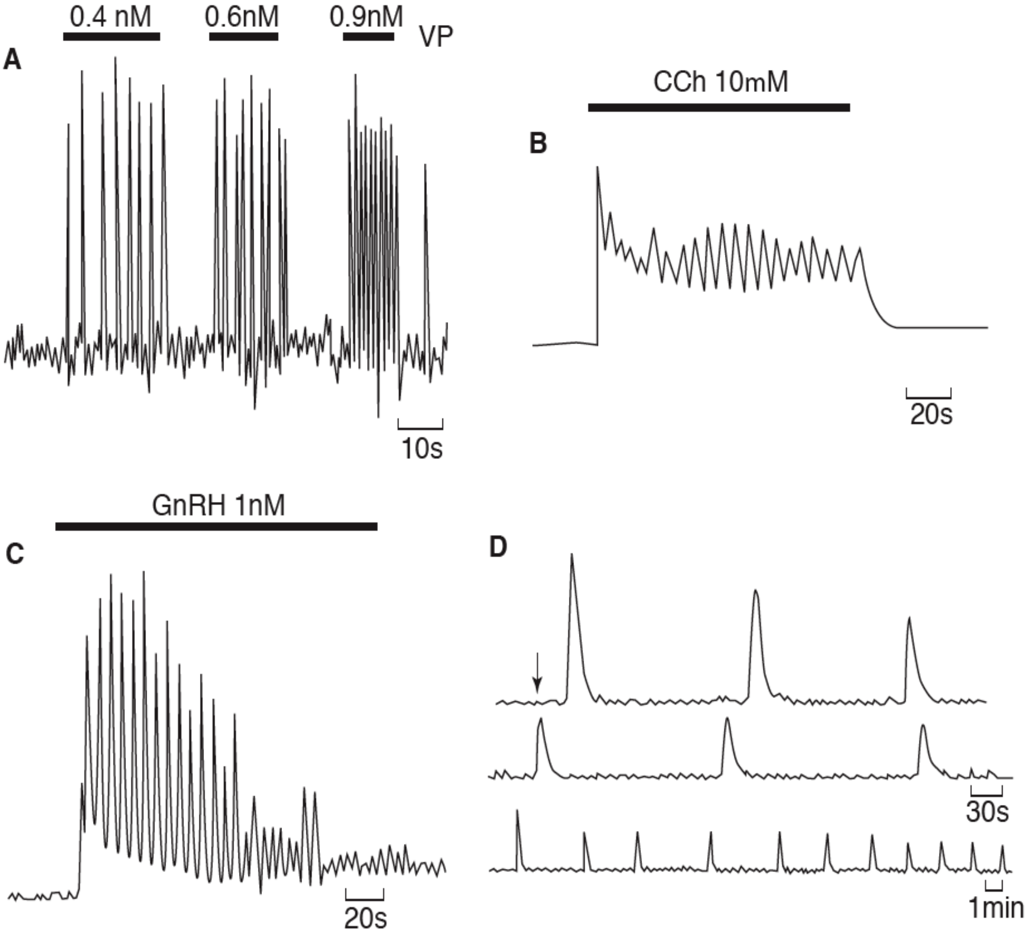

Figure 1.1: Examples of some typical oscillatory patterns of intracellular calcium in the cytoplasm for various cell types. a) Hepatocyte stimulated with three different concentrations of vasopressin (VP). b) Rat parotid gland stimulated with carbachol (CCh). c) Gonadotropes stimulated with gonadotrophin-releasing hormone (GnRH). d) Hamster egg after fertilization. Adapted from Berridge and Galione (1998).

2010).

From the perspective of constructing mathematical models of calcium dynamics, despite the fact that the mechanisms underlying calcium oscillations in one cell type may differ from the mechanisms in another cell type, different cell types may still have a similar fundamental structure and a lot of common components (Berne et al., 2004; Keener and Sneyd, 2008). These common characteristics among different cell types indicate that mathematical models describing the calcium dynamics of various cell types could share some similar structure. For example, one common feature among many cell types is that different cellular processes occur on different time scales (Perez and Sanderson, 2005b; Berridge and Galione, 1998), and we may need to use models with variables evolving on different time scales to describe the dynamics of such cell types accurately.

Two types of waves, solitary waves and periodic waves, are commonly observed in physical experiments as well as in mathematical models of calcium dynamics and other biophysical systems (Perez and Sanderson, 2005b; Wang et al., 2010; Keener and Sneyd, 2008). In this thesis we try to give insight into the dynamics of these two types of wave solutions in mathematical models. We are mainly interested in understanding waves in intracellular calcium dynamics. Our approach is to look at the wave solutions of canonical biophysical models and see how these well-understood solutions are relevant to the wave solutions of calcium dynamics. The focus is on conducting numerical and analytical studies for a number of excitable systems, including the Fitzhugh-Nagumo (FHN) equations and several representative models of intracellular calcium dynamics. We investigate the similarities and differences of wave solutions among these excitable systems. Note that the word "excitable" in excitable system has a different meaning to that used in cell electrophysiology as discussed below, i.e., an "excitable system" is not necessarily related to an "excitable cell".

1.1 Basic cell physiology

In this section we introduce some basic physiological structures common to most cell types, and describe the dynamics of these common components with mathematical equations. Other relevant mathematical modeling assumptions are also discussed.

1.1.1 Fluxes

A cell can be considered to consist of two main components, namely the cell cytoplasm and an internal compartment such as the endoplasmic reticulum (ER). For different cell types, the internal compartment can be of different types. For example, the main internal compartment in smooth muscle cells is the sarcoplasmic reticulum (SR) (Stephens, 2001). However, the calcium uptake and release mechanisms of these different types of internal compartments are more or less the same (Lodish et al., 2003; Toyoshima et al., 2000). Therefore, in this thesis we assume that the internal compartment inside the cell is the ER. The ER is separated from the rest of the cell by the ER membrane. The intracellular space is surrounded by a plasma membrane. Both of these membranes are impermeable to calcium.

At steady state, the concentration of calcium in the cell cytoplasm is quite low while in the extracellular space and in the ER the concentration of calcium is much higher. These concentration differences are maintained partly by calcium ATPase pumps, which use the energy stored in adenosine triphosphate (ATP) to pump calcium

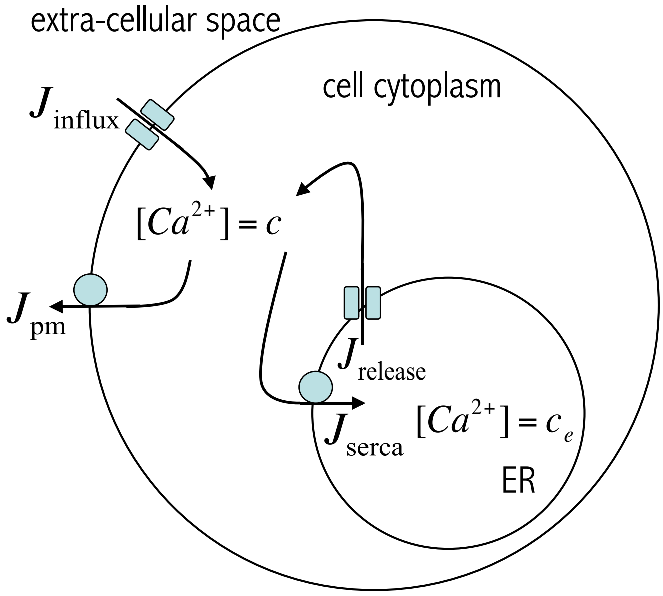

Figure 1.2: Schematic diagram showing the major fluxes involved in the variation of intracellular calcium.

in the cell cytoplasm against the steep gradient into the ER or out of the cell.

Calcium goes into the cell cytoplasm in two main ways: influx from the extracellular medium through calcium channels on the plasma membrane and release from the ER through calcium channels on the ER membrane.

The calcium channels on the plasma membrane can be of several different types. For instance, voltage-dependent channels open in response to depolarization of the plasma membrane potential, and receptor-operated channels open in response to the binding of external chemical agents to the plasma membrane. Voltage-dependent calcium channels are of great importance for certain cell types, e.g., cardiac cells and neurons (Sneyd et al., 2004; Lee et al., 2010). These kinds of cells are usually referred to as electrically excitable cells, while other cell types are referred to as non-excitable cells since they are not sensitive to the variation of potential of the plasma membrane. For the intracellular calcium models considered in this thesis, we focus on the calcium dynamics of non-excitable cells, and omit considerations of the more complicated voltage dependent plasma membrane calcium channels, concentrating instead on the complexity of calcium exchange between the cell cytoplasm and the internal compartments. See Keener and Sneyd (2008), Falcke (2004), Lee et al. (2010) for more detailed information about the properties of voltage-dependent calcium channels on the plasma membrane.

There are calcium channels dispersed across the ER membrane as well as the plasma membrane, and calcium can flow down the gradient from the internal compartment to the cell cytoplasm through the channels when they are open. The channels on the ER membrane are of two main types, both receptor-operated, namely the inositol $(1, 4, 5)$-trisphosphate (IP_3) receptor and the ryanodine receptor.

IP_3 receptors are mostly found in non-muscle cells, e.g., pancreatic acinar cells (LeBeau et al., 1999; Giovannucci et al., 2000) and parotid acinar cells (Gin et al., 2007) and they are sensitive to the chemical IP_3. The binding of an extracellular agonist such as a hormone to a receptor in the plasma membrane can lead to a chain reaction which produces the chemical IP_3, which then diffuses through the cell cytoplasm and binds to the IP_3 receptors on the ER membrane. The IP_3 receptor opens in response to the binding of IP_3 and releases calcium from the internal compartment to the cell cytoplasm. The open probabilities of IP_3 receptors are also modulated by the cytoplasmic calcium concentration. At relatively low concentrations, intracellular calcium increases the open probabilities of the the IP_3 receptors to allow more calcium coming from the ER; this process is usually referred to as calcium-induced calcium release, or CICR. At relatively high concentrations, intracellular calcium decreases the open probabilities of the IP_3 receptors to prevent calcium coming from the ER. The calcium ATPase pumps then pump the calcium out of the cell cytoplasm to lower the intracellular calcium concentration. When the intracellular calcium concentration is low enough, then the IP_3 receptors are stimulated to open again and calcium is again released from the internal compartment to increase the intracellular calcium concentration. This mechanism allows the intracellular calcium concentration to oscillate inside the cell cytoplasm.

The other type of receptor on the ER membrane, i.e., the ryanodine receptor, is mostly found in muscle cells, e.g., smooth muscle cells in the lung (Bai et al., 2009; Stephens, 2001; Wang et al., 2008). Ryanodine receptors have a similar calcium-induced calcium release mechanism as the IP_3 receptors, with intracellular calcium both activating and inhibiting the calcium release through the ryanodine receptors from the internal compartment at different rates. Since the IP_3 receptor and ryanodine receptors share a similar calcium releasing mechanism, we will not distinguish between these two types of receptors in this thesis.

The major fluxes involved in the variation of intracellular calcium are shown in the schematic diagram shown in Fig. 1.2. The fluxes J_{serca} and J_{pm} represent the calcium pumped out of the cell cytoplasm by the ATPase pumps into the internal compartment and the extracellular space, respectively. The fluxes J_{release} and J_{influx} represent the calcium flowing down the concentration gradient into the cell cytoplasm through open channels on the ER and plasma membranes, respectively.

The calcium models studied in this thesis focus on the four major fluxes going into and out of the cell cytoplasm. There are other fluxes which are important for the control of intracellular calcium for some cell types. For example, calcium exchange between the cell cytoplasm and mitochondria is thought to be another important mechanism for controlling intracellular calcium for neurons (Colegrove et al., 2000; Grubelnik et al., 2001); and the use of sodium-calcium ($Na^+ - Ca^{2+}$) exchangers to move calcium from the cell cytoplasm to the extracellular medium plays a significant role in the modulation of cytoplasmic calcium in cardiac cells (Bers, 2002; Winslow et al., 2005). More detailed descriptions of various fluxes related to cytoplasmic calcium can be included for more realistic models. See Keener and Sneyd (2008) for an extensive description of a variety of intracellular calcium fluxes.

1.1.2 ODEs model assumptions and model structure

In some cell types under some circumstances, intracellular oscillations occur practically uniformly across the cell. In such cases, measurement of the concentration of calcium at a point of the cytoplasm gives more or less the same time series, regardless of which point is used. For these cell types, we can assume that the variation of calcium concentration is homogeneous throughout the cell cytoplasm. Specifically, we denote by c the concentration of free intracellular calcium and note that $c = c(t)$ has no spatial dependence, since intracellular variation occurs uniformly. Similarly, we assume that there is homogeneous distribution of calcium inside the ER, and let $c_e = c_e(t)$ denote the concentration of calcium inside the ER.

The assumption of homogeneous variation throughout the cell is quite common in modeling the dynamics of a range of cell types; models that use this assumption are usually referred to as well-mixed models or point cell models (Falcke, 2004; Keener and Sneyd, 2008). Since the intracellular calcium variation in such mathematical models does not have any spatial dependence, we can use a system of ordinary differential equations (ODEs) to describe the change of calcium concentration inside the cell cytoplasm and the ER.

Ordinary differential equations for the variables c and c_e are derived from the conservation of total calcium inside the whole cell. Usually it is assumed that the volumes of the cell cytoplasm and the internal compartment are constant; then the amount of calcium is directly proportional to the calcium concentration. Therefore, the conservation of total calcium of the entire cell can be translated into the conservation of total calcium concentration of the cell, which means the rate of change of total calcium concentration inside the cell is equal to the net flux of calcium across the cell plasma membrane.

In order to give an accurate description of the calcium dynamics inside the cell, we need to take into account the fact that the cytoplasmic volume is different from the ER volume. In particular, the volume of the ER is less than that of the cytoplasm which means the calcium exchange between the cytoplasm and the ER leads to a greater concentration change in the ER than it does in the cytoplasm. A parameter γ is used to denote the ratio of the cytoplasmic volume to the volume of the ER. Furthermore, for non-excitable cell types, the calcium exchange across the plasma membrane occurs much slower than the calcium exchange across the ER membrane. Another parameter ε is used to denote the separation of time scales of these two exchange processes.

Based on all the assumptions given above, we can write down a pair of ordinary differential equations to model the change of calcium concentration of the cell cytoplasm and the ER:

$$\begin{aligned} \frac{dc}{dt} &= J_{\text{release}} - J_{\text{serca}} + \varepsilon(J_{\text{influx}} - J_{\text{pm}}), \\ \frac{dc_e}{dt} &= \gamma(J_{\text{serca}} - J_{\text{release}}). \end{aligned} \tag{1.1}$$

We note that the assumption that ε is small works for non-excitable cells but not for excitable cells. In electrically excitable cells like cardiac cells, the calcium exchange through the channels on the plasma membrane plays a more important role than the calcium exchange inside the cell (Franzini-Armstrong et al., 1999).

An important feature of the calcium dynamics of non-excitable cells, namely calcium entering and leaving the cell across the cell membrane relatively slowly, motivates us to treat the total amount of calcium in the cell as a convenient slow variable. This is a common practice for analyzing the calcium dynamics of non-excitable cell types (Sneyd et al., 2004). Part of the reason is that the separation of time scales is known to introduce complex dynamics, including canards solutions (Benoit et al., 1986; Szmolyan and Wechselberger, 2001; Harvey et al., 2010, 2011), and explicit identification of the slow variable(s) makes it much easier to analyze the complicated dynamics. We therefore follow a standard procedure to introduce a new variable $c_t = \frac{c_e}{\gamma} + c$ and rewrite equations (1.1) with c_t replacing c_e:

$$\begin{aligned} \frac{dc}{dt} &= J_{\text{release}} - J_{\text{serca}} + \varepsilon(J_{\text{influx}} - J_{\text{pm}}), \\ \frac{dc_t}{dt} &= \varepsilon(J_{\text{influx}} - J_{\text{pm}}), \end{aligned} \tag{1.2}$$

where the new variable c_t represents the total concentration of calcium across the entire cell.

1.1.3 PDEs model assumptions and model structure

Equations (1.1) and (1.2) are formulated under the assumption that the cell is well-mixed, which means that variation of calcium concentration occurs uniformly throughout the cell. In some cell types, however, intracellular calcium oscillations take the form of a wave moving across the cell; these fluctuations are referred to as intracellular waves. Inclusion of calcium diffusion terms is necessary to model and analyze such spatially distributed calcium fluctuations.

A cell is a three-dimensional object physically. A more precise representation of a physical cell would be obtained by treating the cell as a three-dimensional structure comprised of two interconnected domains, namely the cell cytoplasm and the ER. Because of the intricate geometry of the ER inside the inhomogeneous cytoplasmic space, these types of precise models are usually far too complex to make progress and give useful information.

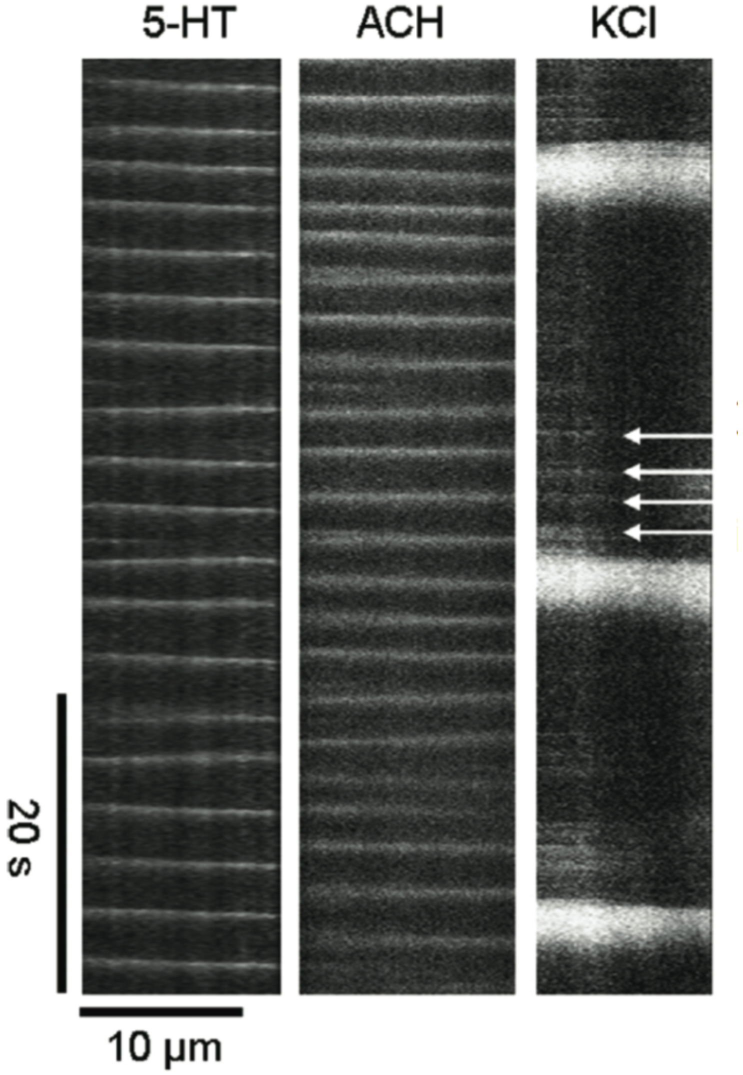

Figure 1.3: The experimental results of line scans from the longitudinal axes of single mouse airway smooth muscle cells with stimulation with various different chemicals. One can observe that the variation of calcium concentration does not occur uniformly along the longitudinal axis of the cell, and the variation of calcium concentration displays little curvature. The figure is adapted from Perez and Sanderson (2005a).

In some cell types, intracellular calcium waves measured in experiments exhibit very little curvature, and thus can effectively be regarded as one-dimensional spatial waves. One example of these experimentally-observed intracellular calcium waves is shown in Fig. 1.3. Observations of these almost one-dimensional spatial waves in experiments motivate us to use homogenization techniques (Goel et al., 2006; Keener and Sneyd, 2008) to derive a simplified model in which a cell is considered to be an essentially one-dimensional object. Specifically, we assume that the geometry of the cell is a long thin cylinder with boundary fluxes (J_{influx} and J_{pm}) on the cylindrical wall. It is also assumed that the intracellular space is isotropic and homogeneous, and that c and c_e coexist at every point in the intracellular space. A third assumption is that diffusion of calcium is rapid over short distances with a constant diffusion coefficient D.

Since the cross-section transverse to the longitudinal axis of the cell is small and the diffusion of calcium is fast, we expect that the calcium concentration should be nearly the same at each point on a cross-section, varying only slightly from its average value. Local variations are smoothed out quickly and it is sufficient to know the average calcium concentration on each cross-section. Therefore, the equations of mean field (i.e., average calcium concentration) can be derived to describe the evolution of the average calcium concentration value along the longitudinal axis of the cell.

The calcium concentration is also affected by the fluxes across the cylindrical wall. As shown in Goel et al. (2006) and Keener and Sneyd (2008), homogenization techniques can be used to take account of the boundary conditions while reducing the cylinder to a one-dimensional domain (a line segment) with no flux boundary conditions at the ends. We then end up with the following equations to model the variation mechanisms of intracellular calcium concentration:

$$\begin{aligned}\frac{\partial c}{\partial t} &= D\frac{\partial^2 c}{\partial x^2} + J_{\text{release}} - J_{\text{serca}} + \varepsilon(J_{\text{influx}} - J_{\text{pm}}),\\ \frac{\partial c_t}{\partial t} &= \varepsilon(J_{\text{influx}} - J_{\text{pm}}) = \frac{\partial c}{\partial t} + \frac{1}{\gamma}\frac{\partial c_e}{\partial t} - D\frac{\partial^2 c}{\partial x^2},\end{aligned} \tag{1.3}$$

where x represents the one-dimensional spatial variable along the longitudinal axis of the cell and c_t represents the total calcium which changes slowly with respect to time. These two equations are typically supplemented with further ODEs modelling other variation mechanisms inside a cell, e.g., IP_3 receptor dynamics; see Keener and Sneyd (2008) and Champneys et al. (2007) for more details. Note that the relation $\frac{\partial c_t}{\partial t} = \frac{\partial c}{\partial t} + \frac{1}{\gamma}\frac{\partial c_e}{\partial t} - D\frac{\partial^2 c}{\partial x^2}$ indicates that the diffusion term $D\frac{\partial^2 c}{\partial x^2}$ affects the evolution of the slow variable c_t as well as the fast variable c. In summary, the dynamics of calcium variation with spatial diffusion inside a cell can be modelled by a reaction-diffusion system of partial differential equations.

Although it seems that assumptions imposed to simplify the complex calcium dynamics inside a cell are rather strong, the wave solutions of the resulting models can match quite well with experimental data. Fig. 1.4 shows a comparison between a numerically computed calcium wave and a calcium wave observed experimentally. The similarity between the panels demonstrates that the simplified model is useful.

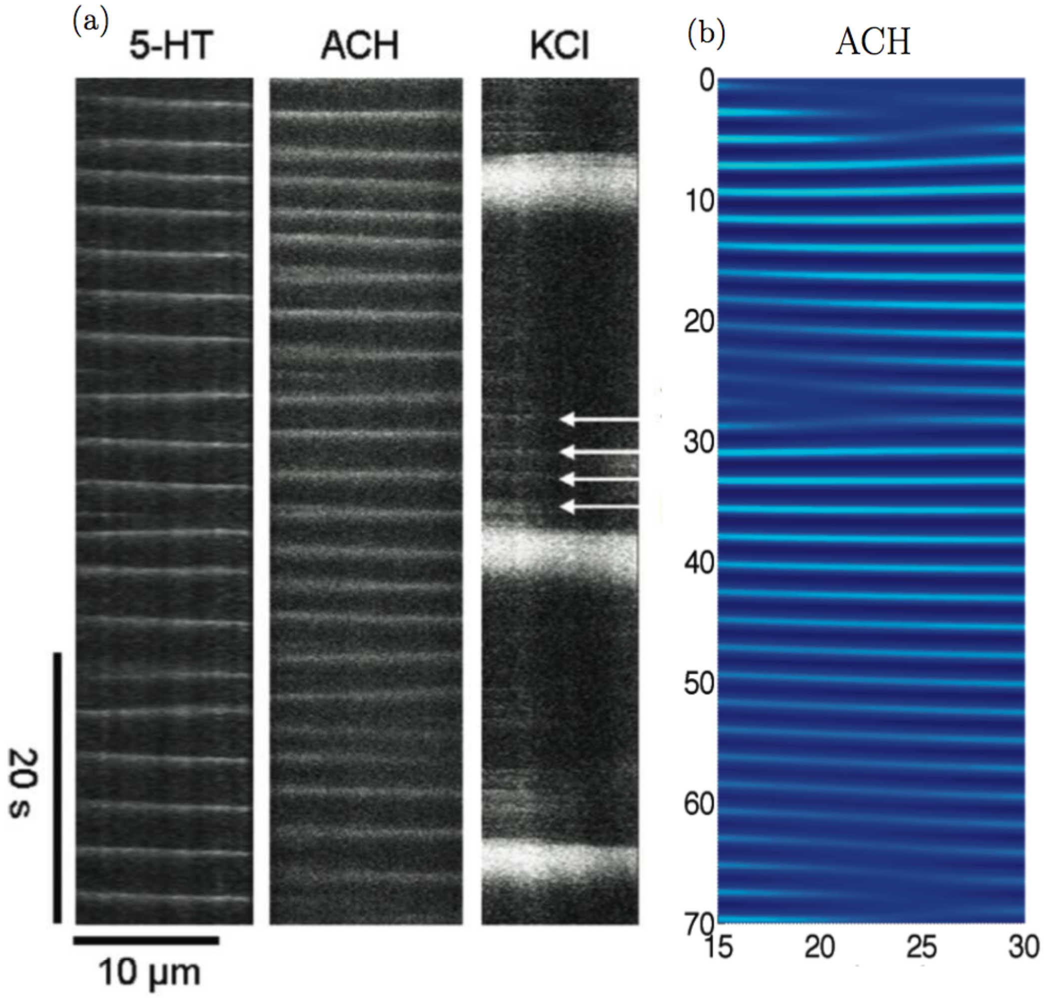

Figure 1.4: Experimental results (panel (a)) and the numerical simulation results (panel (b)), adapted from Wang et al. (2010). The comparison between the results shows that the simplified model is effective at producing a calcium wave solution similar to the experimental data.

1.1.4 Different types of calcium waves

As mentioned before, solitary waves and periodic waves of calcium concentration are commonly observed in experiments. The mechanisms underlying these two classes of calcium waves are discussed further in this section.

It is widely believed that when the underlying reaction kinetics of calcium is stationary, intracellular calcium waves are driven by the diffusion of calcium between calcium release sites (Rottingen and Iversen, 2000; Rooney and Thomas, 1993). According to this hypothesis, the calcium released from one group of release sites diffuses to nearby release sites and stimulates further calcium release from them. Repetition of such a

CICR process leads to aggregation of calcium at this neighborhood of the cell. The aggregation of calcium diffuses through the cell giving rise to an isolated wave front of high calcium concentration. The propagation of the front is mostly maintained by the active release of calcium from the ER via the CICR mechanism. This kind of wave is usually referred to as a solitary wave.

However, when the underlying calcium reaction kinetics are oscillatory, i.e., there is a stable limit cycle of calcium release and recovery in the absence of diffusion, a different mechanism is thought to underlie calcium wave propagation (Rottingen and Iversen, 2000; Rooney and Thomas, 1993). Specifically, all the points of the cell are oscillating in the same periodic manner and the difference among the points is that they are oscillating with a different phase. Each point can be regarded as a local oscillator, and calcium diffusion serves to synchronize these oscillators along the cell. Intracellular calcium waves propagating by this kinematic mechanism are usually referred to as periodic waves.

1.2 Thesis outline

In this thesis we try to give insight into solitary and periodic wave solutions in models of intracellular calcium dynamics, specifically in non-excitable cells. To this end, we perform detailed numerical experiments on various calcium models and the FHN system, and examine singular limits of the models to investigate the origin of the common features of these models (specifically, the so-called CU bifurcation structure first discovered in Champneys et al. (2007)). This work on specific models then inspires more general theoretical work on the analysis of reduction methods for biophysical models and some detailed numerical work on implementing a new algorithm to find global bifurcations involving saddle periodic orbits.

In chapter 2, we examine the CU structure of wave solutions in the FHN equations, and present some new numerical and analytical results about wave solutions to this canonical excitable system. We discuss how the solitary wave solution and the periodic wave solution can be understood by exploiting the slow-fast nature of the FHN system.

In chapter 3, we study a simplified model that captures the essential features of a wide range of realistic calcium dynamical models. Similar to the analysis given in chapter 2, we perform a bifurcation analysis of this representative calcium model.

In chapter 4, we discuss the similarities and differences between the wave solutions of the FHN model and the representative calcium model discussed in chapter 3. Parts of the work presented in chapters 3 and 4 have been done in collaboration with J. C. Tsai, V. Kirk and J. Sneyd and a manuscript has been submitted for publication (Tsai et al., 2012).

In chapter 5, we investigate techniques commonly used to reduce the dimension of mathematical models of biophysical systems and show that some aspects of the dynamics may be changed when these reductions techniques are applied. Parts of the work presented in this chapter have been done in collaboration with V. Kirk, J. Sneyd and M. Wechselberger, and have been published in Zhang et al. (2011).

In chapter 6, we outline a numerical scheme which was used to obtain detailed numerical information about one of our calcium models. The numerical scheme was developed by Krauskopf and Riess (2008), but the first ever implementation of the method to find a specific global bifurcation (i.e., a so-called codimension-one PtoP heteroclinic cycle) was done for a calcium model as part of this thesis. The work presented in this chapter has been done in collaboration with B. Krauskopf and V. Kirk, and a manuscript has been accepted for publication (Zhang et al., 2012).

In chapter 7, we draw some conclusions and discuss some possibilities for future work.

For convenience, equations and parameters of complicated systems are presented in Appendix A, and a list of glossary is also included at the end of the thesis.

Chapter 2

Wave solutions in the FHN model

In this chapter, wave solutions of a canonical excitable system, the FitzHugh-Nagumo (FHN) equations, are studied. The FHN equations are a system of reaction-diffusion equations used to model the variation of membrane potential of a cell. The chapter is structured as follows. In sections 2.1 and 2.2, we briefly discuss the history and the formulation of the FHN equations. Some relevant known numerical results are introduced in section 2.3, while some new numerical results are displayed in section 2.4. The numerical results motivate us to analyze the FHN equations in the singular limit. Both existing results and new results from the analysis of the singular limit are discussed in sections 2.5 and 2.6. We compare the numerical results with analytical results for the FHN equations in section 2.7.

2.1 History of FHN equations

The FHN model is a simplification of a more realistic biophysical model, the Hodgkin-Huxley (HH) equations. Here we give a brief summary of the physiological background of the HH equations; see Hodgkin and Huxley (1952a,b,c,d) and Keener and Sneyd (2008) for more detailed information about derivation of the HH equations.

For some cell types, like cardiac cells and most neuron cells, if sufficiently strong stimulating currents are applied to the cell for a short period of time, the membrane potential of the cell goes through a large excursion before slowly recovering back to its steady state value over a relatively long period of time. One of the advantages of this electrical wave signaling process with a pulsing membrane potential is that the cell responds to a stimulus either with a significantly large increase of membrane potential or not at all. Therefore, a stimulus of sufficiently large amplitude is reliably distinguished from background noise.

The generation and propagation of electrical waves have been extensively studied by physiologists, with one of the landmark studies being the work of Alan Hodgkin and Andrew Huxley (Hodgkin and Huxley, 1952a,b,c,d), who developed the first quantitative model (HH equations) of electrical waves moving along a squid giant axon. Although the HH equations were originally used to explain the ionic mechanisms underlying the initiation and propagation of action potentials in the giant axon of a squid nerve cell, the ideas have been extended and applied to the dynamics of a wide range of other cell types.

The squid nerve cell has two important levels of membrane potential: the resting potential, which is the value the membrane potential maintains as long as nothing perturbs the cell, and a higher value called the threshold potential. For a typical squid neuron, the resting potential is around -70 millivolts and the threshold potential is around -55 millivolts. Synaptic inputs to a neuron cause the membrane to depolarize or hyperpolarize, i.e., they cause the membrane potential of the neuron to rise or fall. Action potentials are triggered when a sufficient amount of depolarization accumulates to bring the membrane potential above the threshold value. When an action potential is triggered, the membrane potential abruptly shoots upward to an elevated level, often reaching as high as 100 millivolts. The membrane potential stays at a plateau of the elevated level for a while then shoots downward rapidly, often ending below the resting potential level. The membrane potential remains for a long period of time below the resting level until returning to the resting potential; this process is usually referred to as after-hyperpolarization. Therefore, the profile of the action potential can be divided into four parts: (A) a stimulus causes the membrane potential to rise above the threshold potential to induce a fast increase of the voltage; (B) the potential decreases slowly on a plateau of high voltage; (C) the membrane potential shoots back below the resting level; (D) slow recovery of the membrane potential to the resting potential. A typical time series of an action potential is depicted in Fig. 2.1.

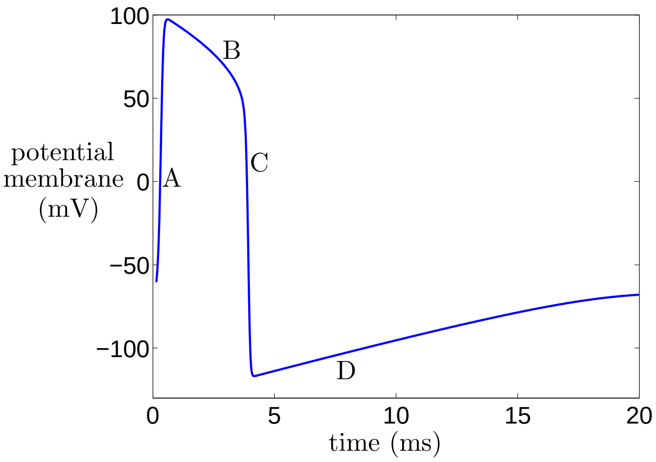

Figure 2.1: A typical time series of an action potential in the HH equations.

The HH equations model the underlying kinetic mechanism of the action potential based on the physiology of the squid nerve axon, and include many nonlinear terms to describe various ionic currents in detail. FitzHugh and Nagumo (Fitzhugh, 1961; Nagumo et al., 1962) independently showed how the essential ingredients of the generation of action potentials could be extracted into a simpler model on which mathematical analysis techniques could be applied more easily. This simplified FHN model turned out to be of great theoretical interest; it contributed enormously to the study and understanding of excitable systems.

2.2 Formulations of the FHN equations

The FHN equations is a dynamical system modelling the generation of the action potential. The two dependent variables evolve on different time scales to capture the excitable feature of the HH equations. The fast variable, u, represents the membrane potential in the HH equations and has a cubic nonlinear term. The other variable, w, is usually referred to as the recovery variable, and provides a slower negative feedback to the membrane potential. The conduction process of the variation of membrane potential along the neuron is modelled by a spatial diffusion term.

The FHN equations can be written in the following form

$$\begin{aligned} \frac{\partial u}{\partial t} &= D_c \frac{\partial^2 u}{\partial x^2} + f(u) - w + p, \\ \frac{\partial w}{\partial t} &= \varepsilon(u - \gamma w), \end{aligned} \tag{2.1}$$

where x is a one-dimensional spatial variable, t represents time, and the diffusion coefficient is denoted by D_c. The nonlinear reaction function f is typically specified as a cubic polynomial relation as follows:

$$f(u) = u(u-1)(a-u),$$

where $\alpha \in (0,1)$. There are other choices for the function f, such as a piecewise linear relation, which is considered in the McKean model (Mckean, 1970; Keener and Sneyd, 2008) with the form:

$$f(u) = \begin{cases} -u & \text{for } u < \frac{\alpha}{2}, \\ u - a & \text{for } \frac{\alpha}{2} < u < \frac{\alpha+1}{2}, \\ 1 - u & \text{for } u > \frac{\alpha+1}{2}. \end{cases}$$

Different forms of the function f are usually chosen to have a similar shape to the cubic polynomial given above; this choice ensures that excitability will be present in the model. The parameter ε represents the separation of time scales between the fast change of the membrane potential compared with the slow variation of the recovery variable, and γ is also a scale parameter.

The level of external applied current is represented by p. In the original formulation of the FHN system (Fitzhugh, 1961; Nagumo et al., 1962), the parameter p mimicking the current applied to the nerve axon in the HH equations was included in the equations. However, it is common to study the FHN system under the assumption that the applied current is zero, and many analytical results have been established in this case (Jones, 1984; Jones et al., 1991; Krupa et al., 1997). In section 2.5.2, we show that there is a coordinate and parameter transformation that converts equations (2.1) into an equivalent form with no applied current, which means that results already established for the FHN equations with no applied current can be reformulated for the FHN equations (2.1) with the applied current term. More details about the derivation of the FHN model can be found in Fitzhugh (1961) and Nagumo et al. (1962). Equations (2.1) were studied in Champneys et al. (2007) with parameter values given as follows:

$$D_c = 5.0, \quad \alpha = 0.1, \quad \gamma = 1.0, \quad \varepsilon = 0.01, \tag{2.2}$$

and we use the same parameter values to begin our analysis of the model equations (2.1).

Stable solitary and periodic wave solutions can be observed in numerical solutions to the FHN equations (2.1). Panel (a) of Fig. 2.2 shows a solitary wave solution found for $p = 0.05$. To obtain this picture, equations (2.1) were integrated on a spatial domain of 1000 units of length with no flux boundary conditions at both ends of the domain. The numerical integration was implemented with a Crank-Nicolson scheme (Crank and Nicolson, 1947). Different grid sizes were used (ranging from 2000 to 5000 grid points on the domain) but the integration results were very similar for different choices of the grid. The initial condition of u was specified as follows: the rightmost 20 unit length of the spatial domain was set at $u^* + 1$, with $u = u^*$ elsewhere, where u^* is the equilibrium value of u of equations (2.1), obtained by setting all derivatives in equations (2.1) to zero and solving for u and w. The variable w was set to its equilibrium value w^* initially across the entire domain. The wave shown in panel (a) of Fig. 2.2 travels to the left in the domain with a wave speed approximately 1.32 units of length per time unit.

By contrast when $p = 0.2$, numerical integration yields a periodic wave solution. The profile of this periodic wave solution is depicted in panel (b) of Fig. 2.2. As time evolves, this solution travels to the left at a wave speed of approximately 1.28 units of length per time unit.

These two types of wave solutions are of particular interest because experiments in excitable media suggest these patterns are commonly observed (Keener and Sneyd, 2008) and can be obtained by varying the external current applied to the media, just as

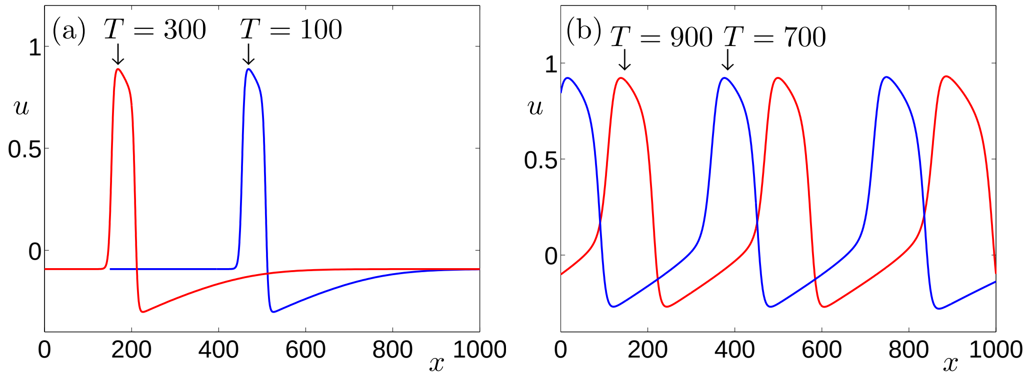

Figure 2.2: (a) A stable solitary wave solution to equations (2.1) at $p = 0.05$ obtained by direct numerical integration. The solution is plotted in blue and red at times T=100 and T=300, respectively. (b) A periodic wave solution to equations (2.1) at $p = 0.2$ obtained by direct numerical integration. The solution is plotted in blue and red at times T=700 and T=900, respectively. The solitary and periodic travelling wave solutions correspond to homoclinic and periodic solutions, respectively, in the travelling wave coordinates.

observed from numerical integration of the FHN model. Although numerical integrations can give some understanding of the behaviour of solutions to the FHN equations (2.1), a more thorough understanding of wave solutions requires a detailed study of the bifurcations occurring in this system.

Since we are mainly interested in wave solutions of the system, it is convenient to analyze the system in travelling wave coordinates. Specifically, we change to travelling wave coordinates by introducing a new independent variable $\xi = x + st$, where s represents the wave speed. Then all the partial derivatives become ordinary derivatives with respect to the new variable ξ:

$$\frac{\partial u}{\partial t} = s\frac{du}{d\xi}, \quad \frac{\partial^2 u}{\partial x^2} = \frac{d^2u}{d\xi^2}, \quad \frac{\partial w}{\partial t} = s\frac{dw}{d\xi},$$

and equations (2.1) become:

$$\begin{aligned} s\frac{du}{d\xi} &= D_c\frac{d^2u}{d\xi^2} + f(u) - w + p, \\ s\frac{dw}{d\xi} &= \varepsilon(u - \gamma w). \end{aligned}$$

This can be rewritten as a system of three ordinary differential equations by introducing a new variable v:

$$\begin{aligned} \frac{du}{d\xi} &= v, \\ \frac{dv}{d\xi} &= \frac{1}{D_c}(sv - u(u-1)(\alpha - u) + w - p), \\ \frac{dw}{d\xi} &= \frac{\varepsilon}{s}(u - \gamma w). \end{aligned} \tag{2.3}$$

It is straightforward to see that solitary and periodic travelling wave solutions of the PDEs system (2.1) correspond to homoclinic and periodic solutions, respectively, in the ODEs system (2.3). However, one thing to keep in mind is that such an approach does not give any information about the stability of the wave solutions of the original reaction-diffusion partial differential equations. The stability of the wave solutions can be determined by analyzing the partial differential equations (Evans and Feroe, 1977; Jones, 1984; Romeo and Jones, 2003); we will not discuss the stability of the wave solutions in detail in this thesis.

2.3 Preliminary analysis of the FHN model in travelling wave coordinates

A partial bifurcation analysis of equations (2.3) with parameter values specified in (2.2) is given in Champneys et al. (2007). This section summarizes some relevant results from Champneys et al. (2007).

We would like to find the locations of homoclinic and periodic solutions in the FHN system, i.e., we try to find the homoclinic and Hopf bifurcation curves in the (p, s) parameter plane. This can be done by using the numerical bifurcation detection and continuation software AUTO (Doedel et al., 2007).

We can trace out the Hopf and homoclinic bifurcation curves in a standard way, as outlined in the following steps. First we specify an equilibrium point of the system either analytically or numerically for certain parameter values, then follow the equilibrium as one system parameter is varied, until a Hopf bifurcation is detected. AUTO can both continue this Hopf bifurcation by varying two system parameters to trace out the Hopf bifurcation curve in the parameter plane and continue a periodic solution from the Hopf bifurcation in one parameter. The period of the periodic solution grows exponentially as the periodic solution approaches a homoclinic bifurcation. After detecting such a homoclinic bifurcation, we can make use of the HomCont routine implemented in AUTO to continue the homoclinic solution in two parameters to trace out the homoclinic bifurcation curve on the parameter plane.

Applying the procedure to the FHN equations (2.3), we can reproduce the partial bifurcation set for equations (2.3) first published in Champneys et al. (2007); see panel (a) of Fig. 2.3. The bifurcation set includes a U-shaped curve of Hopf bifurcations and a C-shaped curve of homoclinic bifurcations in the (p, s) parameter plane.

Some useful information about equations (2.1) can be obtained from the bifurcation set. For instance, homoclinic solutions exist in the interval of the applied current $p \in (-0.0034, 0.0703)$ and the onset of periodic solutions (i.e., Hopf bifurcations) occurs in the interval $p \in (0.0703, 0.5423)$. In terms of the original partial differential equations

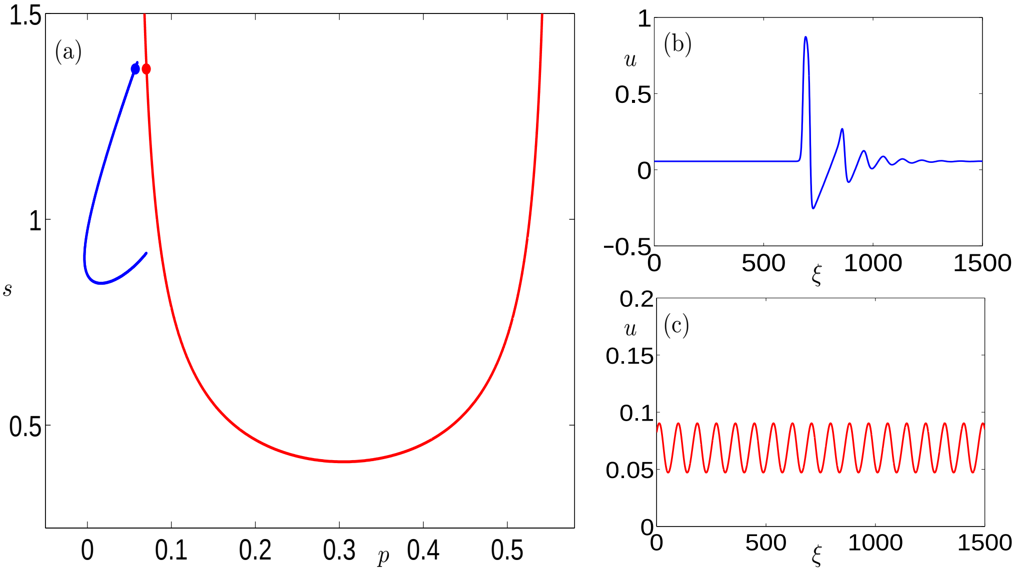

Figure 2.3: (a) Partial bifurcation set for equations (2.3) for the parameter values given in (2.2), showing the U-shaped curve of Hopf bifurcations in red and C-shaped curve of homoclinic bifurcations in blue. The dots mark the positions corresponding to the time series shown in panels (b) and (c). (b) Time series for a homoclinic orbit near the top of the C-shaped curve at $(p, s) = (0.057, 1.37)$. (c) Time series for a nearby periodic orbit at $(p, s) = (0.069, 1.37)$. This figure is reproduced from Champneys et al. (2007).

(2.1), the numerical results show that solitary wave solutions exist in the interval $p \in (-0.0034, 0.0703)$.

The numerical results shown in Fig. 2.3 give rise to several questions. For example, we would like to know why the homoclinic bifurcation and Hopf bifurcation curves are C-shaped and U-shaped in the parameter plane, respectively, and how the C-shaped homoclinic curve terminates near its end points. In order to give insight into such questions, we need more detailed information about the bifurcation structure of equations (2.3).

2.4 Detailed numerical bifurcation analysis of the FHN system

In this section, we look at the bifurcation set for equations (2.3) in more detail. In particular, we find some new codimension-two bifurcation points that are organizing centres of the bifurcation set in the (p, s) parameter plane, with complicated bifurcation structure occurring near these organizing centres.

A detailed bifurcation set for equations (2.3) was obtained with AUTO and is shown in Fig. 2.4. The different features of this figure are described below.

According to the numerical computation, the Hopf bifurcation changes its criticality

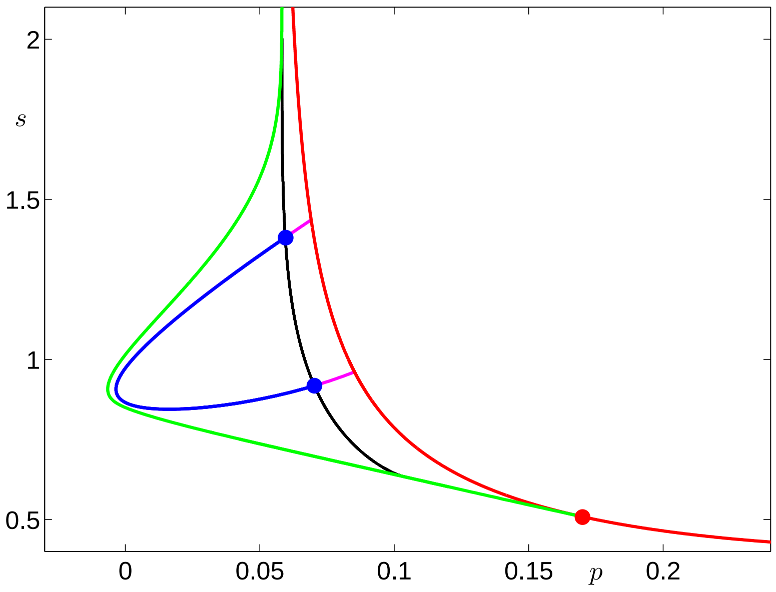

Figure 2.4: Partial bifurcation set for the FHN equations (2.3) for $\varepsilon = 0.01$. The C-shaped curve in blue is the locus of homoclinic bifurcations. The right-most red curve is part of the U-shaped Hopf bifurcation curve. On this curve, the large red dot marks a degenerate Hopf bifurcation. The green curve emanating from the degenerate Hopf bifurcation point denotes a branch of saddle-node bifurcations of periodic orbits and it connects to another degenerate Hopf point not shown in this figure. The black curve denotes a locus of tangency of the heteroclinic connection from a periodic orbit to the equilibrium. The magenta curve very close to the blue homoclinic curve is the locus of codimension-one heteroclinic connections from the equilibrium to the periodic orbit. The curve terminates on the U-shaped Hopf curve, since the heteroclinic connection from the equilibrium to the periodic orbit is generic (of codimension zero) inside the U-shaped Hopf curve. The two large blue dots mark the intersection points between the black curve and the magenta curve; these points are called EP1t points in Champneys et al. (2007).

as the parameter p varies, and thus we expect to find some codimension-two degenerate Hopf bifurcation (Bautin) points (Bautin, 1975, 1977) along the Hopf bifurcation curve. These codimension-two points can be located in the (p, s) plane numerically by using bifurcation analysis software packages, e.g., AUTO and MatCont (Govaerts and Kuznetsov, 2008) implemented in Matlab. There is a branch of saddle-node bifurcations of periodic solutions originating from each such degenerate Hopf bifurcation point. A degenerate Hopf bifurcation point and a branch of saddle-node bifurcations of periodic solution are marked as a red dot and a green curve, respectively, in Fig. 2.4.

For a subcritical Hopf bifurcation point occurring in equations (2.3) for $p < 0.1721$, there exists a small region to the left of the Hopf bifurcation curve such that within the small region the equilibrium is surrounded by an unstable periodic orbit created in the Hopf bifurcation. Therefore, within this region the stable manifold of the equilibrium is a topological disk bounded by the periodic orbit. See Guckenheimer and Kuehn (2009) for more details of the proof of the existence of such small region. Since the boundary of the stable manifold is the small amplitude periodic orbit, a large amplitude homoclinic orbit cannot exist in such a region. Furthermore, the periodic orbits created in these subcritical Hopf bifurcations occur on the left hand side of the Hopf curve which is the same side as the C-shaped curve of homoclinic orbits. Based on the argument above, one can conclude that the homoclinic bifurcation curve cannot reach the Hopf bifurcation curve if the Hopf bifurcation is subcritical. This is in contrast to the case where Hopf bifurcation is supercritical, when a homoclinic curve may reach the Hopf bifurcation, as is observed in the bifurcation sets in various models of calcium dynamics (Champneys et al., 2007).

For the parameter values given in (2.2), the homoclinic bifurcation curve occurs within a range of wave speed values ($0.83 < s < 1.37$), and within the same range of wave speed values the Hopf bifurcation is always subcritical. According to the analysis above, the homoclinic curve cannot reach the Hopf bifurcation curve in this case. As discussed in Champneys et al. (2007), before reaching the Hopf bifurcation the homoclinic curve instead turns around at one end of the C-shaped curve, doubles back on itself in the (p, s) parameter plane and connects to the other end of the C-shaped curve to form a closed loop. The two branches of the homoclinic bifurcation curve lie almost on top of each other in the (p, s) plane so we plot the numerically computed L_2-norm of the homoclinic orbits in panel (a) of Fig. 2.5 to distinguish these two branches of homoclinic orbits. The branch with large (resp. small) L_2-norm value is denoted as the upper (resp. lower) branch of homoclinic orbits. This closed loop is referred to as a “homoclinic banana” in Champneys et al. (2007). Panels (b) and (c) of Fig. 2.5 show the homoclinic orbits of the upper and lower branches near the parameter values $(p, s) = (0.04575, 1.30)$. Homoclinic orbits with one and two spikes, like those in panels (b) and (c), are usually referred to as a single and double pulse solutions, respectively. The existence and stability of multiple pulse homoclinic solutions near the single pulse homoclinic solutions in the FHN system has been studied by a number of people (Evans et al., 1982; Deng, 1991; Bell and Deng, 2002; Guckenheimer and Kuehn, 2009).

Champneys and collaborators (Champneys et al., 2007) analyzed the dynamics near turning points of the homoclinic bifurcation curve and conjectured that there exists a codimension-two bifurcation point which they named an ‘EP1t’ point, but did not locate any EP1t points directly. The dynamics in the neighbourhood of such EP1t points was further analyzed in Champneys et al. (2009), where it was shown that there will be an infinite number of turning points of homoclinic curves near such EP1t points. An EP1t point is actually an intersection point between two codimension-one bifurcation curves on the parameter plane. The codimension-one bifurcations involve heteroclinic connections between an equilibrium and a periodic orbit as described below. We were

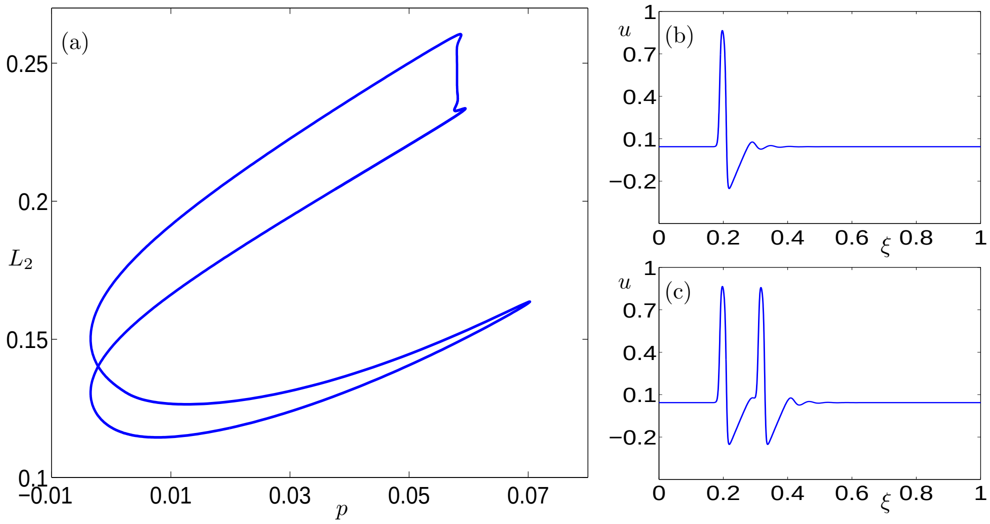

Figure 2.5: Another projection of the homoclinic curve (with L_2-norm plotted against p) in Fig. 2.4 for equations (2.3) with parameters (2.2), to distinguish the two branches of the closed loop. The time series of single pulse and double pulse solutions near (p, s)=(0.04575,1.30) in Fig. 2.4 are depicted in panel (b) and (c).

able to locate the EP1t points numerically in the FHN equations (2.3) and they turn out to be very close to the turning points of the homoclinic bifurcation curve (see Fig. 2.4). Thus, we find numerical evidence to support the conjecture in Champneys et al. (2007) that the homoclinic loci in equations (2.3) turn around near EP1t points.

More precisely, equations (2.3) have a unique equilibrium point and the periodic orbit of interest is created on the Hopf bifurcation curve. To the left of the U-shaped Hopf curve, the equilibrium has a one-dimensional unstable manifold and a two-dimensional stable manifold, while the periodic orbit has a two-dimensional unstable manifold and a two-dimensional stable manifold. An EP1t point is a point of intersection between a codimension-one curve of heteroclinic connections from the equilibrium to the periodic orbit (denoted as EtoP) and a codimension-one curve of tangency of the heteroclinic connection from the periodic orbit to the equilibrium (denoted as PtoE tangency).

We locate these two codimension-one global bifurcation curves with Lin's method for finding and continuing heteroclinic connections involving periodic orbits. The numerical algorithm was introduced in Krauskopf and Riess (2008) and its implementation for finding and continuing global bifurcations will be discussed further in chapter 6. The EtoP and PtoE tangency curves are plotted in magenta and black, respectively, on the (p, s) parameter space in Fig. 2.4. The codimension-one EtoP curve terminates at the Hopf bifurcation, since within the region of the (p, s) parameter plane bounded by the U-shaped curve of the Hopf bifurcations, the EtoP heteroclinic connection is generic (of codimension zero). The codimension-one PtoE tangency curve stops at a saddle-node bifurcation of periodic orbits, at which the periodic orbit disappears. This saddle-node bifurcation curve originates from the degenerate Hopf bifurcation point on the Hopf curve.

In summary, we have computed new features of the bifurcation set of equations (2.3) which enabled us to locate several codimension-two bifurcation points which act as organizing centres for the bifurcation set. In particular, codimension-one EtoP and PtoE tangency curves were located and found to intersect at codimension-two EP1t points, confirming an earlier conjecture of Champneys et al. (2007).

2.5 Homoclinic bifurcations in the singular limit

In the previous section, we showed that the bifurcation structure in the FHN model is rather complex. Since the FHN equations have variables evolving on widely separated time scales, we would like to exploit the separation of the time scales in the system to simplify the analysis of the model. The separation of the time scales of different variables is indicated by a small parameter ε. When $\varepsilon \neq 0$, the system is referred to as the full system, and when $\varepsilon = 0$ the system is usually referred to as the singular limit. The dynamics of the singular limit of the system gives us useful information about the dynamics of the full system.

2.5.1 Brief summary of geometric singular perturbation theory

For systems of ordinary differential equations with multiple time scales, properties of solutions can sometimes be studied using standard mathematical techniques known as geometric singular perturbation theory (GSPT). In this subsection we give a brief summary of GSPT, including some basic ideas, relevant definitions and useful results. The techniques and results will be applied to the FitzHugh-Nagumo equations (2.3) in section 2.5.2.

A typical system of ordinary differential equations with multiple time scales has the standard form:

$$\begin{aligned}\frac{dx}{dt} &= f(x, y, \varepsilon),\\ \frac{dy}{dt} &= \varepsilon g(x, y, \varepsilon),\end{aligned} \tag{2.4}$$

where $x \in \mathbb{R}^m$, $y \in \mathbb{R}^n$, and $0 < \varepsilon \ll 1$. The variables x and y are usually referred to as the fast and slow variables, respectively.

The variable t is referred to as the fast time. Define $\tau = \varepsilon t$ as the slow time. By switching the independent variable in (2.4) from the fast time t to the slow time τ one obtains the equivalent system

$$\begin{aligned}
\varepsilon\frac{dx}{d\tau} &= f(x,y,\varepsilon), \\
\frac{dy}{d\tau} &= g(x,y,\varepsilon).
\end{aligned} \tag{2.5}$$

Then one can study the dynamics of equations (2.4) by analysing the dynamics of the layer problem

$$\begin{aligned}
\frac{dx}{dt} &= f(x,y,0), \\
\frac{dy}{dt} &= 0,
\end{aligned} \tag{2.6}$$

and the dynamics of the reduced system

$$\begin{aligned}
0 &= f(x,y,0), \\
\frac{dy}{d\tau} &= g(x,y,0),
\end{aligned} \tag{2.7}$$

which are the limiting cases for $\varepsilon = 0$ on the fast and slow time scales, respectively. The phase space of the reduced problem (2.7) is the set denoted by $S = \{(x,y) \in \mathbb{R}^{m+n} : f(x,y,0) = 0\}$, which is referred to as the critical manifold of the system. The critical manifold corresponds to a set of equilibria for the layer problem (2.6).

By Fenichel theory (Fenichel, 1979) normally hyperbolic pieces of the critical manifold (i.e., these pieces of the critical manifold such that all eigenvalues of Jacobian matrix of the layer problem evaluated along S have real parts not equal to zero) perturb to nearby invariant manifolds S^ε of the full system (2.4). The flow near the invariant manifolds S^ε can be approximated by the flow near the corresponding normally hyperbolic pieces of the critical manifold S. It follows that, by carefully combining information about the dynamics of the reduced system and the layer problem, it is often possible to get helpful information about the dynamics of the full system; see Fenichel (1979) for more detailed information about GSPT. The main point needed for the work that follows is the observation that some orbits and structures in the full system can be seen to arise as perturbations of similar orbits and structures in the singular limit. In the following sections, we use this observation to investigate the dynamics of the FHN equations (2.3) further.

2.5.2 Homoclinic bifurcations in the singular limit

A homoclinic bifurcation of an equilibrium is a global bifurcation, and as such is usually difficult to locate in the parameter plane analytically. However, since the FHN model has multiple time scales, it is possible to consider the profile of the homoclinic orbit in the singular limit, and use the information to help us to find the locus of the homoclinic bifurcation in the singular limit. Then we can apply standard geometric singular perturbation techniques to show that homoclinic bifurcations exist in the full system, at a distance $O(\varepsilon)$ away from the locus of homoclinic bifurcations in the singular limit.

Homoclinic solutions of the FHN classical form without the applied current term have been extensively studied and clearly understood (Bell and Deng, 2002; Deng, 1991; Jones et al., 1991; Krupa et al., 1997; Yanagida, 1985). The form of FHN equations (2.3) we study contains an applied current term, and the homoclinic solutions for this form are not as well understood as for the classical form. In order to make easy comparison with the results obtained in the classical form, it is convenient to transform equations (2.3) into the classical form.

We have derived a linear transformation of the variables and a nonlinear transformation of the parameters of equations (2.3) to change equations (2.3) to the classical FHN form. Specifically, we introduce new variables and parameters as follows:

$$\begin{aligned}
&x = \frac{u-u_0}{u_2-u_0}, \quad y = \frac{\sqrt{D_c}v}{(u_2-u_0)^2},\\
&z = \frac{w-w_0}{(u_2-u_0)^3}, \quad \alpha_1 = \frac{u_1-u_0}{u_2-u_0},\\
&s_1 = \frac{s}{\sqrt{D_c}(u_2-u_0)}, \quad \varepsilon_1 = \frac{\varepsilon}{(u_2-u_0)^4},\\
&\gamma_1 = (u_2-u_0)^2\gamma, \quad \tau = \frac{(u_2-u_0)\xi}{\sqrt{D_c}},
\end{aligned} \tag{2.8}$$

where $(u_0(p), 0, w_0(p))$ is the unique equilibrium point of equations (2.3) which is determined by the parameter p and u_0, u_1, u_2 are the three real roots of the cubic polynomial

$$g(u) = u(u-1)(u-\alpha) - u_0(u_0-1)(u_0-\alpha).$$

Substituting the new variables and parameters defined in (2.8) into equations (2.3), we obtain the following classical form of the FHN equations:

$$\begin{aligned}
\frac{dx}{d\xi} &= y,\\
\frac{dy}{d\xi} &= s_1 y - x(x-1)(\alpha_1 - x) + z,\\
\frac{dz}{d\xi} &= \frac{\varepsilon_1}{s_1}(x - \gamma_1 z).
\end{aligned} \tag{2.9}$$

The bifurcation parameters for (2.9) are α_1 and s_1. The layer and reduced problems for equations (2.9) are:

$$\begin{aligned}\frac{dx}{d\xi} &= y,\\ \frac{dy}{d\xi} &= s_1 y - x(x-1)(\alpha_1 - x) + z, \\ \frac{dz}{d\xi} &= 0,\end{aligned} \tag{2.10}$$

and

$$\begin{aligned}0 &= y,\\ 0 &= s_1 y - x(x-1)(\alpha_1 - x) + z, \\ \frac{dz}{d\xi} &= \frac{1}{s_1}(x - \gamma_1 z).\end{aligned} \tag{2.11}$$

The critical manifold of equations (2.9) is the set

$$S = \{(x, y, z) \in \mathbb{R}^3 : y = 0, z = x(x-1)(\alpha_1 - x)\}.$$

The critical manifold S is a one-dimensional cubic curve with one local minimum point and one local maximum point, and is divided into three parts by the local minimum and maximum : the left section S_l, the middle section S_m and the right section S_r.

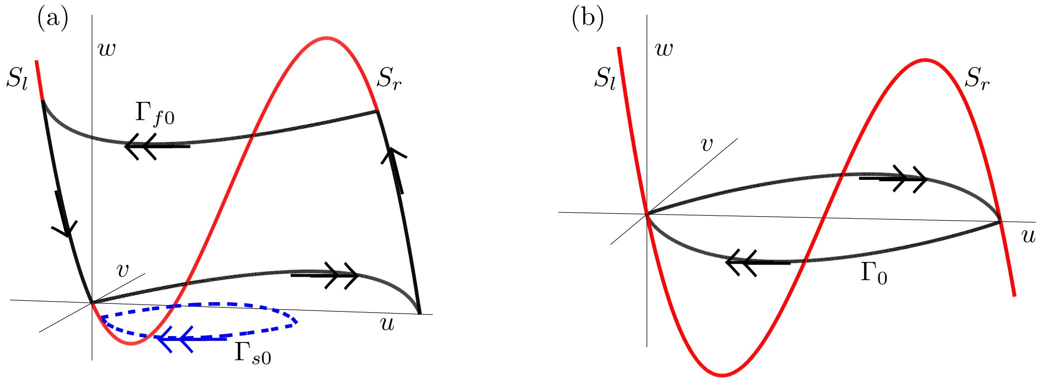

Figure 2.6: (a) Phase portraits of typical singular homoclinic orbits Γ_{f0} (black solid curve) and Γ_{s0} (blue dashed curve) for $0 < \alpha < \frac{1}{2}$. (b) Phase portrait of a heteroclinic cycle Γ_0, which is the coalescence of singular homoclinic orbits Γ_{f0} and Γ_{s0} at $\alpha = \frac{1}{2}$. This figure is adapted from Krupa et al. (1997).

Homoclinic solutions of equations (2.9) have been studied in Krupa et al. (1997). Here we review some relevant results. Equations (2.9) have a single equilibrium $p_0 = (0, 0, 0)$, and two types of singular homoclinic orbits associated with the equilibrium, denoted as Γ_{f0} and Γ_{s0}, exist when $\varepsilon_1 = 0$. The orbit Γ_{f0} exists on a curve in the (α_1, s_1) plane, and is constructed in the following way. When $\varepsilon_1 = 0$, for a fixed value of $\alpha_1 \in [0, \frac{1}{2}]$ there exists a unique positive value of s_1 such that there is a heteroclinic connection (wave front) from p_0 to $p_1 = (1, 0, 0)$ in the plane $\{z = 0\}$. Typically in the plane $\{z = 0\}$ no heteroclinic connection from p_1 to p_0 exists, but one can find another plane $\{z = z^*\}$ such that there is a connection (wave back) from a point in S_r to a point in S_l in the plane. Hence there exists a singular orbit Γ_{f0} consisting of the connection from p_0 to p_1 in $\{z = 0\}$, the piece of S_r from p_1 to $S_r \cap \{z = z^*\}$, the connection from S_r to S_l in $\{z = z^*\}$ and the piece of S_l from $S_l \cap \{z = z^*\}$ to p_0. Panel (a) of Fig. 2.6 depicts a typical phase portrait for the singular orbit Γ_{f0}.

From the construction of the orbit Γ_{f0}, one observes that finding the curve of homoclinic orbits Γ_{f0} is equivalent to finding the curve of heteroclinic connections from p_0 to p_1 in the plane $\{z = 0\}$, where the layer problem (2.10) simplifies to the following equations

$$\begin{aligned} \frac{dx}{d\xi} &= y, \\ \frac{dy}{d\xi} &= s_1 y - x(x-1)(\alpha_1 - x). \end{aligned} \tag{2.12}$$

Exact formulae for heteroclinic connections from one equilibrium to another of equations (2.12) are obtained in Li and Guo (2006) using the first integral method introduced in Feng (2002). In particular, the heteroclinic solution of equations (2.12) from (0,0) to (1,0) exists on a line segment $s_1 = \frac{1-2\alpha_1}{\sqrt{2}}$ for $\alpha_1 \in [0, \frac{1}{2}]$.

The other type of singular orbit Γ_{s0} occurs when $s_1 = 0$, in which case the layer problem simplifies to a Hamiltonian system with the form

$$\begin{aligned} \frac{dx}{d\xi} &= y, \\ \frac{dy}{d\xi} &= -x(x-1)(\alpha_1 - x). \end{aligned} \tag{2.13}$$

System (2.13) admits a planar homoclinic orbit Γ_{s0} to the equilibrium point $(0, 0)$ in the (x, y) phase plane for $\alpha_1 \in (0, \frac{1}{2})$. Typical phase portraits of these two types of singular orbits Γ_{f0} and Γ_{s0} are shown in panel (a) of Fig. 2.6.

From the relation between the wave speed for Γ_{f0} and parameter α_1 ($s_1 = \frac{1-2\alpha_1}{\sqrt{2}}$), we can infer that as α_1 increases towards 0.5, the value of s_1 where Γ_{f0} occurs decreases towards zero. At a critical point when $\alpha_1 = 0.5$, the wave speed s_1 is zero, i.e., the two singular orbits Γ_{f0} and Γ_{s0} coalesce. Two line segments of singular homoclinic orbits join together at the point $(\alpha_1, s_1) = (0.5, 0)$ and there exists a heteroclinic cycle Γ_0 connecting p_0 to p_1 at this point. The heteroclinic cycle Γ_0 is depicted in panel (b) of Fig. 2.6. The two branches of singular homoclinic orbits are depicted in Fig. 2.7.

Homoclinic orbits of equations (2.9) can be obtained by perturbing singular homoclinic orbits Γ_{f0} and Γ_{s0} for $0 < \varepsilon_1 \ll 1$. Homoclinic orbits found by perturbing Γ_{f0} are referred to as fast waves and others found by perturbing Γ_{s0} are referred to as slow waves. It is conjectured in Yanagida (1985) that the bifurcation curve corresponding to fast waves and the bifurcation curve corresponding to slow waves are connected in the full system. It is shown in Krupa et al. (1997) that these two bifurcation curves are indeed connected near the singular limit.

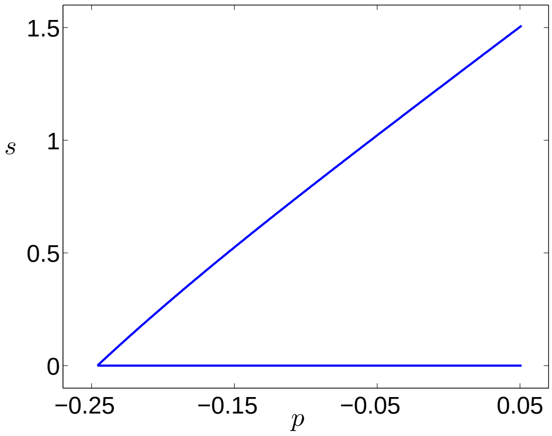

Figure 2.7: The position of the homoclinic bifurcations in the (p, s) plane in the singular limit $\varepsilon = 0$ for equations (2.3), showing two curves of singular homoclinic orbits joining together to form a C-shaped curve.

We can now find the location of bifurcation curves in the (p, s) parameter plane of equations (2.3) by mapping the points on the parameter plane (α_1, s_1) to the points on the parameter plane (p, s) through the relation given in (2.8). The mapping is a bijection but not linear so the locus of the singular homoclinic orbit Γ_{f0} in the (p, s) parameter plane is not a line segment; see Fig. 2.8. In Guckenheimer and Kuehn (2009), the authors conjectured that the homoclinic bifurcation curve converges to a line segment in the (p, s) parameter plane at the singular limit but our approach shows a different result.

In summary, we have applied GSPT to analyze our model equations (2.3). With the help of a transformation from equations (2.3) into the classical FHN form (2.9), homoclinic solutions are shown to exist on a C-shaped locus in the (p, s) plane in the singular limit, as shown in Fig. 2.7. Then, according to Krupa et al. (1997), when ε is sufficiently small, the upper (resp. lower) branch of the C-shaped curve perturbs to a branch of homoclinic orbits Γ_f^ε (resp. Γ_s^ε) in the full system. The two branches of curves of homoclinic solutions connect to form a C-shaped curve of homoclinic orbits for small nonzero values of ε.

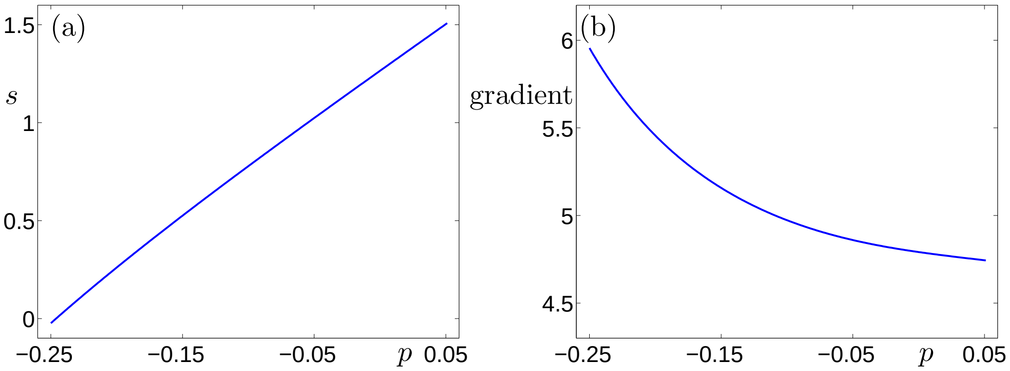

Figure 2.8: (a) Locus of the singular homoclinic orbits Γ_{f0} in the (p, s) plane for equations (2.3). (b) Gradient of the bifurcation curve in panel (a), indicating that the bifurcation curve in panel (a) is not a straight line segment.

2.6 Hopf bifurcations in the singular limit

We can find the position of the Hopf bifurcation analytically for the full FHN model. The equilibrium point of equations (2.3) is solely determined by the parameter p and not dependent on the parameter s. The Jacobian matrix evaluated at this equilibrium $(u_0(p), v_0(p), w_0(p))$ is:

$$\begin{pmatrix} 0 & 1 & 0 \\ -\frac{f'(p)}{D_c} & \frac{s}{D_c} & \frac{1}{D_c} \\ \frac{\varepsilon}{s} & 0 & -\frac{\gamma\varepsilon}{s} \end{pmatrix}.$$

The Hopf bifurcation of this equilibrium occurs when two eigenvalues of the Jacobian matrix are pure imaginary numbers, in which case the only real eigenvalue is equal to the trace of the Jacobian matrix, $\frac{s}{D_c} - \frac{\gamma\varepsilon}{s}$. Furthermore, the characteristic polynomial of the Jacobian matrix is a cubic function:

$$P(\lambda) = \lambda^3 + \Big(\frac{\varepsilon\gamma}{s} - \frac{s}{D_c}\Big)\lambda^2 + \Big(\frac{f'(p)}{D_c} - \frac{\varepsilon\gamma}{D_c}\Big)\lambda + \frac{\varepsilon\gamma f'(p)}{sD_c} - \frac{\varepsilon}{sD_c}.$$

Since the real eigenvalue $\frac{s}{D_c} - \frac{\gamma\varepsilon}{s}$ is a root of the characteristic polynomial, i.e., $P(\frac{s}{D_c} - \frac{\gamma\varepsilon}{s}) = 0$, we can use a symbolic computation package such as Matlab to rearrange the equation to find the values of s for which the Hopf bifurcations occurs:

$$s\sqrt{f'(p) - \gamma\varepsilon} = \sqrt{\varepsilon D_c(1 - \gamma^2\varepsilon)}. \tag{2.14}$$

In the singular limit when $\varepsilon = 0$, if $f'(p) = 0$ then equation (2.14) is satisfied at any value of wave speed s greater than or equal to zero; this case gives rise to two vertical bifurcation branches at $p \approx 0.05$ and $p \approx 0.55$. If $f'(p) > 0$ then equation (2.14) is satisfied at $s = 0$; this case gives rise to a horizontal bifurcation branch at $s = 0$

between the two vertical branches. The three branches form a U-shaped curve in the (p, s) plane, as shown in Fig. 2.9. A similar result was obtained in Guckenheimer and Kuehn (2009) with a different approach.

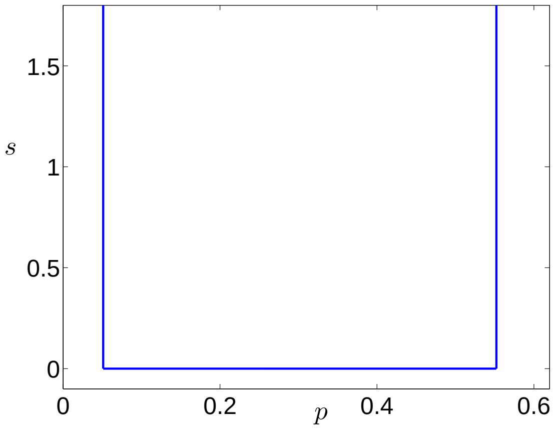

Figure 2.9: The position of Hopf bifurcations of equations (2.3) with parameters (2.2) in the (p, s) parameter plane in the singular limit $\varepsilon = 0$.

We now examine the criticality of the Hopf bifurcations, which can be determined by the sign of the so-called first Lyapunov coefficient (Kuznetsov, 1998). More information about the formal definition and computation of the first Lyapunov coefficients is contained in section 5.3.1.

As mentioned before, if the function $f'(p) > 0$ then the Hopf bifurcation occurs at $s = 0$, and the Jacobian matrix evaluated at the equilibrium is:

$$\begin{pmatrix} 0 & 1 & 0 \\ \frac{-f'(p)}{D_c} & 0 & \frac{1}{D_c} \\ 0 & 0 & 0 \end{pmatrix}.$$

The eigenvalues of the equilibrium are a pair of pure imaginary eigenvalues and one zero eigenvalue. Note that the system is (linearly) degenerate because the Jacobian matrix has a zero eigenvalue. Now the bifurcation package MatCont (Govaerts and Kuznetsov, 2008) can be used to calculate the value of the first Lyapunov coefficient associated with the Hopf bifurcation numerically. As it turns out, the numerical results indicate that the Hopf bifurcations at $s = 0$ have first Lyapunov coefficients equal to zero which means that the Hopf bifurcations are degenerate in the singular limit. In this case the singular limit gives no information about the criticality of the Hopf bifurcation in the full system.

If the function $f'(p) = 0$ then as $\varepsilon \to 0$ the Hopf bifurcation can occur at any $s \geq 0$

and the Jacobian matrix evaluated at the equilibrium is:

$$\begin{pmatrix} 0 & 1 & 0 \\ 0 & \frac{s}{D_c} & \frac{1}{D_c} \\ 0 & 0 & 0 \end{pmatrix}.$$

The eigenvalues of the equilibrium are a pair of zero eigenvalues and one real eigenvalue $\frac{s}{D_c}$; this double zero bifurcation was analyzed extensively in Baer and Erneux (1986, 1992). With the method introduced in Baer and Erneux (1986, 1992), Braaksma (Braaksma, 1998) showed that the double zero bifurcation perturbs to a subcritical Hopf bifurcation in the FHN full system for $\varepsilon > 0$. Therefore, in this case the dynamics of Hopf bifurcation in the full system can be understood as a perturbation of the dynamics of the Hopf bifurcation in the singular limit.

2.7 Comparison between the full system and the singular limit

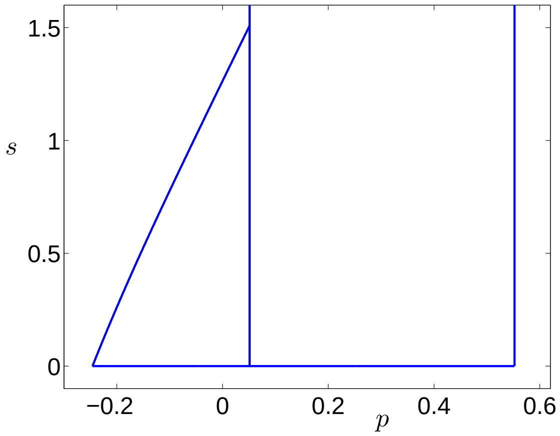

Figure 2.10: The position of the homoclinic bifurcations and Hopf bifurcations in the (p, s) plane in the singular limit $\varepsilon = 0$ for equations (2.3).

From the analysis in the singular limit discussed in sections 2.5 and 2.6, one can conclude that the bifurcation set at $\varepsilon = 0$ is quite simple, with a C-shaped homoclinic curve and a U-shaped Hopf bifurcation curve. The two bifurcation curves connect with each other in the (p, s) parameter plane as shown in Fig. 2.10. The bifurcation set indicates that solitary wave solutions exist for p in the interval $(-0.2459, 0.0511)$ in the singular limit.

In Champneys et al. (2007), it is noted that equations (2.3) have a symmetry. In particular, for the choice of parameters in (2.2), the bifurcation set in the (p, s) plane

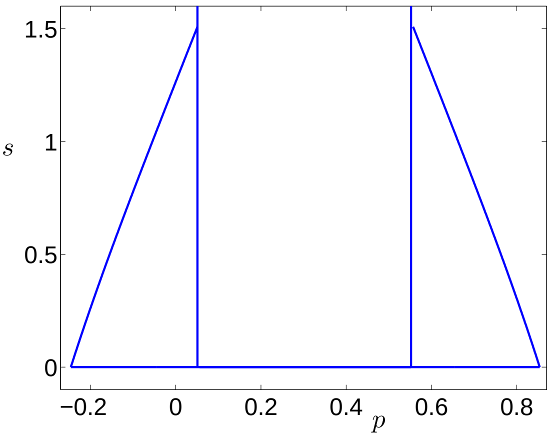

Figure 2.11: The symmetric position of the homoclinic bifurcations and Hopf bifurcations under reflection through the line $p \approx 0.305$ in the (p, s) plane in the singular limit $\varepsilon = 0$ for equations (2.3).

is symmetric under reflection through the line $p \approx 0.305$. This means that there are in fact two C-shaped homoclinic curves attached to the U-shaped Hopf bifurcation curve in the singular limit; the one to the left exists in the interval $(-0.2459, 0.0511)$, while the one to the right exists in the interval $(0.5583, 0.8553)$, as shown in Fig. 2.11.

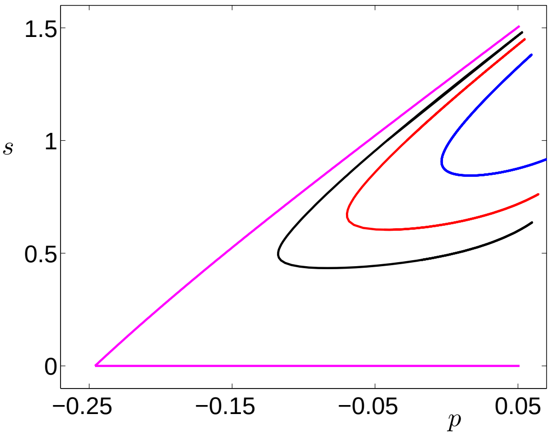

Figure 2.12: Homoclinic bifurcation curves in the (p, s) parameter plane for different values of ε in the FHN equations (2.3). The C-shaped curve in magenta stands for the homoclinic curve in the singular limit. The blue, red and black C-shaped curves represent the homoclinic curves at $\varepsilon = 0.0025$, $\varepsilon = 0.005$ and $\varepsilon = 0.01$, respectively.

With the help of Fenichel's theory (Fenichel, 1979), Krupa and collaborators (Krupa et al., 1997) showed that the C-shaped curve of homoclinic bifurcations persists if ε is sufficiently small. Fig. 2.12 shows several curves of homoclinic orbits in the full system for various small ε. It can be seen in Fig. 2.12 that the locus of homoclinic bifurcations in the full system curves moves towards the locus in the singular limit as $\varepsilon \to 0$, as predicted by the theory.

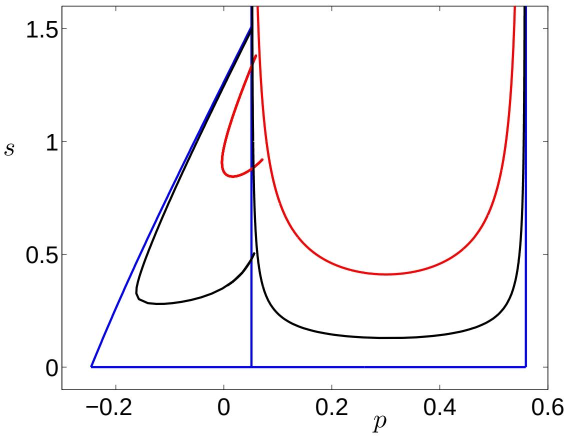

Figure 2.13: Relative positions of homoclinic and Hopf bifurcation curves in the (p, s) parameter plane for different values of ε in the FHN system (2.3). The curves in blue stand for the homoclinic and Hopf bifurcation curves in the singular limit, and the red and black curves represent the homoclinic and Hopf bifurcation curves for $\varepsilon = 0.01$ and $\varepsilon = 0.001$, respectively.

In section 2.6, it was shown that the U-shaped Hopf bifurcation curve persists for small values of ε at the location in the (p, s) plane specified by the relation (2.14). However, the relative position between the Hopf bifurcation curve and the homoclinic bifurcation curve shifts as ε moves away from zero. Numerical results about the positions of the homoclinic curve and Hopf curve for the cases of $\varepsilon = 0$, $\varepsilon = 0.001$ and $\varepsilon = 0.01$ are shown in Fig. 2.13. Fig. 2.13 shows that the Hopf and homoclinic bifurcation curve have a gap between them when $\varepsilon \neq 0$. The reason why there must exist such a gap was discussed in section 2.4, and it arises from the geometry of the stable manifold of the equilibrium near the subcritical Hopf bifurcations. It is claimed in Guckenheimer and Kuehn (2009) that the homoclinic curve terminates at a tangency bifurcation between stable and unstable manifolds of the slow manifold which is a small perturbation from the critical manifold.

Another way of understanding how the homoclinic bifurcation curve stops before reaching the Hopf bifurcation curve follows from our numerical bifurcation analysis of equation (2.3). Specifically, codimension-two EP1t points for equations (2.3) with $\varepsilon = 0.01$ were found numerically using Lin's method implemented in AUTO. The C-shaped homoclinic bifurcation curve turns around in the neighbourhood of such EP1t points before reaching the Hopf bifurcation curve. In other words, the EP1t points indicate the end points of the C-shaped homoclinic curve.

To sum up, the bifurcation set for the FHN equations (2.3) in the full system has a basic CU structure perturbed from the simple CU structure in the singular limit. However, there are complex bifurcations occurring between the C-shaped homoclinic curve and the U-shaped Hopf curve in the full system, and these details need to be taken into account when we try to understand interactions between the wave solutions of the FHN model (2.1).

We have not yet understood how all the complex bifurcations in the full system unfold from the singular limit in the FHN system. We conjecture that features such as the codimension-two EP1t points can be seen to arise from a perturbation of the simple CU bifurcation structure that occurs in the singular limit; a detailed theoretical analysis to support this conjecture is left to future work.

Chapter 3

Waves of a prototypical calcium model

In this chapter, we consider the wave solutions of a prototypical calcium model. The motivation for us to focus on this model is that we are interested in analyzing and understanding wave solutions commonly observed in a wide range of models of intracellular calcium dynamics; a prototypical calcium model of relatively simple equations omitting the minor details of various fluxes is beneficial to our study. Findings about the wave solutions of the prototypical calcium model can then be extended to gain new understanding for more realistic quantitative intracellular calcium models.

The numerical results in Champneys et al. (2007) suggest that the basic bifurcation structure of calcium models is largely independent of model assumptions about the IP$_3$ receptor dynamics, at least for a range of models. Specifically, Champneys and collaborators (Champneys et al., 2007) showed that different variants of a pancreatic acinar cell model (Sneyd and Dufour, 2002; Sneyd et al., 2003) with different numbers of receptor variables displayed a similar basic bifurcation structure. Therefore, we consider a two-component calcium model with diffusion that describes the calcium exchange within the cell and across the cell membrane. One important assumption of this prototypical model is that the IP$_3$ receptor dynamics reaches steady state instantaneously.

The focus of this chapter is to understand the solitary wave solutions and periodic wave solutions in the prototypical calcium model. Similarly to the FHN model we considered in chapter 2, the prototypical model has a basic CU bifurcation structure in a suitably chosen parameter plane. In order to obtain a better understanding of this CU structure, we follow a similar approach to chapter 2 and consider the singular limit of the model, and then compare the dynamics in the singular limit with the dynamics of the full model.

Parts of the work presented in this chapter have been done in collaboration with

J. C. Tsai, V. Kirk and J. Sneyd, and have been written up in the manuscript (Tsai et al., 2012), which has been submitted to a journal. The work presented in this chapter is mostly of a numerical nature; the numerical results have, however, induced conjectures about theoretical results, some of which have now been proven and will appear in Tsai et al. (2012).

3.1 Model equations

As discussed in chapter 1, a cell can sometimes be assumed to be a one-dimensional line segment (a 'long thin cylinder') so conduction of the variation of calcium concentration along the cell occurs in one spatial dimension. A model describing the intracellular calcium dynamics in such a cell may have the general form:

$$\begin{aligned} \frac{\partial c}{\partial t} &= D\frac{\partial^2 c}{\partial x^2} + F(c, c_e), \\ \frac{\partial c_e}{\partial t} &= G(c, c_e), \end{aligned} \tag{3.1}$$

where the functions F and G are given by:

$$\begin{aligned} F(c, c_e) &= J_{\text{release}} - J_{\text{serca}} + \varepsilon(J_{\text{influx}} - J_{\text{pm}}), \\ G(c, c_e) &= \gamma(J_{\text{serca}} - J_{\text{release}}). \end{aligned}$$

The variable c represents the cytoplasmic calcium concentration, and the variable c_e represents the calcium concentration in the ER.

In our simplified model, specific expressions for the fluxes J_{release}, J_{serca}, J_{influx} and J_{pm} are derived from a model of calcium oscillations in the Xenopous laevis oocyte (Atri et al., 1993) as explained below. We use the following form of equations:

$$\begin{aligned} \frac{\partial c}{\partial t} &= D\frac{\partial^2 c}{\partial x^2} + f(c)(c_e - c) - k_s c + \varepsilon(J - c), \\ \frac{\partial c_e}{\partial t} &= -\gamma\big(f(c)(c_e - c) - k_s c\big), \end{aligned} \tag{3.2}$$

where

$$f(c) = \alpha + k_f \frac{c^2}{c^2 + \varphi_1^2} \cdot \frac{\varphi_2}{c + \varphi_2}. \tag{3.3}$$

Typical parameter values are given in Table. 3.1.

In this model, oscillations in the concentration of free cytoplasmic calcium arise via sequential release and uptake of calcium to and from the ER. Release of calcium from the ER is through IP$_3$ receptors and uptake of calcium into the ER is via calcium

D	α	k_s	k_f	φ_1	φ_2	γ	ε
$25.0\ \mu\text{m}^2\text{s}^{-1}$	$0.05\ \text{s}^{-1}$	$20.0\ \text{s}^{-1}$	$20.0\ \text{s}^{-1}$	$2.0\ \mu\text{M}$	$1.0\ \mu\text{M}$	5.0	0.1

Table 3.1: Values of parameters for equations (3.2).

SERCA pumps. Calcium can also enter from the outside of the cell, and is pumped out across the plasma membrane of the cell by other ATPase pumps.

In the original model of Atri et al. (Atri et al., 1993), the SERCA and plasma membrane pumps were modelled as saturating Hill functions of the calcium concentration in the cytoplasm. In addition, release of calcium through the IP_3 receptors was modelled by assuming fast activation of the IP_3 receptors by calcium followed by slower inactivation.

However, in order to construct the prototypical model used here much of the complexity of the original model by Atri et al. has been discarded, while keeping the essential qualitative features of the model. Thus, firstly, calcium release through the IP_3 receptors is modelled by a combination of Hill functions. The steady state flux through the IP_3 receptors is thus a biphasic function of the intracellular calcium concentration, as in the original model, but the functional form is chosen to be as simple as possible. Secondly, the calcium pumps are modelled as linear functions of the calcium concentration.

This simplified version of the Atri model captures the qualitative features that are important to our discussion, but has a much simpler functional form than the full model, making it easier to analyze. In this way, it bears the same relationship to a more complex calcium oscillation model as does the FitzHugh-Nagumo model to the Hodgkin-Huxley model.

The main bifurcation parameter is the term J which represents the influx going into the cell cytoplasm from extracellular space. One reason for choosing J as the bifurcation parameter is due to experimental considerations; it can be quite difficult to manipulate the environment inside a cell in physical experiments, which means that fluxes of intracellular calcium exchange are difficult to modulate. However, we have some control on the outside environment of a cell; the calcium influx entering the cell can sometimes be modulated experimentally, although with some technical difficulty. Mathematically speaking, we can vary the amplitude of the term J, and thus can conduct bifurcation analysis of equations (3.6) to obtain information and predictions about how the variation of the influx current amplitude affects the intracellular calcium dynamics. These predictions might then be tested experimentally by varying the input amplitude of J.

3.2 The analysis of equilibrium solutions

We first find the equilibrium solutions of equations (3.2) in the case there is no diffusion, i.e., find the equilibria of

$$\begin{aligned} \frac{dc}{dt} &= f(c)(c_e - c) - k_s c + \varepsilon(J - c), \\ \frac{dc_e}{dt} &= -\gamma\big(f(c)(c_e - c) - k_s c\big). \end{aligned} \tag{3.4}$$

One can verify that system (3.4) has a unique equilibrium solution given by

$$(c, c_e) = \left(J, \frac{\left(k_s + \alpha + k_f \frac{J^2}{J^2+\varphi_1^2} \frac{\varphi_2}{J+\varphi_2}\right) J}{\left(\alpha + k_f \frac{J^2}{J^2+\varphi_1^2} \frac{\varphi_2}{J+\varphi_2}\right)} \right).$$

The solution is the intersection point of a straight line $c = J$ and the curve defined by $f(c)(c_e - c) - k_s c = 0$ in the (c, c_e) plane.

3.2.1 The profile of the function f

An assumption made in the original model construction of intracellular calcium dynamics (Atri et al., 1993) is that the function f is single-humped. Here we check that the functional form chosen for f in the model has this qualitative feature.

Using f as in equation (3.3), we find the first derivative of f is:

$$\frac{df}{dc} = \frac{k_f \varphi_2 c}{(c^2 + \varphi_1^2)^2 (c + \varphi_2)^2} (-c^3 + c\varphi_1^2 + 2\varphi_1^2 \varphi_2) := \frac{k_f \varphi_2 c}{(c^2 + \varphi_1^2)^2 (c + \varphi_2)^2} f_1(c).$$

The discriminant of the cubic function f_1 is $-4\varphi_1^6 < 0$. Thus the relation $f_1(c) = 0$ has a unique real root, which, together with the fact that $f_1(0) > 0$ and $f_1(\infty) < 0$, shows that the real root is positive. Hence, one can deduce the relation $f'(c) = 0$ also has a unique positive real root by noticing that $\frac{k_f \varphi_2 c}{(c^2+\varphi_1^2)^2 (c+\varphi_2)^2}$ is always greater than zero. Moreover, we note that as $c \to 0$ or $c \to \infty$, the limit of the function $f(c)$ is α, and that $f'(0) = 0$ and $f''(0) > 0$. In view of the above discussion, we can conclude that $f(c)$ is single-humped. Fig. 3.1 shows a plot of $f(c)$ for the specific choice of parameters given in Table. 3.1.

3.2.2 The nullcline of the variable c

For the next step we investigate the c-nullcline of system (3.2) in the absence of diffusion. The c-nullcline is defined by the following equation:

$$f(c)(c_e - c) - k_s c + \varepsilon(J - c) = 0.$$

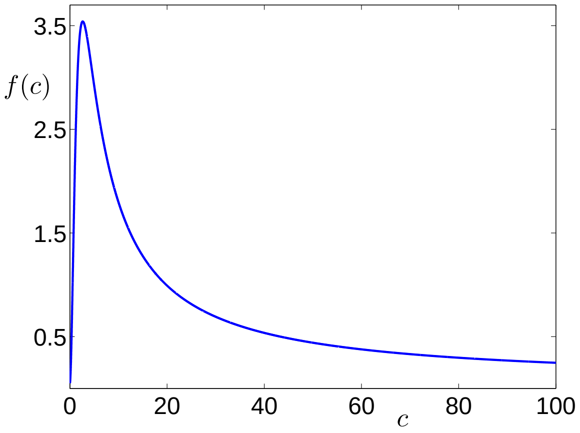

Figure 3.1: The shape of the function of f in (3.3) with parameters as given in Table. 3.1.

Rearranging the equation above to obtain c_e in terms of c yields:

$$c_e = \frac{f(c)c + k_s c - \varepsilon(J-c)}{f(c)}. \tag{3.5}$$

A plot of the relation (3.5) is given in Fig. 3.2 with the parameter values specified in Table. 3.1. As can be seen, the c-nullcline is an N-shaped curve on the (c, c_e) phase plane for these parameter values; it can be shown that this is the case for a range of different choices of parameter values and $\varepsilon = 0$ (Tsai et al., 2012).

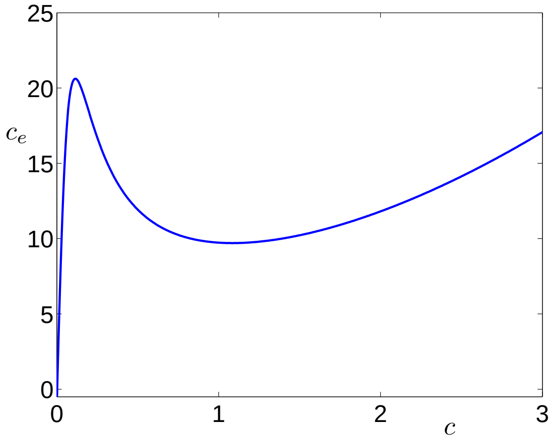

Figure 3.2: The c-nullcline of system (3.2) with $D = 0$ and with other parameters as specified in Table. 3.1.

3.3 Wave solutions

In the last section we established that the nullcline of the variable c of equations (3.2) is N-shaped. It turns out that just as the cubic u-nullcline was an important ingredient for showing the existence of the solitary wave solution of the FHN equations, so too is the N-shaped c-nullcline in the prototypical calcium model important for the existence of solitary wave solutions of equations (3.2).

3.3.1 The calcium model in travelling wave coordinates

For studying the wave solutions of the calcium model, it is convenient to convert equations (3.2) into travelling wave coordinates. We do this in the usual way by introducing a new independent variable $\xi = x + st$, where s represents the wave speed. This yields the system of ordinary differential equations as follows:

$$
\begin{aligned}
s\frac{dc}{d\xi} &= D\frac{d^2c}{d\xi^2} + f(c)(c_e - c) - k_s c + \varepsilon(J - c),\\
s\frac{dc_e}{d\xi} &= -\gamma(f(c)(c_e - c) - k_s c).
\end{aligned}
$$

Introducing another variable $v = \frac{dc}{d\xi}$, the above system becomes a system of three first-order ordinary differential equations:

$$
\begin{aligned}
\frac{dc}{d\xi} &= v,\\
\frac{dv}{d\xi} &= \frac{1}{D}\big(sv - f(c)(c_e - c) + k_s c - \varepsilon(J - c)\big), \qquad (3.6)\\
\frac{dc_e}{d\xi} &= -\frac{\gamma}{s}(f(c)(c_e - c) - k_s c).
\end{aligned}
$$

The solitary and periodic wave solutions of equations (3.2) corresponds to homoclinic and periodic solutions of equations (3.6), respectively.

3.3.2 Numerical bifurcation analysis

We used AUTO to locate the positions in the (J, s) plane of homoclinic bifurcations and Hopf bifurcations of equations (3.6). Fig. 3.3 depicts the basic bifurcation structure of equations (3.6) consisting of a C-shaped curve of homoclinic bifurcations and a U-shaped curve of Hopf bifurcations. This calcium model is representative of a wide range of models of calcium dynamics for different cell types. The CU structure found in the prototypical calcium model is consistent with the conjecture in Champneys et al. (2007) that many intracellular calcium models share a similar basic bifurcation structure.

The homoclinic curve terminates at the Hopf bifurcation at the upper end of the

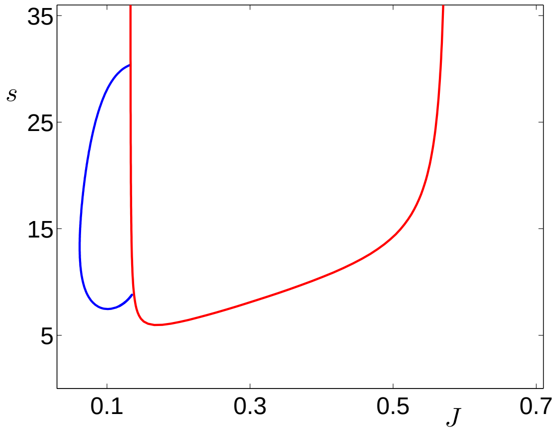

Figure 3.3: Partial bifurcation set for equations (3.6) with parameters as in Table 3.1, showing a U-shaped curve of Hopf bifurcations in red and a C-shaped curve of homoclinic bifurcations of the equilibrium in blue.

homoclinic curve, apparently at a Shil'nikov-Hopf bifurcation (Deng and Sakamoto, 1995; Hirschberg and Knobloch, 1993), as also observed in several other calcium models in Champneys et al. (2007).

As mentioned in section 2.4, for systems defined on $\mathbb{R}^3$, a homoclinic curve must turn around before reaching a Hopf bifurcation curve in the case that the Hopf bifurcation is subcritical. A zoom near the lower end of the homoclinic curve is shown in Fig. 3.4. At the lower end of the homoclinic curve, the homoclinic branch has a sharp turning point and traces back on itself, as expected from the observation that the Hopf bifurcations are subcritical near the lower end of the homoclinic curve.

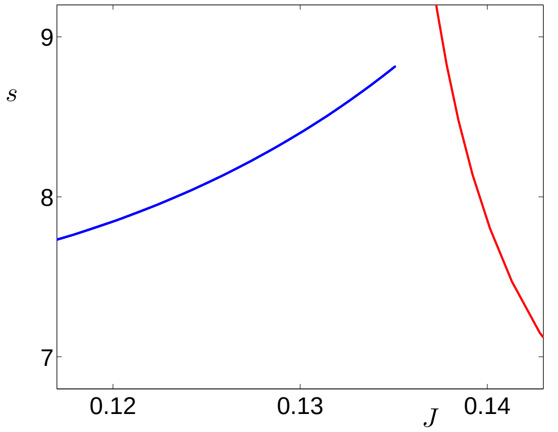

Figure 3.4: An enlargement near the lower end of the C-shaped homoclinic curve of Fig. 3.3. Although it cannot be seen on the scale of this figure, the blue homoclinic curve folds back on itself several times near the red Hopf bifurcation curve; see Fig. 3.5.

In fact, near the lower turning point, there are several different branches of the homoclinic curve lying almost on top of each other in the (J, s) plane. This is similar to the case for the pancreatic acinar cell model studied in Champneys et al. (2007) where the homoclinic branch has a series of turning points and does not form a closed loop in the parameter plane. In Fig. 3.5 we plot $v_{\max}$, the maximum value of v on the homoclinic orbit, against the bifurcation parameter, J, to distinguish these branches of homoclinic orbits.

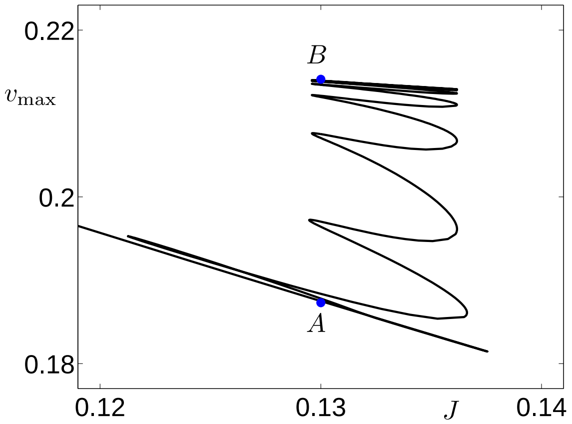

Figure 3.5: The homoclinic branch from Fig 3.4, with the maximum value of v on the homoclinic orbit, v_{max}, plotted as a function of J. The two blue large dots labelled A and B mark homoclinic orbits for which phase portraits are shown in Fig. 3.6.

The homoclinic branch has a sequence of turning points in the (J, s)-plane. As the homoclinic curve wiggles back and forth in the parameter plane, the homoclinic orbit gains extra loops. A homoclinic orbit at $(J, s) \approx (0.13, 8.38)$ (before the bifurcation curve goes through any turning points) is plotted in panel (a) of Fig. 3.6; another homoclinic orbit at almost the same parameter value is plotted in panel (b) of Fig. 3.6. As can be observed from panel (b) of Fig. 3.6, the homoclinic orbit resembles a heteroclinic cycle between the equilibrium point and a periodic orbit after these turns of the homoclinic bifurcation curve. The snaking of the homoclinic bifurcation curve is reminiscent of the behaviour near codimension-two EP1t bifurcation points, as described in Champneys et al. (2009).

In order to determine whether the homoclinic snaking observed is associated with EP1t points, we would need to find the EP1t points numerically in these calcium models. There are some recently developed numerical algorithms available to compute these types of global objects in a dynamical system. In chapter 6, we implement an algorithm based on Lin's method to compute global objects including EP1t points in a related calcium model, but have not directly checked the existence of EP1t points in equations (3.6).

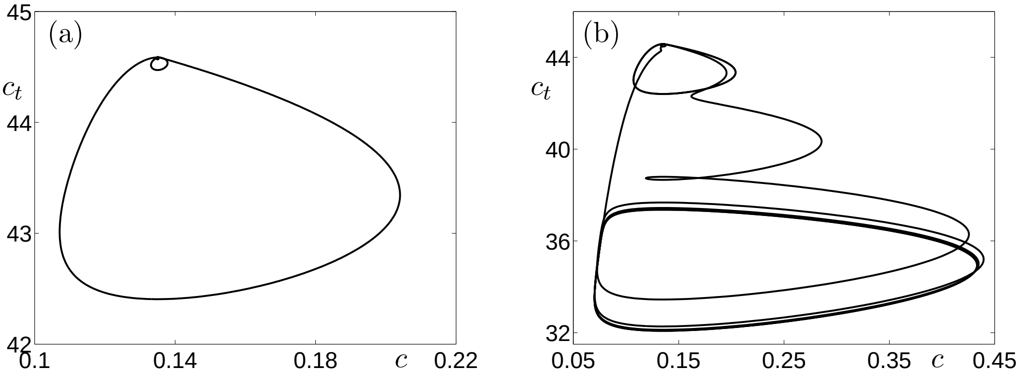

Figure 3.6: (a) The phase portrait of the homoclinic orbit at $J = 0.13$ before going through any turning points of the homoclinic bifurcation curve. The position of the homoclinic orbit is marked as point A in Fig. 3.5. (b) The homoclinic orbit at $J = 0.13$ after several turns of the homoclinic bifurcation curve. The position of the homoclinic orbit is marked as point B in Fig. 3.5.

3.3.3 Singular bifurcation analysis

As mentioned in chapter 1, calcium models, including the prototypical model studied here, typically contain terms modelling different processes evolving on different time scales. Therefore, there is the potential for analysis of the singular limit of the calcium model to provide insight into the overall bifurcation structure in the full system. Note that geometric singular perturbation theory has been used to study related calcium models in a different context in Harvey et al. (2010, 2011).

The first step for the singular bifurcation analysis is to find an appropriate singular limit of equations (3.6). For this, we need to nondimensionalise the equations by rescaling the variables, parameters and functions. We choose

$$\begin{aligned}&\bar{x} = \frac{x}{L},\ \bar{t} = \frac{t}{T},\ \bar{c} = \frac{c}{\varphi_2},\ \bar{c}_e = \frac{c_e}{\varphi_2},\ \bar{D} = \frac{DT}{L^2},\ \bar{\varphi}_1 = \frac{\varphi_1}{\varphi_2},\\ &\bar{\alpha} = T\alpha,\ \bar{k}_f = Tk_f,\ \bar{k}_s = Tk_s,\end{aligned}$$

where the characteristic length scale $L = 1$ μm and the characteristic time scale $T = 1$ s are used. Then the typical dimensionless parameter values corresponding to Table 3.1 are given in the following table:

$\bar{D}$	$\bar{\alpha}$	$\bar{k}_s$	$\bar{k}_f$	$\bar{\varphi}_1$	γ	ε
25.0	0.05	20	20	2.0	5.0	0.1

Table 3.2: Values of dimensionless parameters corresponding to the parameter values in Table. 3.1.

Substituting these rescaled variables, parameters, and functions into system (3.2) and dropping the bar, we find that the resulting system is identical to system (3.2) except that φ_2 now becomes 1. Hence in the following, we always assume that $\varphi_2 = 1$.

In addition, we introduce a new variable $c_t = \frac{sc_e}{\gamma} - Dv + sc$ to replace the variable c_e. Then the system of ODEs (3.6) becomes a slow-fast system in standard form:

$$\begin{aligned} \frac{dc}{d\xi} &= v, \\ \frac{dv}{d\xi} &= \frac{1}{D}\left(sv - \left(\alpha + k_f \frac{c^2}{c^2+\varphi_1^2} \cdot \frac{1}{c+1}\right)\left(\frac{\gamma}{s}(c_t - sc + Dv) - c\right) + k_s c - \varepsilon(J-c)\right), \\ \frac{dc_t}{d\xi} &= \varepsilon(J-c), \end{aligned} \tag{3.7}$$

where c and v are the fast variables and c_t is the slow variable, with ε indicating the separation of time scales between the fast and slow variables. The variable c_t can be regarded as the total number of moles of calcium in the cell, divided by the cytoplasmic volume.

One can verify that system (3.7) has a unique equilibrium solution E^J given by

$$E^J = (J, 0, c_t^J) := \left(J, 0, \frac{s\left(k_s + \alpha + k_f \frac{J^2}{J^2+\varphi_1^2}\frac{\varphi_2}{J+\varphi_2}\right)J}{\gamma\left(\alpha + k_f \frac{J^2}{J^2+\varphi_1^2}\frac{\varphi_2}{J+\varphi_2}\right)} + sJ\right).$$

Hence, a solitary wave of system (3.2) corresponds to a orbit of system (3.7) homoclinic to E^J. A periodic wave solution of system (3.2) corresponds to a periodic orbit of system (3.7).

3.3.4 Homoclinic bifurcations in the singular limit

Section 2.5.2 discussed typical phase portraits of homoclinic orbits of the FHN model in the singular limit. We can obtain typical phase portraits of homoclinic and heteroclinic orbits of the prototypical calcium model in the singular limit in a similar way. In this section, we show how to construct these orbits numerically. A parallel theoretical construction can also be done; Tsai et al. (2012) will contain more details.

Note that in the singular limit, equilibrium solutions of equations (3.7) are not unique, but for a given J value and $\varepsilon > 0$ there is only one equilibrium, which we denote as E^J. In particular, for a given J, equations (3.7) have an equilibrium, E^J, and two types of singular homoclinic orbits associated with the equilibrium, denoted as Γ_{f0} and Γ_{s0}, exist when $\varepsilon = 0$. A schematic phase portrait showing Γ_{f0} and Γ_{s0} is given in panel (a) of Fig. 3.7.

Given J, the orbit Γ_{f0} typically consists of four pieces: a fast jump in the plane $\{c_t = c_t^J\}$ from $c = J$ to a point denoted as c^+ on the right branch of the c-nullcline; a segment of the right branch of the c-nullcline; a second jump from the local minimum of the c-nullcline to a point on the left branch of the c-nullcline; and a segment of the left branch of the c-nullcline back to the equilibrium point E^J. The phase portrait of this type of homoclinic orbit of the prototypical calcium model is similar to that of a minimal cardiac cell model discussed in Beck et al. (2008).

From the construction of the orbit Γ_{f0}, one observes that finding the curve of homoclinic orbits Γ_{f0} is equivalent to finding parameter values for which there is a curve of heteroclinic connections from $c = J$ to $c = c^+$ in the plane $\{c_t = c_t^J\}$, as the second jump occurs automatically near the local minimum point of the c-nullcline and gives no extra constraints on parameter values. We can find the locations of the singular homoclinic solutions Γ_{f0} numerically by solving the following differential algebraic equations:

$$\begin{aligned}
\frac{dc}{d\xi} &= v, \\
\frac{dv}{d\xi} &= \frac{1}{D}\left(sv - \left(\alpha + k_f\frac{c^2}{c^2+\varphi_1^2}\cdot\frac{\varphi_2}{c+\varphi_2}\right)\left(\frac{\gamma}{s}(c_t - sc + Dv) - c\right) + k_s c\right), \\
c_t &= c_t^J,
\end{aligned} \tag{3.8}$$

subject to the following boundary conditions:

$$(c,v) \to (J,0) \;\text{ as }\; \xi \to -\infty, \quad \text{and} \quad (c,v) \to (c^+,0) \;\text{ as }\; \xi \to \infty. \tag{3.9}$$

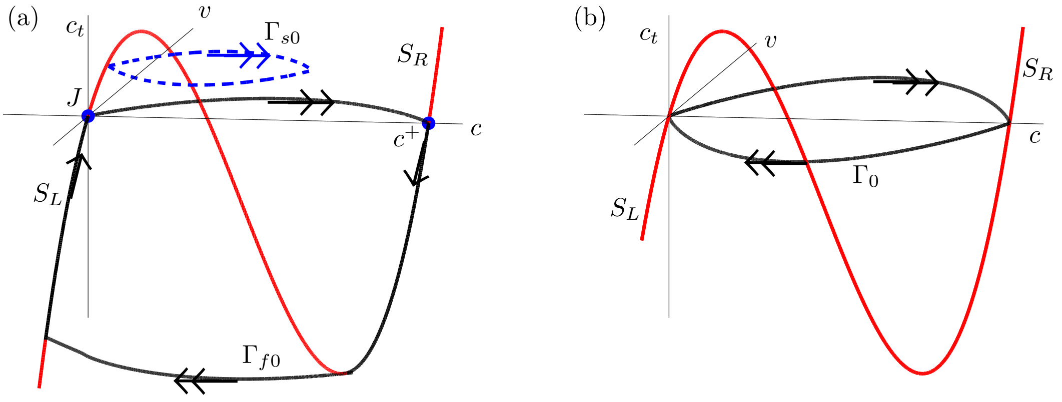

Figure 3.7: (a) Schematic phase portraits of singular homoclinic orbits Γ_{f0} and Γ_{s0} for (3.8) in the singular limit of the calcium model. The two blue dots mark the points $c = J$ and $c = c^+$. (b) Schematic phase portrait of a heteroclinic cycle Γ_0, which is the coalescence of singular homoclinic orbits Γ_{f0} and Γ_{s0} at $J \approx 0.045$.

The other type of singular orbit Γ_{s0} can be found as a planar homoclinic orbit to the equilibrium point $(J, 0)$ in the phase plane $\{c_t = c_t^J\}$. A typical phase portrait for Γ_{s0} is also shown in panel (a) of Fig. 3.7. Specifically, we can find the location of the singular homoclinic solution Γ_{s0} numerically by solving the differential algebraic equations (3.8) subject to the following boundary conditions:

$$(c, v) \to (J, 0) \;\text{ as }\; \xi \to \pm\infty. \tag{3.10}$$

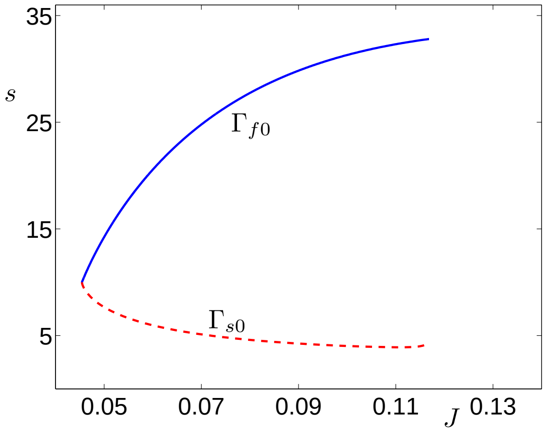

Figure 3.8: Homoclinic bifurcation curve in the (J, s) parameter plane for (3.8) in the singular limit of the prototypical calcium model with parameter values given in Table. 3.2. The blue solid curve shows the branch of singular homoclinic orbits Γ_{f0} and the red dashed curve shows the branch of singular homoclinic orbits Γ_{s0}.

We obtain the locus of the singular homoclinic bifurcations for the above boundary value problems with the help of Lin's algorithm (Krauskopf and Riess, 2008) implemented with the software package AUTO. We find that, at least for the parameter values used to draw Fig. 3.8, the homoclinic bifurcation curve is still C-shaped in the parameter plane, as shown in Fig. 3.8. At the leftmost point of the C-shaped curve, the two different types of homoclinic orbit, Γ_{f0} and Γ_{s0}, coalesce to a singular orbit Γ_0. The phase portrait of the orbit Γ_0 is shown in panel (b) of Fig. 3.7. Fig. 3.8 gives numerical evidence for the existence of singular homoclinic orbits for equations (3.7). A proof of the existence of singular homoclinic orbits for a range of parameter values will be given in Tsai et al. (2012).

3.3.5 Hopf bifurcations in the singular limit

As discussed in the previous section, the singular limit of the calcium model (3.7) can be represented by the differential algebraic equations (3.8), and we can find the position of the Hopf bifurcation numerically for equations (3.8) by using the basic bifurcation continuation routine in AUTO. The Hopf bifurcation of the calcium equations (3.8) is shown in Fig. 3.9. The existence of the U-shaped curve of Hopf bifurcations in the (J, s) parameter plane is proven analytically in the singular limit in Tsai et al. (2012). We can also try to examine the criticality of the Hopf bifurcation in the singular limit numerically by computing the associated first Lyapunov coefficient (Kuznetsov, 1998). The bifurcation package MatCont (Govaerts and Kuznetsov, 2008) can be used to compute the first Lyapunov coefficient. More information about the calculation of the first Lyapunov coefficient is included in section 5.3.1. As it turns out, the numerical results indicate that the first Lyapunov coefficients are greater than zero so that the Hopf bifurcations are generally subcritical in the singular limit. This is different from the case of FHN model in which the Hopf bifurcations are degenerate generically in the singular limit. We will discuss differences between the Hopf bifurcations for the FHN model and the calcium model in more detail in chapter 4.

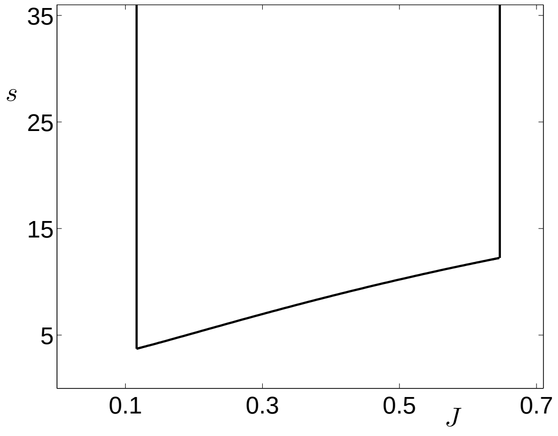

Figure 3.9: Hopf bifurcation curve in the (J, s) parameter plane of equations (3.8) in the singular limit for the prototypical calcium model with parameter values given in Table. 3.2. The Hopf bifurcations are subcritical on the U-shaped curve.

3.3.6 Comparison between waves of the full system and the singular limit

As shown in the previous section, singular homoclinic orbits for equations (3.8) in the singular limit of the calcium model are found numerically to lie on a C-shaped curve of the parameter plane. We can also numerically compute the homoclinic locus at $\varepsilon = 0.01$ and $\varepsilon = 0.1$ for the non-singular calcium equations (3.7) with the HomCont routine in AUTO; these bifurcation curves are plotted in Fig. 3.10. One can observe from the figure that, as the small parameter ε tends towards zero, the homoclinic bifurcation curve of the full system tends towards the singular homoclinic curve in the (J, s) parameter plane.

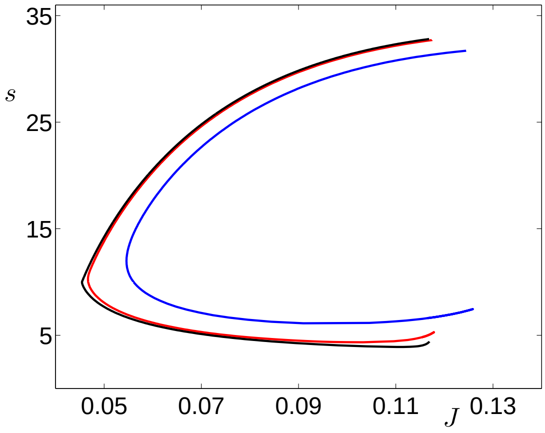

Figure 3.10: Homoclinic bifurcation curves in the (J, s) parameter plane for various different values of ε in the prototypical calcium model with parameter values given in Table. 3.2. The blue and red C-shaped curves represent the homoclinic bifurcations at $\varepsilon = 0.1$ and $\varepsilon = 0.01$, respectively; the black curve represents the homoclinic curve in the singular limit.

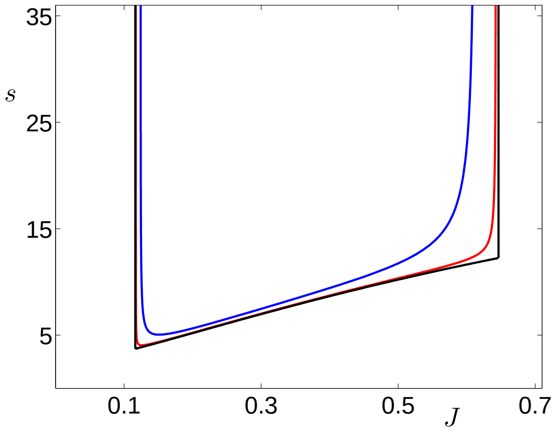

Figure 3.11: Hopf bifurcation curves in the (J, s) parameter plane for various different values of ε in the prototypical calcium model with parameter values given in Table. 3.2. Specifically, the blue and red curves represent the Hopf bifurcation curve for $\varepsilon = 0.1$ and $\varepsilon = 0.01$, respectively; the black curve represents the Hopf curve in the singular limit.

We can find the locus of the Hopf bifurcation with the basic bifurcation continuation routine in AUTO in the (J, s) parameter plane for the full system (3.7) as well as the singular limit system (3.8). The numerical results of the Hopf bifurcation curves are shown in Fig. 3.11. Note that as the small parameter ε moves towards zero, the Hopf bifurcation curve of the full system tends towards the curves of Hopf bifurcation in the singular limit. The criticality of the Hopf bifurcation can be determined numerically by Matcont (Govaerts and Kuznetsov, 2008). Interestingly, the numerical results show that for fixed wave speed s, the criticality of the Hopf bifurcation in the singular limit may not be the same as that of the Hopf bifurcation in the full system for any $\varepsilon > 0$. For example, for fixed $s = 15$, the Hopf bifurcation in the full system is supercritical while the Hopf bifurcation in the singular limit is subcritical, as shown in Fig. 3.12. We will discuss the reason for this difference in more detail in chapter 5.

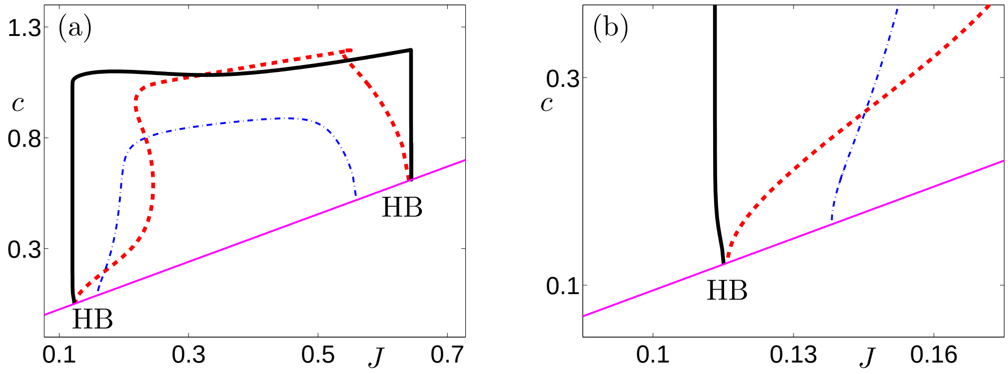

Figure 3.12: Partial bifurcation diagram for equations (3.7) with various values of ε, $s = 15$ and other parameter values as in Table. 3.2. The pink thin solid curve shows the position of the unique equilibrium of the model. This equilibrium has two Hopf bifurcations (labelled HB). The remaining curves show the maximum c-values attained by the periodic orbits created in the Hopf bifurcations, for three choices of ε, i.e., $\varepsilon = 10^{-1}$, $\varepsilon = 10^{-3}$ and $\varepsilon = 0$ (fast subsystem) on the blue thin dashed, red thick dashed and black thick solid curves, respectively. Panel (b) shows an enlargement near the left Hopf bifurcations in panel (a). Note that the left-most Hopf bifurcation in panel (a) is subcritical (when $\varepsilon = 0$) but the bifurcation is supercritical for all $\varepsilon > 0$.

The relative positions of the homoclinic and Hopf bifurcation curves in the full system and the singular limit are shown in Fig. 3.13. Note that, in the singular limit, the homoclinic curve appears to terminate on the Hopf bifurcation curve at both ends, but, as discussed in section 3.3.2, for sufficiently small $\varepsilon > 0$, the upper end of the homoclinic curve may stop at a supercritical Hopf bifurcation point on the Hopf curve, while the lower end of the homoclinic curve must turn around before reaching a subcritical Hopf bifurcation point, possibly due to the presence of the EP1t point.

In summary, we study the prototypical calcium model to give insight into the dynamics of a range of calcium models. We have done numerical simulations on a variety of calcium models and, as found by Champneys et al. (2007), obtained similar features in their bifurcation sets. In light of the numerics, we choose a representative calcium equations (3.7) to analyze because its form is simple enough to find the equilibrium solutions and some features of the equations analytically.

In the prototypical calcium model, with comparison of the bifurcation sets between its singular limit and the full system, we can observe that the homoclinic bifurcation and Hopf bifurcation curves of the full system appear to arise as perturbations of singular homoclinic bifurcation and Hopf bifurcation curves. Thus, examination of the

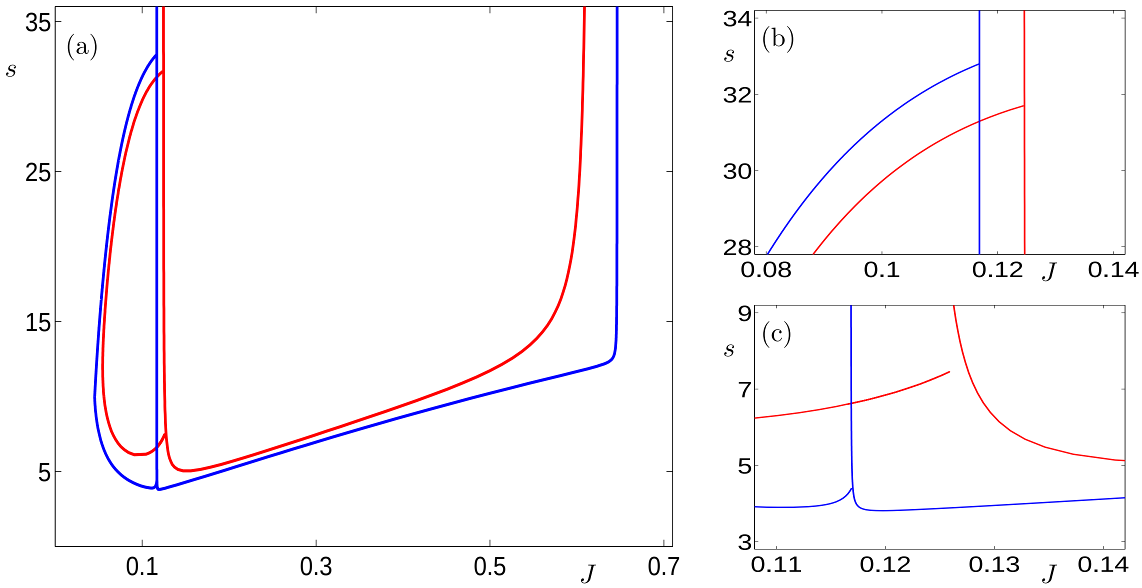

Figure 3.13: (a) Relative positions of homoclinic and Hopf bifurcation curves in the (J, s) parameter plane for different values of ε in the prototypical calcium model (3.7) with parameter values given in Table. 3.2. The curves in blue stand for the homoclinic and Hopf bifurcation curves in the singular limit and the red curves represent the homoclinic and Hopf bifurcation curves for the full system with $\varepsilon = 0.1$. (b) A zoom near the upper end of the C-shaped homoclinic curves in panel (a). (c) A zoom near the lower end of the C-shaped homoclinic curves in panel (a).

singular limit of the prototypical calcium model provides useful information about the bifurcation structure in the full system. A more rigorous theoretical examination of the correspondence between the singular limit and the full system is beyond the scope of this thesis, but some partial results have been proved by J. C. Tsai and has been submitted for publication (Tsai et al., 2012). Similarity of dynamics between calcium models and their singular limits has also been investigated by Harvey et al. (2010, 2011). Just as for the FHN system, the singular limit gives information about basic features of the full bifurcation set. More complex dynamics (e.g., homoclinic snaking) appear in the full system; it is not yet known in detail how these features unfold from the singular limit as ε is increased from zero.

Chapter 4

Comparison between waves of the FHN model and the prototypical calcium model

In chapters 2 and 3, we discussed wave solutions in two important biophysical models, namely the FHN model and a prototypical model of intracellular calcium dynamics. The FHN model is a canonical excitable system widely regarded as a prototypical voltage model (Rocsoreanu et al., 2000; Keener and Sneyd, 2008), and it was argued in chapter 3 that the calcium model is a good representative of models of intracellular calcium dynamics in non-excitable cells.

In this chapter, we compare wave solutions of these two representative models. The aim is to see whether the dynamics of the FHN model is similar enough to that of the calcium model for the FHN model to be used as a qualitative prototype for calcium models.

To this end, we consider different forms of the two systems used in the different sections as follows. In section 4.1, we compare the two systems in the absence of diffusion. The FHN model becomes

$$\begin{aligned} \frac{du}{dt} &= u(u-1)(\alpha - u) - w + p, \\ \frac{dw}{dt} &= \varepsilon(u - \gamma w), \end{aligned} \tag{4.1}$$

and the calcium model becomes

$$\begin{aligned} \frac{dc}{dt} &= \left(\alpha + k_f \frac{c^2}{c^2+\varphi_1^2} \cdot \frac{\varphi_2}{c+\varphi_2}\right)(\gamma(c_t - c) - c) - k_s c + \varepsilon(J - c), \\ \frac{dc_t}{dt} &= \varepsilon(J - c). \end{aligned} \tag{4.2}$$

In section 4.2, we make comparison of the two systems with diffusion. To facilitate the study of the wave solutions, similar to the discussion in previous chapters, we transform the FHN and the prototypical calcium systems into travelling wave coordinates and get systems in the following forms. The FHN system is

$$\begin{aligned}
\frac{du}{d\xi} &= v, \\
\frac{dv}{d\xi} &= \frac{1}{D_c}(sv - u(u-1)(\alpha - u) + w - p), \\
\frac{dw}{d\xi} &= \frac{\varepsilon}{s}(u - \gamma w),
\end{aligned} \tag{4.3}$$

and the calcium system is

$$\begin{aligned}
\frac{dc}{d\xi} &= v, \\
\frac{dv}{d\xi} &= \frac{1}{D}\left(sv - \left(\alpha + k_f \frac{c^2}{c^2+\varphi_1^2} \cdot \frac{\varphi_2}{c+\varphi_2}\right)\left(\frac{\gamma}{s}(c_t - sc + Dv) - c\right) + k_s c - \varepsilon(J-c)\right), \\
\frac{dc_t}{d\xi} &= \varepsilon(J - c),
\end{aligned} \tag{4.4}$$

In section 4.3, we compare the singular limits of the two models via examination of their fast subsystems. The fast subsystem of the FHN model is

$$\begin{aligned}
\frac{du}{d\xi} &= v, \\
\frac{dv}{d\xi} &= \frac{1}{D_c}(sv - u(u-1)(a - u) + w - p),
\end{aligned} \tag{4.5}$$

and the fast subsystem of the calcium model is

$$\begin{aligned}
\frac{dc}{d\xi} &= v, \\
\frac{dv}{d\xi} &= \frac{1}{D}\left(sv - \left(\alpha + k_f \frac{c^2}{c^2+\varphi_1^2} \cdot \frac{\varphi_2}{c+\varphi_2}\right)\left(\frac{\gamma}{s}(c_t - sc + Dv) - c\right) + k_s c\right).
\end{aligned} \tag{4.6}$$

In section 4.4, we summarise our results from comparison of the models, and draw the conclusion that there are similarities between the dynamics of these two models, but also significant differences.

4.1 Comparison in the absence of diffusion

We begin our comparison with the space-clamped version of these two models, i.e., where there are no diffusion terms in the models. From the physiology of the cell, we understand that variation in total calcium is slow compared to the rapid variation of cytoplasmic calcium concentration. This important feature of the calcium dynamics allows us to treat the total calcium c_t as a convenient slow variable. Therefore, the dynamics of intracellular calcium can be described by the slow-fast system (4.2). In the FHN model, the variation of the membrane potential occurs much faster than the negative feedback of the gating conductance. The separation of the time scales in the models is indicated by the small parameter ε in (4.1) and (4.2).

We point out the similarities between the FHN equations (4.1) and the prototypical calcium equations (4.2) in the case of no diffusion. Both of the models are two dimensional and they have a clear separation of time scales between fast and slow variables. Moreover, both of the models have cubic-shaped nullclines (u-nullcline for the FHN model, c-nullcline for the calcium model) which allow the models to exhibit excitability, and the nullclines of the slow variables in both systems are straight lines. Therefore, these two equations superficially display quite strong similarities.

We show comparisons of typical time series and phase portraits of the two models in Fig. 4.1 and Fig. 4.2, respectively. Bifurcation diagrams for the equations are depicted in Fig. 4.3. Note that all these figures display similar features; and we can argue that two equations without diffusion have qualitatively similar dynamics.

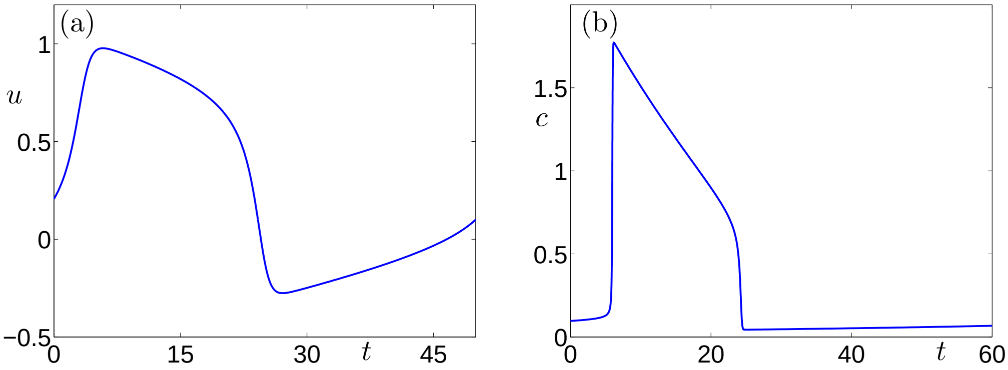

Figure 4.1: (a) Time series of the FHN equations (4.1) without diffusion at $p = 0.1$, $D_c = 0$ and other parameters as in (2.2). (b) Time series of the calcium equations (4.2) without diffusion at $J = 0.15$, $D = 0$, and other parameters as in Table. 3.1.

4.2 Diffusion appears in the models differently

In this section, we show that inclusion of diffusion affects the two models in different ways.

For the FHN model, the slow variable w represents the gating variable of a ionic current. From the modelling assumptions, we know that the gating variable is uniformly distributed along the spatial direction, which means that the derivative of the gating variable with respect to the spatial variable x is equal to zero ($\frac{\partial^2 w}{\partial x^2} = 0$). In other words, the diffusion only affects the fast variable but not the slow variable. Thus,

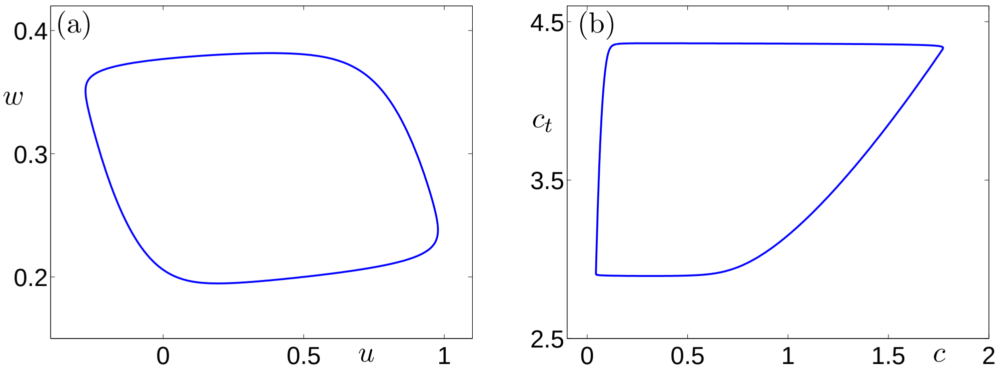

Figure 4.2: (a) Phase portrait corresponding to the time series in panel (a) of Fig. 4.1. (b) Phase portrait corresponding to the time series in panel (b) of Fig. 4.1.

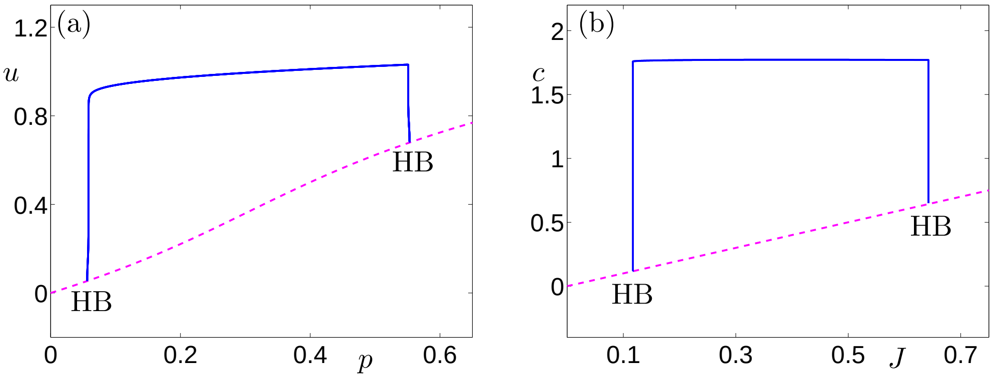

Figure 4.3: (a) Partial bifurcation diagram of the FHN equations (4.1) with parameters D_c=0 and other parameters given in (2.2). The magenta dashed curve shows the position of the unique equilibrium of the model. This equilibrium has two Hopf bifurcations (labelled HB). The blue curve show the maximum u-value attained by the periodic orbits created in the Hopf bifurcations. Both of the Hopf bifurcations are subcritical. (b) Partial bifurcation diagram of the calcium equations (4.2) with parameters D=0 and other parameters given in Table. 3.1. The magenta dashed curve shows the position of the unique equilibrium of the model. This equilibrium has two Hopf bifurcations (labelled HB). The blue curve show the maximum c-value attained by the periodic orbits created in the Hopf bifurcations. The Hopf bifurcation on the left is supercritical and the Hopf bifurcation on the right is subcritical.

we can write down the FHN system with diffusion in travelling wave coordinates as equations (4.3).

However, as noted in chapter 1, for the prototypical calcium model the diffusion affects the slow variable c_t. In particular, the slow variable c_t represents the total calcium of the cell, which consists of two parts: the cytoplasmic calcium c and the calcium in the internal compartment ER c_e. We assume that calcium diffusion occurs in the cytoplasm, which implies that the diffusion affects both the fast variable c and the slow variable c_t and these two variables are intricately linked. We have further assumed throughout the thesis that the calcium in ER does not diffuse spatially, in which case we can write down equations (4.4) to describe the dynamics of intracellular calcium with the spatial variation in travelling wave coordinates.

Note that diffusion enters the FHN model and the calcium model differently. The diffusion term only affects the evolution of the fast variable in the FHN model, while the diffusion term affects the evolution of both the fast and the slow variable in the calcium model. As a result, in the travelling wave coordinates, equations (4.3) of FHN model has no nonlinear coupling term between the fast variables u and v, while equations (4.4) of the calcium model has a nonlinear coupling term between the fast variables

$$\left(\alpha + k_f \frac{c^2}{c^2+\varphi_1^2} \cdot \frac{\varphi_2}{c+\varphi_2}\right) \left(\frac{\gamma}{s}(c_t - sc + Dv) - c\right). \tag{4.7}$$

Different behaviours between these two models might be expected in the singular limits, and hence in the full systems. In the next section, we investigate the dynamics near the singular limit to look for the similarities and differences between the fast subsystem of the FHN model (4.5) and the fast subsystem of the calcium model (4.6).

4.3 Comparison between systems in their singular limits

As discussed in section 2.5.1, we can understand the dynamics of the full system by way of the dynamics in the singular limit. The fast subsystem in the singular limit can be obtained by setting the small parameter ε to zero, and fixing the slow variable to its equilibrium value. This yields equations (4.5) and (4.6) for the fast subsystems of the FHN model and the calcium model, respectively.

4.3.1 Comparison of Hopf bifurcations

In chapter 2, we displayed some numerical and analytical results to show that at the Hopf bifurcations of the FHN system, the imaginary parts of the eigenvalues become unbounded as $\varepsilon \to 0^+$, and the first Lyapunov coefficients will also become zero. On the other hand, numerical evidence shows that the imaginary parts of the eigenvalues at the Hopf bifurcations of the prototypical calcium model (4.6) are bounded as $\varepsilon \to 0^+$, and the associated first Lyapunov coefficients are also bounded away from zero as ε tends to zero. The FHN fast subsystem (4.5) has singular Hopf bifurcations on the vertical branches of the Hopf bifurcation curve (Baer and Erneux, 1986, 1992) and degenerate Hopf bifurcations on the horizontal branch of the Hopf bifurcation curve (the first Lyapunov coefficient is zero) in the singular limit, while the Hopf bifurcation of the calcium fast subsystem model (4.6) is subcritical. However, the difference in nature of the Hopf bifurcations in the two singular limits may not be reflected in a significant difference in the non-singular models other than the steepness of the branches of periodic orbits in the bifurcation diagrams.

We compare the form of equations (4.5) and (4.6) to look for the reason for the different types of Hopf bifurcations. The difference seems to arise from the way diffusion couples the fast and slow variables in the two models, as we will now show. In particular, a general two-dimensional planar smooth system at a Hopf bifurcation can be written in the following form (some changes of coordinates may be needed):

$$\begin{pmatrix} \dot{x} \\ \dot{y} \end{pmatrix} = \begin{pmatrix} 0 & \omega \\ \omega & 0 \end{pmatrix} \begin{pmatrix} x \\ y \end{pmatrix} + \begin{pmatrix} f(x,y) \\ g(x,y) \end{pmatrix}. \tag{4.8}$$

The first Lyapunov coefficient of Hopf bifurcation can be calculated with the following formula (Guckenheimer and Holmes, 1983):

$$\begin{aligned} 16 l_1 = \mathrm{Re}\ & \left[(f_{xxx} + f_{xyy} + g_{xxy} + g_{yyy}) + \right. \\ & \left. \tfrac{1}{\omega}\big(f_{xy}(f_{xx} + f_{yy}) - g_{xy}(g_{xx} + g_{yy}) - f_{xx}g_{xx} + f_{yy}g_{yy}\big)\right]. \end{aligned} \tag{4.9}$$

If $l_1 > 0$ then the Hopf bifurcation is subcritical; if $l_1 < 0$ then the Hopf bifurcation is supercritical.

Applying formula (4.9) to the fast subsystem of FHN system (4.5) in the singular limit, it follows that the value for the Lyapunov coefficient l_1 is always equal to zero. On the other hand, applying formula (4.9) to the fast subsystem of the calcium system (4.6) in the singular limit, it follows that the value for l_1 is generally not equal to zero. We note that the presence of the coupling term between variables c and v, as shown in (4.7), in the singular limit of the prototypical calcium model (4.6) leads to the Hopf bifurcation being generally non-degenerate. This is a significant difference compared to the dynamics of the singular limit of the FHN equations (4.5). Referring back to the original PDEs calcium model, we note that the presence of the coupling term in the model is due to the fact that the diffusion affects both fast and slow variables. In particular, the diffusion appears in both fast and slow variables so that there is a coupling term between c and v in the calcium equations (4.6) when the system is transformed into the travelling wave coordinates, and this in turn results in the Hopf bifurcation being non-degenerate. This is different from the degenerate Hopf bifurcation observed in the fast subsystem of the FHN model (4.5).

Note that there are other significant differences between equations (4.5) and (4.6). Firstly, the nonlinear function in FHN system $f(u) = u(u-1)(\alpha - u)$ is particularly simple, while the nonlinear functions in the prototypical calcium system are rather complex. Secondly, the FHN system has a symmetry: the equations are equivariant under the transformation

$$
\begin{aligned}
&u \to \frac{2}{3}(1+\alpha) - u,\ v \to -v,\ w \to \frac{2}{3\gamma}(1+\alpha) - w, \\
&I \to \frac{2}{3}(1+\alpha)\Big[\frac{1}{\gamma} - \frac{(2-\alpha)(1-2\alpha)}{9}\Big] - I.
\end{aligned} \tag{4.10}
$$

We could use a more general functional form of $f(u)$ instead of the simple cubic function, in which case the symmetry of FHN system may be lost. However, even with such changes, inspection of (4.9) shows that the first Lyapunov coefficient l_1 will still be zero in the FHN fast subsystem (4.5). This demonstrates that neither the simple functional form of f nor the symmetry of the FHN model is an important factor in the difference in the Hopf bifurcations in systems (4.5) and (4.6).

4.3.2 Comparison of homoclinic orbits

The phase portraits of the homoclinic orbits of the FHN model and the prototypical calcium model in the singular limit are discussed in sections 2.5.2 and 3.3.5, respectively. We recall that both models have singular homoclinic orbits that consist of four pieces, namely two fast jumps between different branches of the critical manifold and two segments of the critical manifold; the following discussion is about these homoclinic orbits, not the other type of homoclinic orbits which have no branches on the critical manifold.

The symmetry of the FHN model, specified in (4.10), results in a qualitatively different phase portrait of the homoclinic orbit from that of the prototypical calcium model in the singular limit. In particular, an important difference is the nature of the second jump. For the prototypical calcium model, the second jump of the homoclinic orbit occurs at the local minimum of the critical manifold where normal hyperbolicity is lost. The phase portrait of the homoclinic orbit is similar to that of a minimal cardiac cell model analyzed in Beck et al. (2008). On the other hand, the FHN model has a symmetry, which implies that the position of the second jump point is symmetric to the first jump point. Thus, the second jump does not occur at the local minimum of the critical manifold. This difference of the phase portraits of homoclinic orbits between FHN model and that of the minimal cardiac cell model is also observed and reported in Beck et al. (2008).

Different mechanisms in the two fast subsystems (4.5) and (4.6) in the singular limit give rise to the qualitatively different phase portraits for these singular homoclinic orbits. However, these two types of singular homoclinic bifurcations are both of codimension-one, and both singular homoclinic orbits perturb to similar homoclinic orbits in the full system. Specifically, as ε is increased from zero, the homoclinic orbits in the full system move $O(\varepsilon)$ away from the singular homoclinic orbits. Therefore, the difference of the phase portraits of the homoclinic orbits between the FHN model and the calcium model in the singular limit do not appear to produce significant differences in the homoclinic orbits in the full systems.

Furthermore, the symmetry of the FHN model also indicates that there are two symmetric C-shaped homoclinic curves in the parameter plane, as shown in Fig. 2.11. On the other hand, the numerical results in Tsai et al. (2012) indicate that the calcium model seems to also have C-shaped homoclinic curves one on each side of the U-shaped Hopf curve, but these two C-shaped curves are not symmetric to each other. This difference again is probably not significant for dynamics to the left of the Hopf bifurcation curve in the full system.

4.4 Summary

Although there are many models of intracellular calcium dynamics for different types of cells, they seem to share similar features. In particular, the U-shaped curve of Hopf bifurcations and the C-shaped curve of homoclinic orbits are structures that are preserved across a wide variety of calcium wave models (Champneys et al., 2007). Thus it is reasonable to suppose that the simplified prototypical model, which also has these characteristics, has captured important basic features of these models. Superficial similarities between the FHN system and the prototypical calcium model then give rise to the question of whether the canonical FHN system itself captures the basic features of the calcium models.

One prominent similarity between systems (4.3) and (4.4) is that they have a similar CU bifurcation structure. As discussed in chapters 2 and 3, the CU structure of these systems is mainly due to the cubic-shaped critical manifold in the phase space. The prototypical calcium model and the FHN model both have this important ingredient in the singular limit so they have similar CU structure in the full system for sufficiently small ε.

From the analysis in section 4.1 we see that without diffusion the FHN model (4.1) and the prototypical calcium model (4.2) have solutions with similar qualitative behaviour. However, the spatial diffusion terms affect the two types of model differently, and one consequence is that there exists a coupling term between c and v in the prototypical calcium model while no such coupling term exists in the FHN model. In section 4.2 we showed that the presence of the coupling term will make a difference to the overall dynamics of the system. Specifically, the Hopf bifurcation of the FHN fast subsystem (4.5) is generally degenerate while the Hopf bifurcation of the calcium fast subsystem (4.6) is generally not degenerate. Therefore, with the spatial diffusion term the FHN model and the prototypical calcium model have qualitatively different dynamics in the singular limit, which may be the source of differences in the full system.

Moreover, the FHN model has a symmetry which implies that the position and the phase portrait of the homoclinic orbits is quite different from those of the prototypical calcium model in the singular limit. However, these differences due to the symmetry of the FHN system do not have a big impact on the dynamics of these two models in the full systems.

Chapter 5

Changes in the criticality of Hopf bifurcations due to model reduction techniques

It is often the case that higher-dimensional models are more difficult to analyze than lower-dimensional models. Therefore, one would frequently like to reduce the dimension of a model to simplify the analysis. Various model reduction methods have been introduced for simplifying excitable systems, including commonly used techniques such as making a quasi-steady state approximation and using GSPT.

However, some difficulties may arise when model reduction techniques are used. For example, in chapter 3 it was noticed that for the calcium model studied there, the Hopf bifurcation has different criticality in the singular limit and in the full system for any small $\varepsilon > 0$. Investigation of this difference lead to the work described in this chapter, which is an analysis of changes in the criticality of Hopf bifurcations due to model reduction techniques.

The chapter is structured as follows. In section 5.1, we first review some basic information about two commonly used model reduction techniques for biophysical models with multiple time scales, namely the quasi-steady state approximation and GSPT. In section 5.2, we investigate the quasi-steady state approximation in detail and determine conditions under which use of this technique can be rigorously justified by centre manifold theory. In section 5.3, we focus on Hopf bifurcations in slow-fast biophysical systems. In particular, we show that the criticality of a Hopf bifurcation in a model may be changed when the reduction techniques are applied. The findings are summarized in section 5.4.

The work presented in this chapter has been published in Zhang et al. (2011) in collaboration with V. Kirk, J. Sneyd and M. Wechselberger.

5.1 Model reduction methods and criticality of Hopf bifurcations

Many models of physiological processes have the feature that one or more variables evolve much faster than the other variables. Such biophysical processes involving variables of different time scales include neural activities such as bursting and spiking of membrane potentials (Hodgkin and Huxley, 1952a,b,c,d), and intracellular calcium signalling (Keener and Sneyd, 2008).

The model reduction technique of setting some fast variables to their quasi-steady states, known as quasi-steady state approximation, is used in many conductance based physiological models with multiple time scales. One well-known example of use of a quasi-steady state approximation occurs in Rinzel (1978, 1985), in which the HH equations (Hodgkin and Huxley, 1952a,b,c,d) are reduced to a simplified model which captures the qualitative behaviour of the neural dynamics observed in the full model. One of Rinzel's reduction steps is to set the fast gate variable m instantaneously to its quasi-steady state value $m = m_\infty(V)$. However, the approach is not always mathematically justified. In section 5.2 we give conditions under which such a model reduction technique in a slow-fast system can be justified mathematically. As an example, we will show in section 5.2.1 that this reduction step is mathematically justified in the HH model, and point out some potential problems of this technique.

In many physiological models we are interested in the onset of oscillations, i.e., in the existence and criticality of Hopf bifurcations. The position of Hopf bifurcations in a model can be determined from a computation of the eigenvalues of the Jacobian matrix of equilibrium solutions in the system, but it is more complicated to determine the criticality of a Hopf bifurcation. For a general system, criticality of a Hopf bifurcation is determined by the sign of the first Lyapunov coefficient (Kuznetsov, 1998). More information about the computation of the first Lyapunov coefficient of a general system is contained in section 5.3.1

The criticality of the Hopf bifurcation plays an important role in the overall dynamics, so it is desirable that the model reduction should be performed in such a way that a Hopf bifurcation in the full model corresponds to a Hopf bifurcation in the reduced model and that the criticality of the Hopf bifurcations in the full and reduced models match. However, we will show that model reductions may sometimes cause problems, in that the reduced model may have a Hopf bifurcation of a different criticality to that in the full system.

For a physiological model represented as a singularly perturbed system there is another potential trap related to the criticality of a Hopf bifurcation if we wish to apply GSPT in such slow-fast systems. Suppose the full system possesses a Hopf bifurcation that persists in the singular limit as a Hopf bifurcation of the fast subsystem. We may want to know if one can relate the criticality of the Hopf bifurcation obtained in the fast subsystem to the criticality of the Hopf bifurcation in the full problem. Care needs to be taken because, very close to the Hopf bifurcation, the time scale associated with the bifurcating directions (i.e., corresponding to real part of the complex conjugate pair of eigenvalues) will be comparable with the time scale(s) associated with the slow variable(s), which can give rise to problems if we wish to apply GSPT in this case.

We study the criticality of Hopf bifurcations in typical physiological models with multiple time scales, and show that the singular limit of the first Lyapunov coefficient of a Hopf bifurcation is not always equal to the first Lyapunov coefficient of the Hopf bifurcation in the corresponding fast subsystem, as is observed in the calcium model discussed in chapter 3. Specifically, we show that in some cases in which a Hopf bifurcation involves the fast variables, all the information needed to determine the criticality of the Hopf bifurcation is contained in the fast subsystem but in other cases there is crucial information in the slow dynamics as well. In such cases, a small perturbation of the slow dynamics can change the criticality of the Hopf bifurcation, a seemingly counterintuitive result. Consequently, one cannot deduce, in general, the criticality of a Hopf bifurcation from the lower-dimensional fast subsystem in a slow-fast system.

5.2 A physiological model reduction technique for slow-fast systems

In this section we consider the quasi-steady state reduction technique widely used in physiological models that are described by slow-fast systems, and find conditions under which use of this technique is justified mathematically. Many physiological models, including many neural and calcium models, contain gating variables $m = (m_1, \ldots, m_j)$ which are thought to evolve faster than other processes in the model. In these cases, often the first step is to set the fast gating variables to their quasi-steady states, and thereby reduce the dimension of the model by the number of gating variables treated in this way. In the following, we show that this procedure can sometimes be justified by centre and invariant manifold theory.

Specifically, we are concerned with physiological models that are described in dimensionless form by slow-fast systems as follows:

$$\begin{aligned} \frac{dv}{dt} &= f(v, m, n, \mu, \varepsilon), \\ \frac{dm}{dt} &= h(v, m, n, \mu, \varepsilon), \\ \frac{dn}{dt} &= \varepsilon g(v, m, n, \mu, \varepsilon), \end{aligned} \tag{5.1}$$

where $(v, m) \in \mathbb{R} \times \mathbb{R}^j = \mathbb{R}^k$ are the fast variables, $n \in \mathbb{R}^l$ are the slow variables, f, g and h are $O(1)$ vector-valued functions, $\mu \in \mathbb{R}^m$ are system parameters, t represents the fast time and $\varepsilon \ll 1$ is the small perturbation parameter indicating the time scale separation. In neural models, v typically represents voltage, while in calcium models, v might represent the cytoplasmic calcium concentration. In biophysical (conductance based) models, m represents the fast gating variables and n represents the slow gating variables. In calcium models, the total calcium concentration might also be included in the slow variables n.

By taking the singular limit $\varepsilon \to 0$ in (5.1), we obtain the fast subsystem, which possesses, in general, an l-dimensional manifold of equilibria called the critical manifold,

$$S_0 := \{(v, m, n) : f(v, m, n, \mu, 0) = h(v, m, n, \mu, 0) = 0\}.$$

We are interested in different cases, depending on whether or not the critical manifold is normally hyperbolic, and, if it is not normally hyperbolic, the way in which normal hyperbolicity is lost.

Assumption 1 *The critical manifold S_0 is normally hyperbolic, i.e., all eigenvalues of the $(k \times k)$ Jacobian matrix of the fast subsytem evaluated along S_0,*

$$J = \left.\begin{pmatrix} \frac{\partial}{\partial v} f & D_m f \\ \frac{\partial}{\partial v} h & D_m h \end{pmatrix}\right|_{S_0},$$

have real parts not equal to zero.

If system (5.1) satisfies Assumption 1, then Fenichel theory (Fenichel, 1979) applies in this case. Specifically, according to the implicit function theorem, there exists an l-dimensional invariant manifold S_ε given as a graph $(v, m) = (\hat{V}(n, \mu, \varepsilon), \hat{M}(n, \mu, \varepsilon))$. This invariant manifold S_ε is a smooth $O(\varepsilon)$ perturbation of the critical manifold S_0. If we further assume that all eigenvalues of the Jacobian matrix of the fast subsystem along S_0 have real parts less than zero, then the theory says that a model reduction onto the slow manifold S_ε will recover the dynamics of the model after some initial transient time. In a biophysical model that would imply that the reduction of the fast gating variables m and, e.g., voltage or cytoplasmic calcium concentration v to their quasi-steady state correctly describes the flow on S_0.

Unfortunately, most physiological models have a critical manifold that is not normally hyperbolic and the reduction technique is not (globally) justified. In the following, we focus on the two main cases that cause loss of normal hyperbolicity of S_0: a fold or a Hopf bifurcation in the fast subsystem.

Assumption 2 *The Jacobian of the fast subsystem evaluated along S_0, i.e., the $(k \times k)$-matrix*

$$J = \left. \begin{pmatrix} \frac{\partial}{\partial v} f & D_m f \\ \frac{\partial}{\partial v} h & D_m h \end{pmatrix} \right|_{S_0},$$

has a zero eigenvalue along $F := \{(v, m, n) \in S_0 : \det(J) = 0, rank(J) = j = k - 1\}$ which is an $(l - 1)$-dimensional subset of S_0. We further assume that the other j eigenvalues all have real parts less than zero along S_0.

Generically, the manifold S_0 is folded near F if the following non-degeneracy conditions are fulfilled (evaluated along F):

$$w_l \cdot [(D^2_{(v,m)(v,m)}(f, h))(w_r, w_r)] \neq 0\,, \qquad w_l \cdot [D_n(f, h)] \neq 0 \tag{5.2}$$

where w_l and w_r denote the left and right null vectors of the Jacobian matrix J. Without loss of generality, we assume that the $(j \times j)$ sub-matrix $D_m h$ of the Jacobian J has full rank j. This implies that the right null vector w_r of J has a nonzero v-component, i.e., the nullspace is not in $v = 0$.

Next we make use of the fact that the determinant of the Jacobian J can be calculated by

$$\det(J) = \det(D_m h) \cdot \det \left(\frac{\partial}{\partial v} f - D_m f (D_m h)^{-1} \frac{\partial}{\partial v} h \right)$$

which follows from the block structure of J and the Leibniz formula for determinants. By Assumption 2, $\det(J) = 0$ along F. Since $D_m h$ has full rank, $\det(D_m h) \neq 0$ along F. Hence, the second determinant

$$\det \left(\frac{\partial}{\partial v} f - D_m f (D_m h)^{-1} \frac{\partial}{\partial v} h \right) = 0$$

along F which implies that $\frac{\partial}{\partial v} f - D_m f (D_m h)^{-1} \frac{\partial}{\partial v} h = 0$ along F, because it is a scalar. This reflects the zero eigenvalue of J. Since $\det(D_m h) \neq 0$, it also follows from the implicit function theorem that $h(v, m, n, \mu, \varepsilon) = 0$ can be solved as $m = M(v, n, \mu, \varepsilon)$. Note that in neural systems like the HH model, this functional relation is automatically given by the quasi-steady functions $m_i = M_i(v, n, \mu, \varepsilon) = m_{i,\infty}(v)$, $i = 1, \ldots, j$, for the fast gating variables. In the following we generalise a result that was presented in Rubin and Wechselberger (2007).

Proposition 1 *Given system* (5.1) *under Assumption 2, then there exists an $(l + 1)$-dimensional centre-manifold W^c in a neighbourhood of the fold F given as a graph*

$m = \hat{M}(v, n, \mu, \varepsilon)$. *System* (5.1) *reduced to* W^c *has the form*

$$\begin{aligned} \frac{dv}{dt} &= f(v, \hat{M}(v, n, \mu, \varepsilon), n, \mu, \varepsilon), \\ \frac{dn}{dt} &= \varepsilon g(v, \hat{M}(v, n, \mu, \varepsilon), n, \mu, \varepsilon). \end{aligned} \tag{5.3}$$

Proof. Since the right null vector w_r has a nonzero v-component it follows that the one-dimensional centre manifold of the fast subsystem of (5.1) can be locally given as a graph over the v-space. Thus the corresponding $(l + 1)$-dimensional centre manifold of the full system (5.1) is also locally given as a graph $m = \hat{M}(v, n, \mu, \varepsilon)$. Introducing the nonlinear coordinate transformation $\hat{m} = m - \hat{M}(v, n, \mu, \varepsilon)$ to system (5.1) gives

$$\begin{aligned} \frac{dv}{dt} &= f(v, m(v, \hat{m}, n, \mu, \varepsilon), n, \mu, \varepsilon), \\ \frac{d\hat{m}}{dt} &= h(v, m(v, \hat{m}, n, \mu, \varepsilon), n, \mu, \varepsilon) \\ &\quad -\frac{\partial}{\partial v}\hat{M}(v, n, \mu, \varepsilon) f(v, m(v, \hat{m}, n, \mu, \varepsilon), n, \mu, \varepsilon) \\ &\quad -\varepsilon D_n \hat{M}(v, n, \mu, \varepsilon) g(v, m(v, \hat{m}, n, \mu, \varepsilon), n, \mu, \varepsilon), \\ \frac{dn}{dt} &= \varepsilon g(v, m(v, \hat{m}, n, \mu, \varepsilon), n, \mu, \varepsilon), \end{aligned} \tag{5.4}$$

where the $(l + 1)$-dimensional centre manifold is now aligned with $\hat{m} = 0$. Hence, the flow on the $(l + 1)$-dimensional centre manifold is given by system (5.3). This proves the assertion.

Note that, in general, $M(v, n, \mu, \varepsilon) \neq \hat{M}(v, n, \mu, \varepsilon)$, i.e., solving $h(v, m, n, \mu, \varepsilon) = 0$ for $m = M(v, n, \mu, \varepsilon)$ does not yield the centre manifold for any ε, including in the singular limit when $\varepsilon = 0$. Thus, the dynamics of the reduced system obtained using the quasi-steady state reduction is, in general, different to the dynamics of the full system reduced to the centre manifold. The difference between M and $\hat{M}$ is due to two terms: an ε-dependent term that tends to zero in the singular limit and a term that is due to the function f. This last term will vanish on the critical manifold (where $f = 0$) and so on the critical manifold, $M \to \hat{M}$ as $\varepsilon \to 0$.

In summary, we have shown that making a quasi-steady state approximation can be mathematically justified if the critical manifold is normally hyperbolic or if it loses normal hyperbolicity in a simple fold and we are concerned with dynamics near the fold (Proposition 1). In these cases, quantitative changes may be introduced by the approximation but the qualitative features of the dynamics will be preserved.

5.2.1 The Hodgkin-Huxley model

As an example of the quasi-steady state reduction, we look at the Hodgkin-Huxley (HH) model again. This model is a four-dimensional system that in dimensionless form is given by

$$\begin{aligned}
\varepsilon\frac{dv}{dt} &= \bar{I} - m^3h(v-\bar{E}_{Na}) - \bar{g}_kn^4(v-\bar{E}_k) - \bar{g}_l(v-\bar{E}_L) \equiv S(v,m,n,h),\\
\varepsilon\frac{dm}{dt} &= \frac{1}{\tau_m t_m(v)}(m_\infty(v)-m) \equiv M(v,m),\\
\frac{dh}{dt} &= \frac{1}{\tau_h t_h(v)}(h_\infty(v)-h) \equiv H(v,h),\\
\frac{dn}{dt} &= \frac{1}{\tau_n t_n(v)}(n_\infty(v)-n) \equiv N(v,n),
\end{aligned} \tag{5.5}$$

where the fast variables are v and m (dimensionless membrane potential and activation gate of the sodium channel) and the slow variables are h and n (inactivation gate of the sodium channel and activation gate of the potassium channel). The quantity $\bar{I}$ is the bifurcation parameter (and is proportional to the applied external current I), and expressions for the functions $m_\infty(v)$, $n_\infty(v)$, $h_\infty(v)$, etc. and the values of constants used in (5.5) are given in Appendix A.

It was shown in Rubin and Wechselberger (2007) that the two-dimensional critical manifold, $S(v,m_\infty(v),n,h)=0$, is cubic shaped (in the physiologically relevant domain of the phase space) with two fold-curves $F^\pm$, attracting outer branches and a middle branch of saddle type. Furthermore, the vector field has a three-dimensional centre manifold $m=\hat{M}(v,n,h,\varepsilon)$ along each fold curve $F^\pm$, which is attracting. Hence, Proposition 1 can be applied in this example and the vector field reduced to the centre-manifold near each fold $F^\pm$ is given by:

$$\begin{aligned}
\varepsilon\frac{dv}{dt} &= \bar{I} - (\hat{M}(v,n,h,\varepsilon))^3h(v-\bar{E}_{Na}) - \bar{g}_kn^4(v-\bar{E}_k) - \bar{g}_l(v-\bar{E}_L),\\
\frac{dh}{dt} &= \frac{1}{\tau_h t_h(v)}(h_\infty(v)-h),\\
\frac{dn}{dt} &= \frac{1}{\tau_n t_n(v)}(n_\infty(v)-n).
\end{aligned} \tag{5.6}$$

One of the classical reduction steps in the literature is to use the quasi-steady state approximation $m=m_\infty(v)$ rather than perform the full centre manifold reduction $m=\hat{M}(v,n,h,\varepsilon)$. We have to expect quantitative changes in the reduced model (i.e., in equations (5.6) with $\hat{M}(v,n,h,\varepsilon)$ replaced by $m_\infty(v)$) compared to the full HH model (5.5), and such changes are in fact observed. For example, equations (5.5) have a subcritical Hopf bifurcation for $I=9.8\ \mu A/cm^2$ (i.e., $\bar{I}=0.00082$) while equations (5.6) with $\hat{M}=m_\infty$ have a subcritical Hopf bifurcation for $I=7.8\ \mu A/cm^2$ (i.e., $\bar{I}=0.00065$). We note that the Hopf bifurcation of equations (5.5) is in the vicinity of the fold curve for sufficiently small ε, because in the singular limit the Hopf bifurcation is a singular Hopf bifurcation (Rubin and Wechselberger, 2007, 2008). Thus the Hopf bifurcation in equations (5.5) is in the neighbourhood of the fold where Proposition 1 applies. Further discussion of this type of Hopf bifurcation is contained in Section 5.3.4.

5.3 Hopf bifurcation in slow-fast systems

In the previous section, it was shown that the quasi-steady state reduction technique is mathematically justified in a slow-fast system if the critical manifold is normally hyperbolic or if we are interested in the dynamics near a fold of the critical manifold. In this section we show that the quasi-steady state reduction technique, when applied to slow-fast systems with a Hopf bifurcation, may lead to changes in the criticality of the Hopf bifurcation. From a dynamical systems point of view, it is well established that misleading results may be obtained if a proper centre manifold reduction is not performed prior to the calculation of criticality of a Hopf bifurcation (Guckenheimer and Holmes, 1983; Kuznetsov, 1998). However, in the context of biophysical systems, model variables often have a physiological meaning. Therefore, it is tempting to try to avoid making coordinate transformations that transform the variables into physically ambiguous combinations. (Transformations required for centre manifold reductions are frequently of this type.) Unfortunately, without the proper centre manifold reduction the criticality of a Hopf bifurcation in a model may not match the criticality of the corresponding Hopf bifurcation in the model obtained after applying the reduction technique and this has resulted in some erroneous conclusions in the literature about the criticality of Hopf bifurcations in some biophysical models, as we will show in this section.

We then go on to show that there can be problems with the use of geometric singular perturbation theory in analyzing slow-fast models with Hopf bifurcations. In particular we show that the criticality of a Hopf bifurcation in a full system may not match the criticality of the corresponding Hopf bifurcation in the associated fast subsystem. This last result is independent of whether a quasi-steady state assumption or other reduction technique has been used prior to applying geometric singular perturbation theory. We illustrate our results with numerical examples throughout the section.

5.3.1 Computing the criticality of a Hopf bifurcation

We first give a brief review of the general procedure for computing the criticality of a Hopf bifurcation. The criticality of a Hopf bifurcation is determined by the sign of the first Lyapunov coefficient of a system near a Hopf bifurcation (Kuznetsov, 1998; Guckenheimer and Holmes, 1983). Specifically, consider a general system

$$\frac{dx}{dt} = f(x;\mu)\,,$$

with $x \in \mathbb{R}^n$, $\mu \in \mathbb{R}$ and with a Hopf bifurcation at $x = 0$, $\mu = \hat{\mu}$. Write the Taylor expansion of $f(x; \hat{\mu})$ at $x = 0$ as

$$f(x; \hat{\mu}) = Ax + \frac{1}{2}B(x, x) + \frac{1}{6}C(x, x, x) + O(\|x\|^4),$$

where A is the Jacobian matrix evaluated at the bifurcation, and $B(x, y)$ and $C(x, y, z)$ are multilinear functions with components

$$B_j(x, y) = \sum_{k,l=1}^{n} \left.\frac{\partial^2 f_j(\xi; \hat{\mu})}{\partial \xi_k \partial \xi_l}\right|_{\xi=0} x_k y_l, \tag{5.7}$$

$$C_j(x, y, z) = \sum_{k,l,m=1}^{n} \left.\frac{\partial^3 f_j(\xi; \hat{\mu})}{\partial \xi_k \partial \xi_l \partial \xi_m}\right|_{\xi=0} x_k y_l z_m, \tag{5.8}$$

where $j = 1, 2, \ldots, n$. Let $q \in \mathbb{C}^n$ be a complex eigenvector of A corresponding to the eigenvalue $i\omega$, i.e., $Aq = i\omega q$. Let p be the associated adjoint eigenvector, i.e., $p \in \mathbb{C}^n$ and $A^T p = -i\omega p$, $\langle p, q\rangle = 1$. Here $\langle p, q\rangle = \bar{p}^T q$ is the usual inner product in $\mathbb{C}^n$. Then the first Lyapunov coefficient for the system is defined as

$$\begin{aligned} l_1 \;&= \tfrac{1}{2\omega}\mathrm{Re}\;\; [\langle p, C(q, q, \bar{q})\rangle - 2\langle p, B(q, A^{-1}B(q, \bar{q}))\rangle \\ &\qquad\qquad + \langle p, B(\bar{q}, (2i\omega I_n - A)^{-1}B(q, q))\rangle], \end{aligned} \tag{5.9}$$

where I_n is the $n \times n$ identity matrix. If $l_1 < 0$ the Hopf bifurcation is supercritical and produces periodic solutions that are stable on the three-dimensional extended centre manifold corresponding to the Hopf bifurcation. If $l_1 > 0$, the Hopf bifurcation is subcritical and the associated periodic orbits are unstable within the three-dimensional extended centre manifold.

5.3.2 Hopf bifurcation and model reduction

Here we are concerned with physiological models that are of the same form as (5.1) except that v is now in $\mathbb{R}^2$ instead of in $\mathbb{R}$. In particular, we are interested in models that are described in dimensionless form by singularly perturbed systems with the form

$$\begin{aligned} \frac{dv}{dt} &= f(v, m, n, \mu, \varepsilon), \\ \frac{dm}{dt} &= h(v, m, n, \mu, \varepsilon), \\ \frac{dn}{dt} &= \varepsilon g(v, m, n, \mu, \varepsilon), \end{aligned} \tag{5.10}$$

where $(v, m) \in \mathbb{R}^2 \times \mathbb{R}^j = \mathbb{R}^k$ are the fast variables, $n \in \mathbb{R}^l$ are the slow variables, f, g and h are $O(1)$ vector-valued functions, $\mu \in \mathbb{R}^m$ are system parameters and $\varepsilon \ll 1$ is the singular perturbation parameter reflecting the time scale separation. Without loss of generality, we fix $m-1$ parameters, and consider Hopf bifurcations that occur as the other parameter, which we denote by ν, is varied.

Assumption 3 *System* (5.10) *possesses a non-degenerate Hopf bifurcation at $\nu = \hat{\nu}_\varepsilon$. Specifically, for sufficiently small ε:*

(a) there exists a family of equilibria $(v(\nu,\varepsilon), m(\nu,\varepsilon), n(\nu,\varepsilon))$, for ν in a neighbourhood of $\hat{\nu}_\varepsilon$, such that the Jacobian matrix has a pair of eigenvalues, $\lambda_1(\nu)$ and $\lambda_2(\nu)$, with $\lambda_1(\hat{\nu}_\varepsilon) = \bar{\lambda}_2(\hat{\nu}_\varepsilon) = i\omega$ where $\omega = O(1)$, while the other $(k-2)$ eigenvalues associated with the fast components of the vector field all have real parts of order $O(1)$, which we assume to be negative;

(b) $\frac{d}{d\nu} Re\ (\lambda_1)|_{\nu=\hat{\nu}_\varepsilon} = O(1) \neq 0$;

(c) $l_1(\varepsilon) = O(1) \neq 0$, where l_1 is the first Lyapunov coefficient associated with the Hopf bifurcation;

(d) the bifurcation parameter ν persists in the singular limit $\varepsilon \to 0$, i.e., ν appears explicitly in the fast subsystem.

The condition $\omega = O(1)$ ensures that the Hopf bifurcation is in the fast variables. Thus there is a Hopf bifurcation for $\nu = \hat{\nu}_0$ in the singular limit system of (5.10), the fast subsystem. We assume, without loss of generality, that the complex eigenvector $q \in \mathbb{C}^k$ of the eigenvalue $i\omega$ in the fast subsystem of (5.10) has nonzero entries in the first two fast components of the vector field, $v \in \mathbb{R}^2$, i.e., we associate the Hopf bifurcation with the direction of v.

A natural first step in determining the criticality of the Hopf bifurcation in the full system (5.10) might be to reduce the dimension of the model by setting the fast gating variables $m \in \mathbb{R}^j$ to their quasi-steady state as described in section 5.2. Since $D_m h$ is invertible we can invoke the implicit function theorem and solve $h = 0$ for $m = M(v, n, \mu, \varepsilon)$. Again, we can introduce a coordinate change $\hat{m} = m - M(v, n, \mu, \varepsilon)$. However, this process does not always correspond to a proper centre manifold reduction as in the case of a folded critical manifold. In general, one also has to introduce new coordinates $\hat{v} \in \mathbb{R}^2$ to align the centre manifold with $\hat{m} = 0$. Hence, a reduction of the fast gating variables m alone typically changes the first Lyapunov coefficient which might change the criticality of the Hopf bifurcation, so that the Hopf bifurcation in the full system is subcritical while the Hopf bifurcation in the lower-dimensional system is supercritical (or vice versa). This effect is independent of whether the Hopf bifurcation involves fast or slow variables.

The Chay-Keizer model

An example in which we get such a change of criticality of Hopf bifurcation is the Chay-Keizer model of a pancreatic β-cell (Chay and Keizer, 1983). This minimal biophysical model was originally developed as a system of five ordinary differential equations to describe the bursting behaviour of a β-cell :

$$\begin{aligned}
C_m \frac{dV}{dt} &= -I_{\mathrm{Ca}}(V) - (\bar{g}_K n^4 + \frac{\bar{g}_{\mathrm{K,Ca}} c}{K_d + c})(V - V_K) - \bar{g}_L (V - V_L) + I_{app}, \\
\frac{dn}{dt} &= a_n(V + V^*)(1 - n) - b_n(V + V^*)n, \\
\frac{dm}{dt} &= a_m(V + V')(1 - m) - b_m(V + V')m, \\
\frac{dh}{dt} &= a_h(V + V')(1 - h) - b_h(V + V')h, \\
\frac{dc}{dt} &= f(-k_1 I_{\mathrm{Ca}}(V) - k_c c),
\end{aligned} \tag{5.11}$$

where V represents the membrane potential of a β cell, n the activation gate of a potassium channel, m and h the activation and inactivation gates of a calcium channel, and c the cytoplasmic concentration of free calcium. The quantity $I_{\mathrm{Ca}}(V) = \bar{g}_{\mathrm{Ca}} m^3 h (V - V_{\mathrm{Ca}})$ is the calcium current and I_{app} is an applied external current and is also the bifurcation parameter. The other parameter values and the functions a_n, b_n, etc. are specified in Appendix A. A straightforward numerical bifurcation analysis of system (5.11) using AUTO shows that there are two Hopf bifurcations, with a subcritical Hopf bifurcation at $I_{app} \approx 0.4419$, as shown in Fig. 5.1.

On the other hand, in Rinzel and Lee (1986), the authors simplify the five-dimensional Chay-Keizer model by setting the gating variables m and h equal to their quasi-steady state values, i.e., they choose

$$\begin{aligned}
m &= \frac{a_m(V + V')}{a_m(V + V') + b_m(V + V')} := m_\infty(V), \\
h &= \frac{a_h(V + V')}{a_h(V + V') + b_h(V + V')} := h_\infty(V).
\end{aligned}$$

The reduction is based on the observation that these gates m and h have fast kinetics. Numerical bifurcation analysis of the corresponding three-dimensional system that results from this process reveals that this reduced model has a supercritical Hopf bifurcation at a nearby parameter value at $I_{app} \approx 0.4429$. Thus, the reduction of the dimension of this system by equating these gating variables to their equilibrium values changes the criticality of the Hopf bifurcation; if an aim of analysis is to determine the criticality of Hopf bifurcations, then this type of reduction should not be attempted.

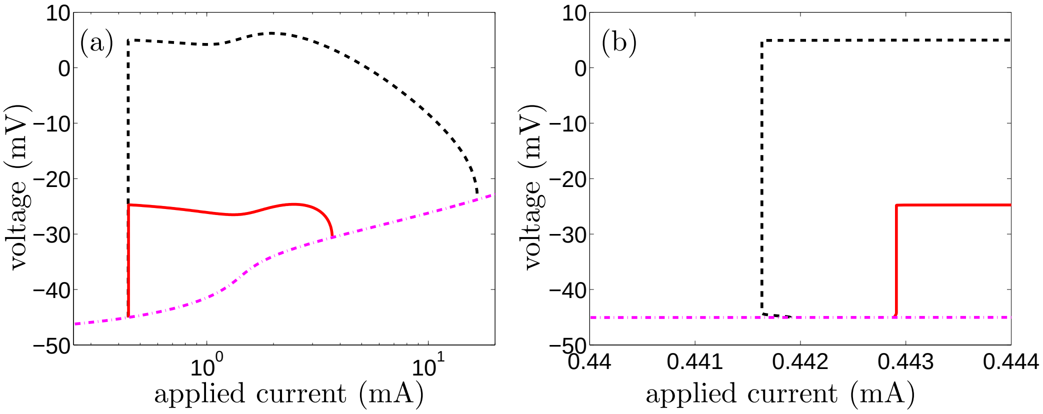

Figure 5.1: Bifurcation diagrams for two versions of the Chay-Keizer model: the full five-dimensional model, equations (5.11) and the reduced three-dimensional model obtained by setting m and h equal to their quasi-steady state values. The position of the equilibrium solutions is the same in both models and is indicated by the pink dot-dash curve. The black dashed curve shows the maximum voltage attained on a branch of periodic solutions in the full model, while the red solid curve shows the maximum voltage attained on the corresponding branch of periodic orbits in the reduced model. Panel (b) shows an enlargement of part of Panel (a), near the left pair of Hopf bifurcations.

We note that the widely used three-dimensional model captures the most important dynamical feature of pancreatic β-cells, namely their bursting behaviour.

Fig. 5.1 also shows that both versions of the model have a second Hopf bifurcation at much higher applied current. In both cases this is a supercritical bifurcation but the value of the parameter at the bifurcation differs significantly between the models. Thus, the model reduction used also has the effect of making a significant change to the amplitude of the oscillations and the range of values of the applied current for which the oscillations occur.

5.3.3 Hopf bifurcation in the full slow-fast system versus the fast subsystem

A second potential trap in determining the criticality of a Hopf bifurcation in system (5.10) comes when we try to apply geometric singular perturbation theory. From Assumption 3 it follows that a Hopf bifurcation in the full system will persist in the singular limit as a Hopf bifurcation in the fast subsystem. It might be tempting to proceed by determining the criticality of the Hopf bifurcation in the fast subsystem and then asserting that the Hopf bifurcation in the slow-fast system will be of the same type. However, the existence of a Hopf bifurcation satisfying Assumption 3 automatically implies that the critical manifold of the full system is not normally hyperbolic near the bifurcation, and, hence, that Fenichel theory (Fenichel, 1979) is not applicable. In this case, there is no guarantee that complete information about bifurcations in the full system can be obtained from analysis of the fast subsystem alone.

Let us revisit the Chay-Keizer model (5.11). If we assume that c is a slow variable and (v, m, h, n) are fast variables, as is usually done in the literature, then the fast subsystem is four-dimensional. Numerical bifurcation analysis of the fast subsystem shows that it has a supercritical Hopf bifurcation at $I_{app} \approx 0.4427$. Again, the criticality of the Hopf bifurcation has changed: the criticality of the Hopf bifurcation in the fast subsystem is not the same as the criticality of the corresponding Hopf bifurcation in the full system. At first glance, this result seems counterintuitive since one does not expect that the small $(O(\varepsilon))$ terms of the slow c equation in (5.11) play an important role in the calculation of the first Lyapunov coefficient.

In the following, we show how these small $O(\varepsilon)$ terms can be significant in determining the criticality of a Hopf bifurcation in a slow-fast system. In particular, we show that calculating the first Lyapunov coefficient $l_1(\varepsilon)$ of a Hopf bifurcation in the full system and then taking the limit $\varepsilon \to 0$ does not give the Lyapunov coefficient $\hat{l}_1$ of the Hopf bifurcation in the corresponding fast subsystem, i.e., in general,

$$\lim_{\varepsilon \to 0} l_1(\varepsilon) \neq \hat{l}_1 \,. \tag{5.12}$$

First Lyapunov coefficient for a three-dimensional problem

Consider the singular perturbed system of equations

$$\begin{aligned} \frac{dx}{dt} &= f_1(x, y, z; \mu, \varepsilon), \\ \frac{dy}{dt} &= f_2(x, y, z; \mu, \varepsilon), \\ \frac{dz}{dt} &= \varepsilon g(x, y, z; \mu, \varepsilon), \end{aligned} \tag{5.13}$$

where $x, y, z \in \mathbb{R}$, $\mu \in \mathbb{R}$ is the bifurcation parameter, ε is a small parameter, and f_1, f_2 and g are $O(1)$ smooth functions. Then x and y are fast variables and z is a slow variable. Suppose that Assumption 3 is fulfilled for system (5.13) – thus system (5.13) and the corresponding fast subsystem both have Hopf bifurcations. Furthermore, we assume that $(0, 0, 0; \hat{\mu}_0, 0)$ is the Hopf point of the fast subsystem. Note that the position of the Hopf point in phase and parameter space can vary with ε, by $O(\varepsilon)$, and so the Hopf bifurcation value $\mu = \hat{\mu}_\varepsilon$ of the full system is, in general, different to the bifurcation value $\mu = \hat{\mu}_0$ of the fast subsystem. More importantly, we show that the $O(\varepsilon)$ terms in the slow equation can produce an $O(1)$ change in the first Lyapunov coefficient which in turn may lead to a change of the criticality of the Hopf bifurcation in the full system compared with the criticality of the associated Hopf bifurcation in the fast subsystem. This means that analysis of the fast subsystem alone is not sufficient to determine the dynamics associated with the Hopf bifurcation.

Since the Hopf point of the fast subsystem is $(0,0,0;\hat{\mu}_0,0)$, it is straightforward to use the formulae in section 5.3.1 to compute the first Lyapunov coefficient (5.9) for the Hopf bifurcation in the fast subsystem for (5.13), i.e., for the system

$$\begin{aligned} \frac{dx}{dt} &= f_1(x,y,z;\mu,0), \qquad (5.14)\\ \frac{dy}{dt} &= f_2(x,y,z;\mu,0). \end{aligned}$$

It is convenient for what follows to introduce some notation. The Jacobian matrix, A_a, at the Hopf point, and its inverse A_a^{-1} are

$$A_a = \begin{pmatrix} a_{11} & a_{12} \\ a_{21} & a_{22} \end{pmatrix}, \qquad A_a^{-1} = \frac{1}{\omega_a^2}\begin{pmatrix} a_{22} & -a_{12} \\ -a_{21} & a_{11} \end{pmatrix},$$

with $a_{11}+a_{22}=0$ and $a_{11}a_{22}-a_{21}a_{12} \equiv \omega_a^2 > 0$. Let $q_a = (q_1,q_2)$ be a (right) eigenvector of A_a corresponding to the eigenvalue $i\omega_a$ and let $p_a = (p_1,p_2)$ be the corresponding adjoint (or left) eigenvector. Then, defining B_a and C_a as in section 5.3.1 (with the subscript merely denoting that they are the B and C multi-linear forms corresponding to the same system as A_a), the first Lyapunov coefficient (5.9) is

$$\begin{aligned} \hat{l}_{1a} = \quad & \frac{1}{2\omega_a}\mathrm{Re}\left[\langle p_a, C_a(q_a,q_a,\bar{q_a})\rangle - 2\langle p_a, B_a(q_a, A_a^{-1}B_a(q_a,\bar{q_a}))\rangle\right. \\ & \left. + \langle p_a, B_a(\bar{q_a}, (2i\omega_a I_2 - A_a)^{-1}B_a(q_a,q_a))\rangle\right]. \end{aligned}$$

We now return to the full system (5.13). The Jacobian matrix at the Hopf point will have the form

$$A_c = \begin{pmatrix} a_{11}+O(\varepsilon) & a_{12}+O(\varepsilon) & a_{13} \\ a_{21}+O(\varepsilon) & a_{22}+O(\varepsilon) & a_{23} \\ \varepsilon a_{31} & \varepsilon a_{32} & \varepsilon a_{33} \end{pmatrix},$$

where the matrix has a purely imaginary eigenvalue $i\omega_c$ with $\omega_c^2 = \omega_a^2 + O(\varepsilon)$. The inverse matrix A_c^{-1} is given by

$$A_c^{-1} = \frac{O(1)}{\omega_c^2}\begin{pmatrix} a_{22}+O(1) & -a_{12}+O(1) & O(\varepsilon^{-1}) \\ -a_{21}+O(1) & a_{11}+O(1) & O(\varepsilon^{-1}) \\ (a_{31}+k_1a_{32})O(1) & (a_{32}+k_2a_{31})O(1) & O(\varepsilon^{-1}) \end{pmatrix},$$

where k_1 and k_2 are $O(1)$ coefficients. We note that the position of the Hopf bifurcation point can vary with ε and thus the entries in the corresponding (2×2)-submatrix of the Jacobian A_c may differ (by at most $O(\varepsilon)$) from their values in the Jacobian A_a of the fast subsystem.

A (right) eigenvector of A_c corresponding to the eigenvalue $i\omega_c$ is given by $q_c = (q_1 + O(\varepsilon), q_2 + O(\varepsilon), O(\varepsilon))$ with adjoint (or left) eigenvector $p_c = (p_1 + O(\varepsilon), p_2 + O(\varepsilon), p_3 + O(\varepsilon))$. Note that $p_3 = O(1)$, since it satisfies $a_{13}p_1 + a_{23}p_2 + i\omega_c p_3 = 0$ to leading order.

Our aim is to calculate the difference of the first Lyapunov coefficients for the full and fast subsystems, i.e., $l_{1c}(\varepsilon) - \hat{l}_{1a}$. We have $C_c(q_c, q_c, \bar{q}_c) = (O(1), O(1), O(\varepsilon))$ which gives

$$\langle p_a, C_a(q_a, q_a, \bar{q}_a)\rangle - \langle p_c, C_c(q_c, q_c, \bar{q}_c)\rangle = O(\varepsilon)\,. \tag{5.15}$$

We also have $B_c(q_c, \bar{q}_c) = (O(1), O(1), O(\varepsilon))$ and $A_c^{-1}B_c(q_c, \bar{q}_c) = (O(1), O(1), O(1))$ from which follows that

$$\langle p_a, B_a(q_a, A_a^{-1}B_a(q_a, \bar{q}_a))\rangle - \langle p_c, B_c(q_c, A_c^{-1}B_c(q_c, \bar{q}_c))\rangle = O(1)\,. \tag{5.16}$$

Similarly, we obtain that

$$\begin{aligned} &\langle p_a, B_a(\bar{q}_a, (2i\omega_a I_2 - A_a)^{-1}B_a(q_a, q_a))\rangle \\ &-\langle p_c, B_c(\bar{q}_c, (2i\omega_c I_3 - A_c)^{-1}B_c(q_c, q_c))\rangle \;=\; O(1). \end{aligned} \tag{5.17}$$

Combining all these results, we find that

$$l_{1c}(\varepsilon) - \hat{l}_{1a} = O(1)\,. \tag{5.18}$$

Thus, l_{1c} may not tend to $\hat{l}_{1a}$ as $\varepsilon \to 0$. In other words, an $O(\varepsilon)$ perturbation to equations (5.13) can yield an $O(1)$ difference in the first Lyapunov coefficient, which may induce a sign change.

It is worth having a closer look to see what causes this $O(1)$ difference in (5.18). Note that (5.15) only contributes an $O(\varepsilon)$ perturbation to the Lyapunov coefficient. Thus third order terms in (x, y, z) of the function g have no influence on the result. On the other hand, linear and second order terms in (x, y, z) of the function g are responsible for the $O(1)$ difference in (5.16) and (5.17). To be more precise, the quantities $\frac{\partial g}{\partial x} = a_{31}$, $\frac{\partial g}{\partial y} = a_{32}$, $\frac{\partial^2 g}{\partial x^2}$, $\frac{\partial^2 g}{\partial x \partial y}$ and $\frac{\partial^2 g}{\partial y^2}$ evaluated at the Hopf bifurcation are responsible for this discrepancy. So, if these five terms do not exist, or vanish at the Hopf bifurcation, then the terms (5.16) and (5.17) are of $O(\varepsilon)$ and the Lyapunov coefficient $l_{1c}(\varepsilon)$ is an $O(\varepsilon)$ perturbation of $\hat{l}_{1a}$.

These results have significant consequences for computation of the criticality of the

α	k_s	k_f	k_p	φ_1	φ_2	τ	γ
0.05 s^{-1}	20.0 s^{-1}	20.0 s^{-1}	20.0 s^{-1}	2.0 μM	1.0 μM	2.0 s^{-1}	5.0

Table 5.1: Parameters of the simplified Atri model, equations (5.19).

Hopf bifurcation for (5.13). Specifically, the $O(1)$ difference found above may result in a sign change of the first Lyapunov coefficient, so that the Hopf bifurcation in the fast subsystem may be supercritical while the Hopf bifurcation in the full system is subcritical (or vice versa). Thus, we see that, in general, it is not possible to predict the criticality of a Hopf bifurcation in a slow-fast system with two or more fast variables in the limit $\varepsilon \to 0$ simply by observing the criticality of the associated Hopf bifurcation in the fast subsystem. However, in the special case that the component of the vector field associated with the slow variable is sufficiently aligned with the centre manifold of the full system (5.13) then there is no such difficulty; the criticality of the Hopf bifurcations in the $\varepsilon = 0$ limit of the full system and in the fast subsystem will be the same.

Application to a model of intracellular calcium dynamics

To see how these results apply to a specific model with two fast and one slow variables, we consider a simplified version of a model of calcium oscillations (Atri et al., 1993). The formulation of this model is quite similar to equations (3.2) considered in chapter 3, except that we also include a dynamical variable n to describe the variation of the fraction of IP$_3$ receptors that have not been inactivated by calcium and omit the consideration of the calcium diffusion term by setting the diffusion coefficient $D = 0$. Specifically, the calcium equations studied here have the following form:

$$\begin{aligned}
\frac{dc}{dt} &= \left(\alpha + k_f \frac{c^2}{c^2+\varphi_1^2} n\right)(c_t - (\gamma+1)c) - k_s c + \varepsilon(J_{in} - k_p c), \\
\frac{dn}{dt} &= \frac{1}{\tau}\left(\frac{\varphi_2}{\varphi_2 + c} - n\right), \\
\frac{dc_t}{dt} &= \varepsilon(J_{in} - k_p c),
\end{aligned} \tag{5.19}$$

where values of all the system parameters are given in Table 5.1. In this model, c represents the concentration of free calcium in the cytoplasm, c_t is the total number of moles of calcium in the cell, divided by the cytoplasmic volume, and n is the proportion of IP$_3$ receptors that have not been inactivated by calcium.

The original Atri model is known to be a multiple time scale system, and some results about the original version of the model have been established with the help of

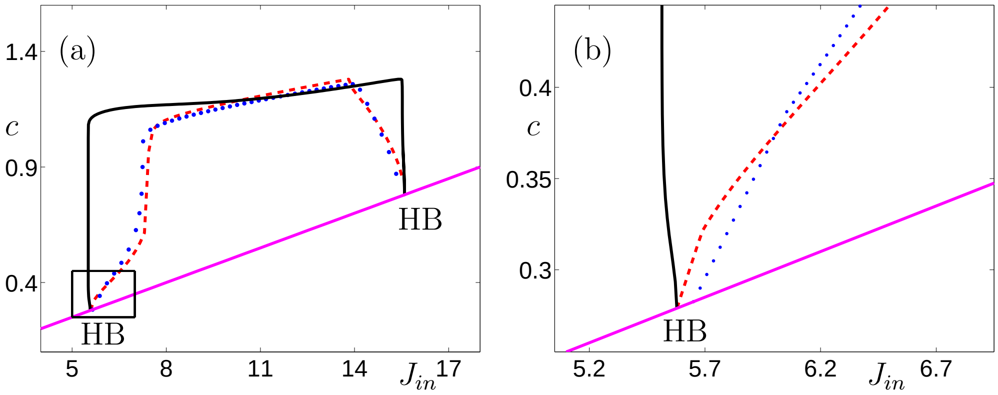

Figure 5.2: Partial bifurcation diagram for the simplified Atri model, equations (5.19) with various values of ε and other parameter values as in Table 5.1. The pink solid curve shows the position of the unique equilibrium of the model. This equilibrium has two Hopf bifurcations (labelled HB), with the equilibrium being of saddle-type for parameter values between the two Hopf bifurcations and being stable otherwise. The remaining curves show the maximum c-values attained by the periodic orbits created in the Hopf bifurcations, for three choices of ε, i.e., $\varepsilon = 10^{-4}$, $\varepsilon = 10^{-2}$ and $\varepsilon = 0$ (fast subsystem) on the red thick dashed, blue dotted and black thin solid curves, respectively. Panel (b) shows an enlargement of the marked rectangle in panel (a). Note that the left-most Hopf bifurcation in panel (a) is subcritical when $\varepsilon = 0$ but supercritical for all $\varepsilon > 0$.

geometric singular perturbation theory to explain the dynamics observed in the model (Domijan et al., 2006; Harvey et al., 2010, 2011). Our simplified version of the Atri model is also a multiple time scale system. Specifically, for the values of the parameters specified in Table 5.1, the right hand sides of the $\frac{dc}{dt}$, $\frac{dn}{dt}$ and $\frac{dc_t}{dt}$ equations, respectively, are $O(1)$, $O(1)$ and $O(\varepsilon)$, respectively, and so the model has two fast variables and one slow variable when $\varepsilon \ll 1$.

Part of the bifurcation diagram for this model is shown in Fig. 5.2, for three different choices of ε. The model has a unique equilibrium when $\varepsilon \neq 0$, the position of which does not depend on ε. This equilibrium has two Hopf bifurcations at parameter values that depend on ε; we are interested in the criticality of the left-most Hopf bifurcation for $J_{\text{in}} \approx 5$.

As can be seen in Fig. 5.2, the left-most Hopf bifurcation for this model is subcritical in the fast subsystem but supercritical for the full problem for the two non-zero choices of ε shown. As shown in Fig. 5.3, the left-most Hopf bifurcation is in fact supercritical ($l_1 < 0$) for all choices of small $\varepsilon > 0$ and subcritical ($l_1 > 0$) at $\varepsilon = 0$. Inspection of equations (5.19) shows that the differential equation for the slow variable c_t contains a term that is linear in c, one of the fast variables, and this feature is not changed by the transformation required to shift the branch of equilibria to the origin (which is linear for the c component). As discussed at the end of section 5.3.3, we can thus expect an $O(1)$ difference between the first Lyapunov coefficients for the Hopf bifurcations in

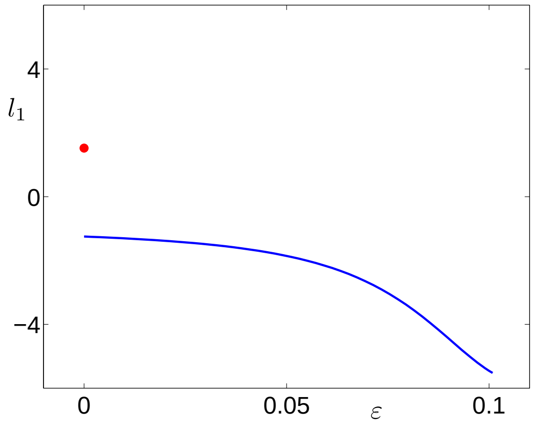

Figure 5.3: The first Lyapunov coefficient of the left-most Hopf bifurcation plotted as a function of ε for equations (5.19) with parameter values as in Table. 5.1. The blue solid curve shows the first Lyapunov coefficient for $0 < \varepsilon < 0.1$, and the red large dot marks the first Lyapunov coefficient for $\varepsilon = 0$.

the fast subsystem and the full system in the model. Therefore, there is no reason to expect the criticality of the Hopf bifurcations to be the same for the full system and the fast subsystem. The Chay-Keizer model discussed above provides another example of a specific model with the same difficulty.

5.3.4 Hopf bifurcation involving both fast and slow variables

In a range of biophysical systems, including Hodgkin-Huxley type neuronal models such as system (5.5) and a variety of calcium models such as those discussed in Harvey et al. (2010), Hopf bifurcations in the full system are found in the neighbourhood of a fold of the critical manifold S_0, as defined in Assumption 2. In such cases, neither the fast nor slow subsystem has a Hopf bifurcation; instead the Hopf bifurcation involves both fast and slow variables. This implies that the complex conjugate eigenvalues associated with the Hopf bifurcation are λ_1 and λ_2 with $\lambda_1(\hat{\mu}, \varepsilon) = \bar{\lambda}_2(\hat{\mu}, \varepsilon) = i\omega$, where $\omega = O(\sqrt{\varepsilon})$ and so the Hopf bifurcation vanishes in the singular limit. This special type of Hopf bifurcation is known as a singular Hopf bifurcation (Baer and Erneux, 1986; Braaksma, 1998; Guckenheimer, 2008) and it is closely related to the notion of canard explosion and type II folded saddle-node singularities in geometric singular perturbation theory; we refer the reader to the literature on this subject (Krupa et al., 1997; Rubin and Wechselberger, 2007). Since the singular Hopf bifurcation vanishes in the singular limit, it is mandatory to calculate the criticality of the Hopf bifurcation for $\varepsilon \neq 0$ and we do not run into the same problem as in the previous case study. We are not tempted to use the first Lyapunov coefficient from the singular limit to predict the value of l_1 in the full system, since it is zero in the singular limit and clearly non-zero in the full system.

5.3.5 Hopf bifurcation in the slow subsystem

This case of Hopf bifurcation occurring in the slow subsystem is trouble free for a singularly perturbed system under Assumption 1 that the critical manifold S_0 is normally hyperbolic. In this case, Fenichel theory (Fenichel, 1979) applies and the slow flow on the slow manifold S_ε is a regular perturbation of the slow subsystem, a remarkable insight from Fenichel's work. It implies that if we have a Hopf bifurcation in the slow subsystem then it persists generically as a Hopf bifurcation in the full problem. Furthermore, the first Lyapunov coefficient $l_1(\varepsilon)$ is a regular perturbation of the singular limit value $l_1(0)$, i.e,

$$\lim_{\varepsilon \to 0} l_1(\varepsilon) = l_1(0)\,. \tag{5.20}$$

Thus, criticality of the Hopf bifurcation in the full system is then the same as criticality of the Hopf bifurcation in the reduced problem, the slow subsystem.

On the other hand, if the Assumption 1 is not satisfied, the critical manifold loses normal hyperbolicity at the Hopf bifurcation then we are dealing with a more degenerate bifurcation: a "fold-Hopf"-type bifurcation in the case where the critical manifold is folded and a "Hopf-Hopf"-type bifurcation in the case of a simultaneous Hopf bifurcation in the fast subsystem. These cases are outside of the scope of this thesis and we do not consider them further.

5.4 Summary

In this chapter, we have discussed some difficulties that may arise when computing the criticality of Hopf bifurcations in slow-fast systems. We have identified two potential problems. The first problem may occur in neural type models that have fast gating variables. In biophysical systems of this type, a typical first step in the model analysis is to reduce the dimension of the model by making a quasi-steady state assumption and replacing the differential equations for one or more of the fast gating variables by the steady state values. This technique is widely used in the analysis of biophysical models, and is believed to preserve many important qualitative features of the dynamics. However, we have shown that this reduction technique can change the criticality of Hopf bifurcations in the system, which means that a subcritical Hopf bifurcation in the full system becomes a supercritical Hopf bifurcation in the reduced system, or vice versa. If the purpose of analysis is to determine the nature of the onset of oscillations, it may not be advisable to perform a quasi-steady state reduction.

We note that a change in the criticality of the Hopf bifurcation alone may not make a significant change to the overall observed dynamics. For instance, in the Chay-Keizer model (5.11) discussed in section 5.3.2, the branch of periodic solutions near the Hopf bifurcation is very steep, in both the full system and the reduced system obtained by applying a quasi-steady state assumption (see Fig. 5.1). This means that the onset of oscillations occurs at almost the same parameter value in both the full system and the reduced system, despite the criticalities of the Hopf bifurcations being different. However, we also remark that the maximum amplitude of the oscillations is very different in the two models, as is the overall parameter range for which oscillations exist. Despite all these difference, the reduced model still captures the interesting physiological feature, the potential bursting behaviour, of pancreatic β-cells. Therefore, the widely used reduced model is quite helpful to analyze and understand potential bursting dynamics of β-cells.

The second potential problem we discussed may arise if we attempt to use geometric singular perturbation theory in the analysis of a model with a Hopf bifurcation. Geometric singular perturbation theory aims to use lower dimensional fast and slow subsystems to make predictions about the dynamics in the full system. We have shown that when a Hopf bifurcation in a full slow-fast system has a corresponding Hopf bifurcation in the fast subsystem, (i.e., the equilibrium has eigenvalues $\lambda = \pm i\omega$ with $\omega = O(1)$) the criticality can be different between the full system and the fast subsystem. This means that the fast subsystem cannot be used to make predictions about the criticality of the Hopf bifurcation in the full system. In some biophysical models, the fast subsystem corresponds to a physically relevant state of the system. For example, in models of intracellular calcium dynamics, the fast subsystem often can be thought of a modeling the cell with no flux across the cell membrane. In such a situation, it is tempting to presume that the dynamics of the fast subsystem will match the dynamics of the full model in the limit that we approach the fast subsystem. We have shown that this is not the case, at least for the criticality of Hopf bifurcations.

There are no such difficulties in computing the criticality of Hopf bifurcations that involve slow variables. We discussed two cases. The first case occurs when the Hopf bifurcation in the full model is caused by the interaction of a slow and a fast variable. The Hopf bifurcation is a singular Hopf, i.e., the relevant eigenvalues for the Hopf bifurcation are $\lambda = \pm i\omega$ with $\omega = O(\sqrt{\varepsilon})$. In this case, the Hopf bifurcation vanishes in the singular limit, and one is not tempted to deduce the criticality of the Hopf bifurcation in the full problem from the dynamics of the fast subsystem or the reduced problem. Alternatively, if the critical manifold is normally hyperbolic and there is a Hopf bifurcation in the slow subsystem (i.e. $\lambda = \pm i\omega$ with $\omega = O(\varepsilon)$), the criticality of the Hopf bifurcation will be the same in the full system and the slow subsystem.

In recent work, Guckenheimer and Osinga (Guckenheimer and Osinga, 2012) investigate two slow-fast systems in which the criticality of a Hopf bifurcation in the full system does not match the criticality of the corresponding Hopf bifurcation in the fast subsystem. They show that in each case there is a nearby torus bifurcation in the slow-fast system and that the family of periodic orbits in the full system is $O(\varepsilon)$ close to the family of periodic orbits in the layer problem, regardless of the criticality of the Hopf bifurcation. A practical consequence of their work is that observation of a torus bifurcation close to a Hopf bifurcation in a slow-fast system is a possible indication that the full system and the corresponding fast subsystem will have Hopf bifurcations of different criticalities, so extra care should be taken in the analysis of the model with this kind of bifurcation diagram.

A wide variety of biophysical models are of the types that are potentially affected by the problems we have discussed in this chapter, including Hodgkin-Huxley type neural models and many models of intracellular calcium dynamics. One specific example of different criticalities of Hopf bifurcations in the full system and in the corresponding fast subsystem of a calcium model was shown in chapter 3. In light of our results, it seems advisable that care be taken when attempting to use either quasi-steady state reductions or geometric singular perturbation theory for the analysis of slow-fast systems with Hopf bifurcations.

Chapter 6

Using Lin's method to compute and continue global bifurcations

Global objects, such as stable and unstable manifolds, play a very important part in determining the dynamics of a system (Kuznetsov, 1998; Guckenheimer and Holmes, 1983). Global bifurcations involving saddle periodic orbits recently have been recognized as being involved in various new types of organizing centres for complicated dynamics (Krauskopf and Riess, 2008; Doedel et al., 2008, 2009). The main emphasis in these papers has been on heteroclinic connections between saddle equilibria and saddle periodic orbits, called EtoP orbits for short, which can be found in vector fields in $\mathbb{R}^3$. Thanks to the development of dedicated numerical techniques, EtoP orbits have been found in a number of three-dimensional model vector fields arising in applications (Aguirre et al., 2011; Krauskopf and Riess, 2008; Doedel et al., 2008, 2009). In chapter 2, we mentioned that a so-called EP1t point is in fact an intersection point between the loci of two global bifurcations involving saddle periodic orbits, namely an EtoP heteroclinic connection and a PtoE heteroclinic tangency. We argued in chapter 2 that an EP1t point is one of the organizing centres of the global dynamics of the FHN model, and that, locating the global objects helps us to obtain a clearer understanding of the complex bifurcation structure of the FHN model.

Developing robust algorithms to calculate different types of global objects in a dynamical system has been an active research field for a long time (Beyn, 1990; Doedel and Friedman, 1989; Friedman and Doedel, 1993; Champneys et al., 1996). Recently, in Krauskopf and Riess (2008), the authors developed an innovative approach to find an EtoP connection in vector fields. The key idea of this approach is to apply Lin's theory (Lin, 1990) to formulate a well-posed boundary value problem. The solution to this boundary value problem corresponds to an EtoP connection. Furthermore, with one EtoP connection obtained with the Lin's approach as an initial condition, a curve of EtoP connections can be found by continuing in system parameters.

Various numerical algorithms for finding and continuing EtoP connections have been developed with different approaches, see e.g., Dieci and Rebaza (2004) and Doedel et al. (2008). An advantage of Lin's approach is that this algorithm can be applied to find more complicated global objects. For instance, some new features of the bifurcation set (e.g., EtoP bifurcations and EP1t bifurcation point) of the FHN model shown in chapter 2 were calculated with this algorithm.

In this chapter we show details of how the algorithm developed by Krauskopf and Riess, based on Lin's approach, can be used to find and continue a codimension-one heteroclinic cycle between two periodic orbits (PtoP) in a vector field. A homoclinic orbit from a periodic orbit to itself is an example of a PtoP connection, but is generically structurally stable in a phase space of any dimension. Until now, no example of a concrete vector field with a non-structurally stable PtoP connection was known. We present a first concrete example of a PtoP heteroclinic cycle of codimension one between two different saddle periodic orbits; we found this example in a four-dimensional vector field model of intracellular calcium dynamics. This calcium model is a variant of the prototypical calcium model we considered in chapter 3. We first show that the model is a good candidate system for the existence of such a PtoP cycle and then demonstrate how a PtoP cycle can be detected and continued in system parameters using a numerical setup that is based on Lin's method.

The chapter is structured as follows. In section 6.1, we provide the definition of a PtoP orbit of codimension d and then discuss the specific example of a codimension-one PtoP heteroclinic cycle in $\mathbb{R}^4$; we also briefly discuss the Lin's method setup for finding PtoP orbits. In section 6.2, we introduce the four-dimensional prototypical model for intracellular calcium dynamics. We first use a partial bifurcation set to demonstrate that this model has the geometric elements required for the existence of a codimension-one PtoP heteroclinic cycle. The codimension-one PtoP connection is then computed and the codimension-zero PtoP connection is also found; the codimension-one PtoP cycle is then continued as a curve in two system parameters. Section 6.3 shows how PtoP homoclinic orbits and saddle periodic orbits can be found numerically near the codimension-one PtoP cycle. We summarize our findings in section 6.4.

The work presented in this chapter was done in collaboration with B. Krauskopf and V. Kirk and a manuscript has been accepted for publication (Zhang et al., 2012).

6.1 Introduction to Lin's method

We briefly introduce some important ideas about the Lin's method. First, we introduce some notation, similar to that used in Krauskopf and Riess (2008). We consider a general autonomous vector field denoted by

$$\frac{dx}{dt} = f(x, \lambda), \tag{6.1}$$

where

$$f : \mathbb{R}^n \times \mathbb{R}^m \to \mathbb{R}^n \tag{6.2}$$

is sufficiently smooth; we assume that the function f is at least twice differentiable. Here $\mathbb{R}^n$ is the phase space of (6.1) and the parameter λ is a vector in $\mathbb{R}^m$. We denote the flow of (6.1) by ϕ^t. Note that all objects involved (equilibria, periodic orbits, their invariant manifolds, etc.) depend on the parameter λ, but we generally do not indicate this explicitly in the notation. The unstable and stable manifolds of a periodic orbit Γ are denoted as

$$W^u(\Gamma) := \{x \in \mathbb{R}^n \mid \lim_{t\to-\infty} \operatorname{dist}(\phi^t(x), \Gamma) = 0\}, \tag{6.3}$$

and

$$W^s(\Gamma) := \{x \in \mathbb{R}^n \mid \lim_{t\to\infty} \operatorname{dist}(\phi^t(x), \Gamma) = 0\}, \tag{6.4}$$

respectively.

6.1.1 PtoP connection of codimension d

We consider here a heteroclinic connecting orbit Q of system (6.1), between two hyperbolic periodic orbits Γ_1 and Γ_2, that exists for a given value of the parameter $\lambda = \lambda^*$. Specifically, we assume that the connection is such that the flow is from Γ_2 to Γ_1, meaning that the orbit Q belong to the intersection between the unstable manifold of Γ_2 and the stable manifold of Γ_1 ($Q \in W^u(\Gamma_2) \cap W^s(\Gamma_1) \subset \mathbb{R}^n$); if necessary, this can be achieved by reversing time in system (6.1). We further assume that the following conditions are satisfied.

(C1) The periodic orbit Γ_1 is hyperbolic and its stable manifold $W^s(\Gamma_1)$ is of dimension $k \geq 2$.

(C2) The periodic orbit Γ_2 is hyperbolic and its unstable manifold $W^u(\Gamma_2)$ is of dimension $l \geq 2$.

(C3) $k + l \leq n$.

(C4) The connecting orbit Q at $\lambda = \lambda^*$ is isolated.

(C5) The λ-dependent families of $W^u(\Gamma_2)$ and $W^s(\Gamma_1)$ intersect transversely in the product $\mathbb{R}^{n+m}$ of phase space and parameter space.

Note that the conditions (C1)–(C5) ensure that the only source of codimension of the PtoP connection is due to the dimensions of the two global manifolds $W^u(\Gamma_2)$ and $W^s(\Gamma_1)$, so that $Q \in W^u(\Gamma_2) \cap W^s(\Gamma_1) \subset \mathbb{R}^n$ has codimension $d := n + 1 - k - l$. Note also that $d \geq 1$ due to (C3). The PtoP connection Q can be found along an $(m - d)$-dimensional subspace of the m-dimensional parameter region Λ. In particular, one encounters the PtoP connection Q generically for $m \geq d$. If the condition (C3) is not satisfied, i.e., $k + l > n$, the PtoP connection Q is structurally stable, and we say that Q is of codimension zero.

There is an important difference with the case of EtoP connections. One may find codimension-one EtoP orbits in the phase space $\mathbb{R}^3$ when the dimension of the unstable manifold $W^u(p)$ of the equilibrium p is one. A well-known example of such an EtoP connection was found in the Lorenz system (Aguirre et al., 2011; Doedel et al., 2006, 2008; Krauskopf and Riess, 2008), and other examples of EtoP connections can also be found in Dieci and Rebaza (2004) and Pampel (2001). For PtoP connections, on the other hand, the dimensions k and l of $W^u(\Gamma_2)$ and $W^s(\Gamma_1)$, respectively, are at least two, so that a PtoP connection Q with codimension $d \geq 1$ can be found in the phase space $\mathbb{R}^n$ only for $n \geq 4$. It also requires that $\Gamma_1 \neq \Gamma_2$, that is, the PtoP connection is a heteroclinic orbit between two different periodic orbits. Note that any homoclinic PtoP connection of a periodic orbit $\Gamma = \Gamma_1 = \Gamma_2$ is of codimension zero for any dimension n of the phase space, because the dimensions of $W^u(\Gamma)$ and $W^s(\Gamma)$ for any $\Gamma \in \mathbb{R}^n$ add up to $n + 1$.

6.1.2 Codimension-one PtoP connection in $\mathbb{R}^4$

We would like to find such a codimension-one PtoP heteroclinic cycle Q in a four-dimensional system, since it has the lowest possible phase space in which Q could exist. The first task is to come up with a strategy to identify the position where one might find two periodic orbits Γ_1 and Γ_2 with the required properties in the parameter space. We propose here to look in a two-dimensional parameter plane near a curve of saddle-node bifurcations of periodic orbits that creates Γ_1 and Γ_2 as saddle periodic orbits in $\mathbb{R}^4$. It is required that Γ_1 has a three-dimensional unstable manifold $W^u(\Gamma_1)$ and a two-dimensional stable manifold $W^s(\Gamma_1)$, while Γ_2 has a three-dimensional stable manifold $W^s(\Gamma_2)$ and a two-dimensional unstable manifold $W^u(\Gamma_2)$. Furthermore, the two-dimensional manifold $\mathcal{Q}_0 = W^u(\Gamma_1) \cap W^s(\Gamma_2)$ is a topological cylinder that is bounded by Γ_1 and Γ_2 in the phase space. In other words, Γ_1 and Γ_2 have the correct local properties as listed in (C1)–(C5). The main question is whether the two-dimensional manifolds $W^u(\Gamma_2)$ and $W^s(\Gamma_1)$ are close enough to each other, so that they may pass through each other along a suitable path in the two-dimensional parameter space. If they do then the codimension-one PtoP connection Q_1 also exists and the heteroclinic cycle is complete at the corresponding parameter values λ^* along a curve in the parameter plane.

6.1.3 Finding a PtoP connection with Lin's method

The mathematical setup of Lin's method for a PtoP connecting orbit Q is a direct generalization of the corresponding setup for EtoP orbits except that the role of the saddle equilibrium is taken by another saddle periodic orbit. Consider a cross section Σ (an $(n-1)$-dimensional submanifold) that intersects Q transversely and separates Γ_1 and Γ_2 in the phase space. In many situations such a section can be found in the convenient linear form

$$\Sigma = \{x \in \mathbb{R}^n \mid \langle x - p_\Sigma, n_\Sigma \rangle = 0\}, \tag{6.5}$$

where p_Σ is a point in Σ and n_Σ is a fixed normal vector to the section Σ. Note that transversality of the flow of (6.1) to Σ can be assured in practice at least locally near the orbit Q, even when Q is not yet known. We now consider the parameter neighborhood Λ of λ^* and define for all λ-dependent ($\lambda \in \Lambda$) orbit segments

$$\begin{aligned} Q^- &= \{q^-(t) \mid t \leq 0\} \subset W^u(\Gamma_2) \quad \text{where} \quad q^-(0) \in \Sigma, & (6.6)\\ Q^+ &= \{q^+(t) \mid t \geq 0\} \subset W^s(\Gamma_1) \quad \text{where} \quad q^+(0) \in \Sigma, & (6.7)\end{aligned}$$

from Γ_2 to Σ and from Σ to Γ_1, respectively. The integration times from Γ_2 to Σ and from Σ to Γ_1 are denoted as T^- and T^+, respectively.

The key idea of Lin's theory (Lin, 1990) is that the difference of the points on the section, i.e., $q^-(0) - q^+(0) \in \Sigma$, can be required to lie in a d-dimensional linear subspace Z, which is referred to as the Lin space.

Suppose that system (6.1) has a PtoP connection Q satisfying conditions (C1)–(C5), and let Z be a d-dimensional space with basis $z_1, \cdots, z_d$. Then, in some neighbourhood Λ of λ^*, for any $\lambda \in \Lambda$ the difference between Q^- and Q^+ as defined by (6.6) and (6.7) is uniquely defined by the function:

$$\xi(\lambda) := q^+(0) - q^-(0) \in Z.$$

Furthermore, there are d smooth functions $\eta_i : \mathbb{R}^m \to \mathbb{R}$ such that

$$\xi(\lambda) = \sum_{i=1}^{d} \eta_i(\lambda) z_i \quad \text{and} \quad \eta_i(\lambda^*) = 0 \ \text{ for all } \ i = 1, \ldots, d.$$

This statement is typical for any setup of Lin's method. The underlying idea is to consider so-called Lin orbits, which may consist of any finite number of orbit segments with 'jumps' in suitable Lin spaces from one orbit segment to the next; see, for example, Knobloch (2000) and Yew (2001). Each such Lin orbit is well defined. When all jumps, that is, all Lin gaps, are zero then one has found the desired global orbit. This approach can be used to study EtoP and PtoP connections, as well as more general heteroclinic networks involving periodic orbits; see Knobloch (2000), Knobloch and Riess (2010) and Rademacher (2005) for more details. The main step in proving the general Lin's method is to show the uniqueness of the orbit segments Q^- and Q^+ for any $\lambda \in \Lambda$. The properties of the functions η_i are a consequence of this uniqueness. Since the matrix $D\xi$ is non-singular due to condition (C5), the $\eta_i(\lambda)$, which we refer to as the Lin gaps, are well-defined test functions with regular zero solutions, including a joint regular zero solution at λ^*. An approach to finding an unknown PtoP connection Q is, therefore, to continue the λ-dependent orbit segments Q^- and Q^+ in parameters until all Lin gaps $\eta_i(\lambda)$ are closed.

This Lin's method setup is sketched in Fig. 6.1 for the lowest-dimensional case of a codimension-one heteroclinic PtoP connection in $\mathbb{R}^4$ with $k = l = 2$; then the Lin space Z is of dimension one, and the PtoP connection can be found at an isolated point λ^* of a single parameter $\lambda \in \mathbb{R}$. The situation depicted in panel (a) is for λ near λ^*. The two-dimensional manifolds $W^u(\Gamma_2)$ and $W^s(\Gamma_1)$ of the periodic orbits Γ_2 and Γ_1 are shown up to the three-dimensional section Σ, which they intersect in one-dimensional curves (shown in the figure as two circles). The orbit segments $Q^- \subset W^u(\Gamma_2)$ and $Q^+ \subset W^s(\Gamma_1)$ end in Σ. The difference of their endpoints $q^+(0)$ and $q^-(0)$ lies along the one-dimensional Lin space Z, giving rise to the single Lin gap $\eta_1(\lambda) = q^+(0) - q^-(0) \neq 0$. While Q^- and Q^+ are continued in the parameter λ, the Lin gap $\eta_1(\lambda)$ can be monitored. As is shown in Fig. 6.1(b), at the root λ^* of $\eta_1(\lambda)$ the orbit segments Q^- and Q^+ match up to form the PtoP connecting orbit Q. Note that $\eta_1(\lambda)$ undergoes a sign change at λ^* because it is regular zero solution.

6.1.4 Implementation of the method

The setup of Lin's method presented in the previous section can be implemented numerically by formulating a system of boundary value problems (BVP) for all the dynamic objects involved, which typically includes Γ_1 and Γ_2, their unstable and stable eigenfunctions and finite-time approximations of the orbit segments Q^- and Q^+. In fact, the continuation of families of orbit segments is a very powerful and accurate general numerical method for the investigation of global objects in a dynamical system, such as invariant manifolds, connecting orbits and slow manifolds; see Aguirre et al. (2011) and Krauskopf et al. (2007) for more details. The key step is to formulate a suitable

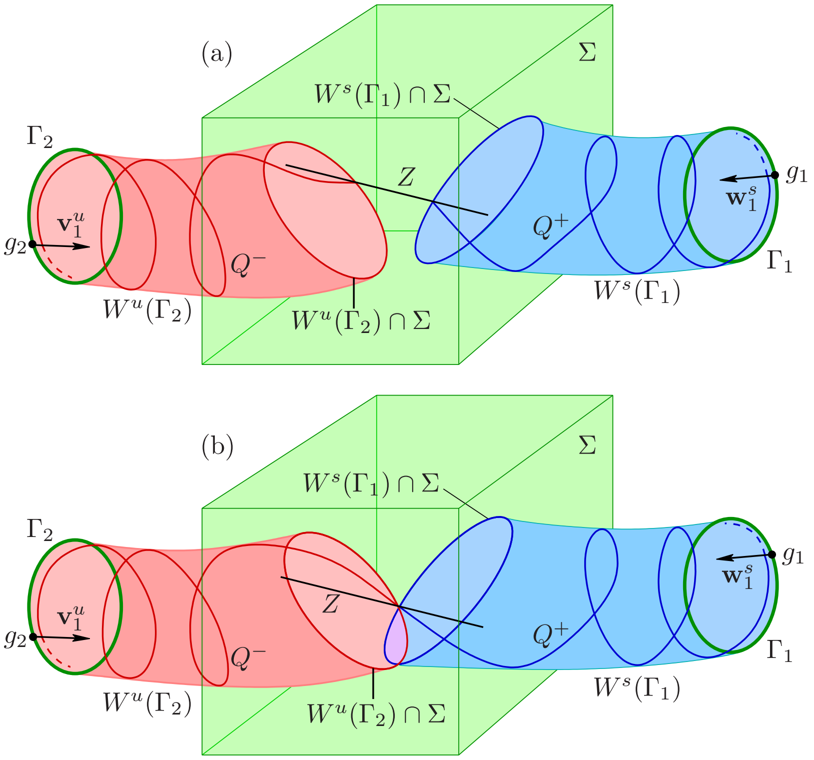

Figure 6.1: Schematic diagram illustrating the Lin's method setup for finding a codimension-one PtoP connecting orbit in $\mathbb{R}^4$. The end points of the two orbit segments, $Q^- \subset W^u(\Gamma_2)$ and $Q^+ \subset W^s(\Gamma_1)$, in the three-dimensional section Σ lie in the one-dimensional Lin space Z; in the numerical approximation Q^- and Q^+ are truncated to orbit segments whose other end points lie on vectors $\mathbf{v}_1^u$ and $\mathbf{w}_1^s$ in the respective unstable and stable eigenspaces at points $g_2 \in \Gamma_2$ and $g_1 \in \Gamma_1$, respectively. Panel (a) shows a nonzero Lin gap along the one dimensional subspace Z for λ near λ^*, and panel (b) shows the PtoP connection $Q = Q^- \cup Q^+$ for $\lambda = \lambda^*$ when the gap is closed.

parameterized system of well-posed BVP, which can then be solved, for example, with the collocation solver of the numerical package AUTO. Solutions of the BVP can then be continued in parameters with AUTO's pseudo-arclength continuation routine.

A detailed guide to the setup of boundary value problems for general systems can be found in Krauskopf and Riess (2008) and Doedel et al. (2008, 2009). We illustrate Lin's approach by finding various global bifurcations involving saddle periodic orbits in a four-dimensional calcium model in the next section, including a codimension-one PtoP connection in section 6.2.2.

6.2 A codimension-one PtoP cycle in a calcium model

Since it is not at all a straightforward task to find a vector field (of dimension at least four) that features orbits Γ_1 and Γ_2 with the required properties (C1)–(C5), all examples of PtoP connecting orbits considered so far in the literature (Dieci and

Rebaza, 2004; Doedel et al., 2009; Krauskopf and Riess, 2008; Pampel, 2001) are of codimension-zero. The lowest-dimensional example of a PtoP connecting orbit that is not structurally stable requires $n = 4$, $k = 2$ and $l = 2$ so that the connection is of codimension $d = 1$. Notice that such a PtoP connection of codimension one will often be part of a heteroclinic cycle. More specifically, in the $\mathbb{R}^4$ phase space the global manifolds $W^u(\Gamma_1)$ and $W^s(\Gamma_2)$, which are of dimension $(n+1-k) = 3$ and $(n+1-l) = 3$, respectively, would generally intersect in a two-dimensional manifold. In other words, a codimension-one connection from Γ_2 to Γ_1 exists on a curve in the $\mathbb{R}^4$ phase space, while a codimension-zero connection from Γ_1 to Γ_2 exists on a two-dimensional surface in the $\mathbb{R}^4$ phase space.

In this section we show that this type of codimension-one PtoP heteroclinic cycle indeed exists near a saddle-node of periodic orbits bifurcation in a simplified four-dimensional model of intracellular calcium dynamics. To this end, we employ the numerical implementation of Lin's method.

6.2.1 Calcium model description and partial bifurcation set of the model

The calcium equations we discuss here are very similar to the prototypical calcium system (3.2) discussed in chapter 3. However, as mentioned before, the lowest dimension of a model which has a codimension-one PtoP heteroclinic cycle is four, and so we consider a four-dimensional variant of the prototypical calcium system in the travelling wave coordinates as follows:

$$\begin{aligned}
\frac{dc}{d\xi} &= v, \\
D\frac{dv}{d\xi} &= sv - \Big(\alpha + k_f \frac{c^2}{c^2+\varphi_1^2} n\Big)\Big(\frac{\gamma(c_t + Dv - sc)}{s} - c\Big) + k_s c - \varepsilon(J - k_p c), \\
\frac{dc_t}{d\xi} &= \varepsilon(J - k_p c), \\
s\frac{dn}{d\xi} &= \frac{1}{2}\Big(\frac{\varphi_2}{\varphi_2 + c} - n\Big).
\end{aligned} \tag{6.8}$$

The form of equations (6.8) is more or less the same as equations (3.7), except that we introduce an extra dynamical variable n which represents the proportion of IP_3 receptors that have not been inactivated by calcium. All the other variables and parameters have the same meaning as those in equations (3.7). The parameter values for the numerical computation of equations (6.8) are given in Table 3.1, with the bifurcation parameters being J and s. Note that if the variable n is set to its quasi-steady state value, then we can reduce the four-dimensional system (6.8) to the three-dimensional system (3.7).

It was argued in chapter 3 that a large number of reaction-diffusion calcium travelling wave equations have a similar bifurcation structure of homoclinic and periodic solutions, referred to as the “CU” structure (Champneys et al., 2007, 2009). Specifically, these calcium models have a C-shaped curve of homoclinic bifurcation and a U-shaped curve of Hopf bifurcation on a parameter plane. Unsurprisingly, equations (6.8) also have this bifurcation structure, as shown in panel (a) of Fig. 6.2.

Equations (6.8) have a single equilibrium solution p, which is always of saddle type, having one negative eigenvalue and three eigenvalues with positive real part inside the region bounded by the Hopf curve (labelled H in Fig. 6.2), and having one positive eigenvalue and three eigenvalues with negative real part outside this region. The equilibrium undergoes a Hopf bifurcation on this U-shaped locus.

The C-shaped curve of homoclinic bifurcations of p is labelled hom in Fig. 6.2. The numerics suggest that the upper end of the C-shaped homoclinic bifurcation curve terminates at a codimension-two Shil’nikov-Hopf bifurcation point (Deng and Sakamoto, 1995; Hirschberg and Knobloch, 1993) when the homoclinic curve reaches a supercritical Hopf bifurcation on the U-shaped Hopf curve.

Unlike the case near the upper end, the lower end of the C-shaped curve does not reach the Hopf bifurcation curve. Instead, the homoclinic curve has a sharp turning point, with the branch tracing back on its locus in the parameter plane and stopping near a Belyakov bifurcation point (Belyakov, 1980) where the saddle-quantity of the equilibrium is equal to zero. Complex dynamics are known to arise in the neighbourhood of such Belyakov bifurcation points (Kuznetsov et al., 2001). In particular, we can find a saddle-node bifurcation of periodic orbits (SL) and a heteroclinic connection from the equilibrium point to a periodic orbit (EtoP), among other bifurcations.

These two codimension-one bifurcations can be followed in the (J, s) parameter plane, resulting in panel (b) of Fig. 6.2. The SL bifurcation curve stops at a degenerated Hopf point on the U-shaped Hopf bifurcation curve. The EtoP bifurcation curve terminates at the Hopf bifurcation curve, since across the Hopf bifurcation curve the EtoP connection is structurally stable (of codimension zero). In the small parameter region of panel (b) of Fig. 6.2, there are two periodic orbits, Γ_1 and Γ_2, created on the SL bifurcation curve. Furthermore, a heteroclinic connection from the equilibrium p to the periodic orbit Γ_2 also exists. Indeed, Γ_1 and Γ_2 near the SL bifurcation curve of the calcium model (6.8) have all the local properties listed in (C1)–(C5). Therefore, we can hope to find a codimension-one heteroclinic connection between these two periodic orbits in this region.

The existence of a codimension-one EtoP heteroclinic cycle gives a strong hint of the existence of a codimension-one PtoP heteroclinic cycle, and the setup to find these global bifurcations involving saddle periodic orbits is quite similar. To find a heteroclinic cycle between the equilibrium p and the periodic orbit Γ_2 means to find a

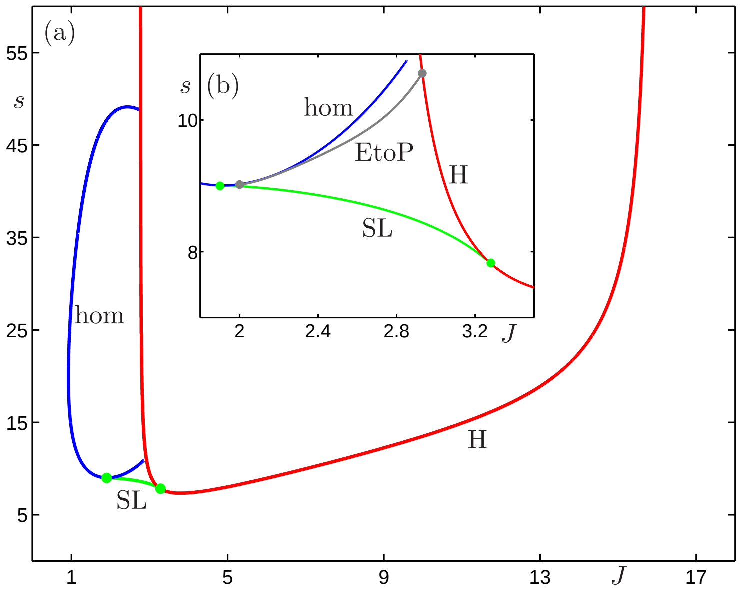

Figure 6.2: Panel (a) shows a partial bifurcation set in the (J, s)-plane for equations (6.8), consisting of a C-shaped curve (labelled hom) of homoclinic bifurcations and a U-shaped curve (labelled H) of Hopf bifurcations, which are connected by a curve of saddle-node of limit cycles bifurcations (labelled SL). Panel (b) is an enlargement near the curve SL, and also shows a curve of EtoP connections with end points on the curves H and hom.

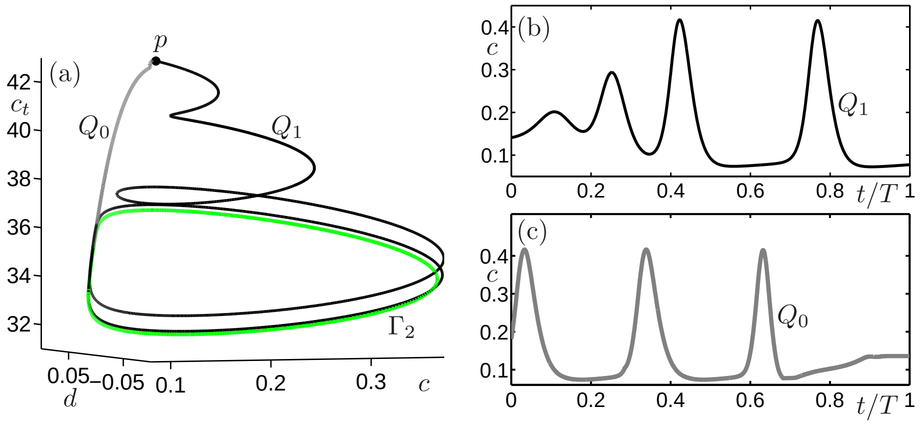

Figure 6.3: Panel (a) shows the EtoP cycle for $s = 10.0$ and $J = 2.71917$ between the equilibrium p and the periodic orbit Γ_2, which consists of the codimension-one EtoP connection Q_1 and the codimension-zero EtoP connection Q_0. Time traces (of the variable c) of the computed orbit segments Q_1 and Q_0 are shown in panels (b) and (c), respectively.

'forward' connection from the equilibrium p to the periodic orbit Γ_2 and the 'backward' connection from the periodic orbit Γ_2 to the equilibrium p. The method used to find these connections is similar to the one described in Krauskopf and Riess (2008). Specifically, the connection Q_1 from p to Γ_2 is of codimension one, and it occurs when the one-dimensional unstable manifold $W^u(p)$ lies in the three-dimensional stable manifold $W^s(\Gamma_2)$; see Fig. 6.3(a) and the time series of the variable c along Q_1 in panel (b). There also exists a structurally stable heteroclinic connection from Γ_2 back to p, which is the intersection of the two-dimensional unstable manifold $W^u(\Gamma_2)$ with the three-dimensional stable manifold $W^s(p)$; see Fig. 6.3(a) and the time series along Q_0 in panel (c). Once it was found as the solution of the corresponding BVP from Krauskopf and Riess (2008), the locus of codimension-one EtoP connections was continued to yield the curve labelled EtoP in Fig. 6.2(b). This curve has one end point at $(J_{\text{in}}, s) = (2.93121, 10.51281)$ on the Hopf bifurcation curve and another end point at $(J_{\text{in}}, s) = (2.04216, 9.04523)$ on the homoclinic bifurcation curve (near the Belyakov point). In the region of interest we also find the second periodic orbit Γ_1, which bifurcates from the curve H in Fig. 6.2(b) and, hence, is quite close to the equilibrium p. Therefore, the existence of the EtoP connections from p to Γ_2 and back strongly suggests that there may also be a PtoP cycle between Γ_1 and Γ_2. Overall, we conclude that the global geometry of the phase space of (6.8) looks very promising for the hunt for a codimension-one PtoP cycle.

6.2.2 Lin's method for the heteroclinic connection between periodic orbits

We now demonstrate how a heteroclinic connection between periodic orbits can be found in model (6.8). We set the secondary parameter $s = 9.0$ initially. Two Hopf bifurcation points at $J \approx 3.04800$ and $J \approx 6.04467$ can be found as we vary the primary bifurcation parameter J. One periodic orbit Γ_1 can be found by continuation from the first Hopf bifurcation at $J \approx 3.04800$ and the other periodic orbit Γ_2 can be found by continuation from the other Hopf bifurcation at $J \approx 6.04467$.

Inspection of the Floquet multipliers shows that Γ_1 is of saddle type with a three-dimensional unstable manifold and a two-dimensional stable manifold while Γ_2 is also of saddle type with a two-dimensional unstable manifold and a three-dimensional stable manifold. The periodic orbits and their corresponding unstable and stable manifolds can be continued in system parameters. The continuation is stopped at $J = 3.0$, which is a point close to the SN bifurcation curve in the region of interest in the parameter plane, which agrees with the strategy discussed in section 6.1.2.

Since the unstable manifold of Γ_1 is three-dimensional and the stable manifold of Γ_2 is three-dimensional so the connection from Γ_1 to Γ_2 is of codimension zero. On the other hand, the stable manifold of Γ_1 is two-dimensional and the unstable manifold of Γ_2 is two-dimensional so the backward connection from Γ_2 to Γ_1 is codimension one.

We define the section

$$\Sigma = \{(c, d, c_t, n) \mid c_t = 36.0\},$$

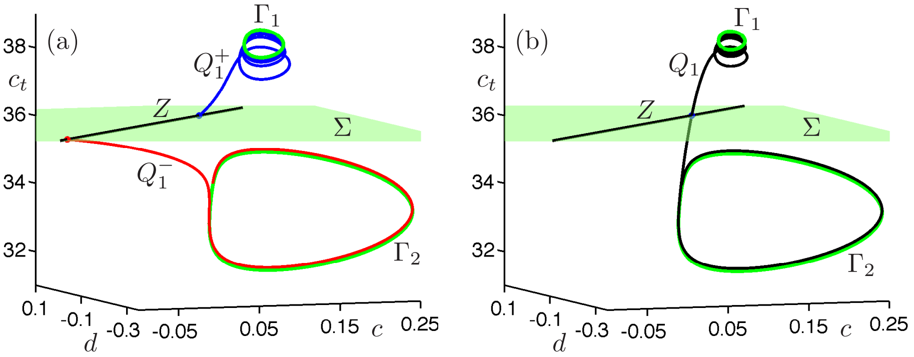

Figure 6.4: Computing the codimension-one PtoP connection Q_1 for $s = 9.0$. Panel (a) for $J = 3.0$ shows two initial orbit segments Q_1^- from Γ_2 to $\Sigma = \{c_t = 36.0\}$ and Q_1^+ from Σ to Γ_1 with a Lin gap in Σ of $\eta = 0.4065$ along the direction Z. Panel (b) shows the connecting orbit Q_1 for $J = 3.02661$ where $\eta = 0$.

for which $p_\Sigma = (0, 0, 36, 0)$ and $n_\Sigma = (0, 0, 1, 0)$ in (6.5). The section Σ divides the phase space of (6.8) into two parts, one containing Γ_1 (where $c_t < 36.0$) and the other containing Γ_2 (where $c_t > 36.0$). Hence, any orbit connecting Γ_1 and Γ_2 must cross the section Σ.

The codimension-one PtoP connection

We first consider the PtoP connecting orbit Q_1 from Γ_2 to Γ_1 that, if it exists, is of codimension one, since we have $n = 4$, $k = 2$, $l = 2$, and $d = 1$. An initial orbit segment Q_1^+ from Σ to Γ_1 can be obtained by continuation in T^+ from a base point $g_1 = (0.1347, 0.0023, 38.2595, 0.8728) \in \Gamma_1$ along the associated one-dimensional stable eigenspace $E^s(\Gamma_1)$, which is spanned by Floquet vectors $\mathbf{w}_1^s = (0.0108, -0.0064, 0.9981, -0.0606)$ corresponding to the stable Floquet multiplier $\mu_1^s = 0.3387$ with the initial distance along this vector $\delta_1 = 10^{-4}$. Similarly, another orbit segment Q_1^- from Γ_2 to the section Σ is found by performing a continuation in the integration time T^- from a base point $g_2 = (0.0915, 0.0019, 34.0078, 0.8833) \in \Gamma_2$ along the associated Floquet vector $\mathbf{v}_1^u = (-0.1997, -0.1630, 0.9661, 0.0106)$ of the unstable Floquet multiplier $\mu_1^u = 95340$ with the initial distance along the vector $\varepsilon_1 = 10^{-6}$. Figure 6.4(a) shows the periodic orbits Γ_1 and Γ_2, the section Σ and the orbit segments Q_1^- and Q_1^+ for $(J, s) = (3.0, 9.0)$ in projection onto (c, d, c_t)-space. Also shown is the Lin space Z, which we also refer to as the Lin direction because it is of dimension $d = 1$. It is chosen here as the line through the two end points $Q_1^- \cap \Sigma$ and $Q_1^+ \cap \Sigma$ for $(J, s) = (3.0, 9.0)$, and is spanned by a direction vector z_1; the initial Lin gap is $\eta_1 = 0.4065$ in Fig. 6.4(a). We stress that the Lin vector z_1 is kept fixed throughout further computations, that is, it is not allowed to change with system parameters. After these initial computations, the overall BVP for both Γ_1 and Γ_2 can be continued in a single system parameter. Specifically, we continue Q_1^- and Q_1^+ as solutions of the

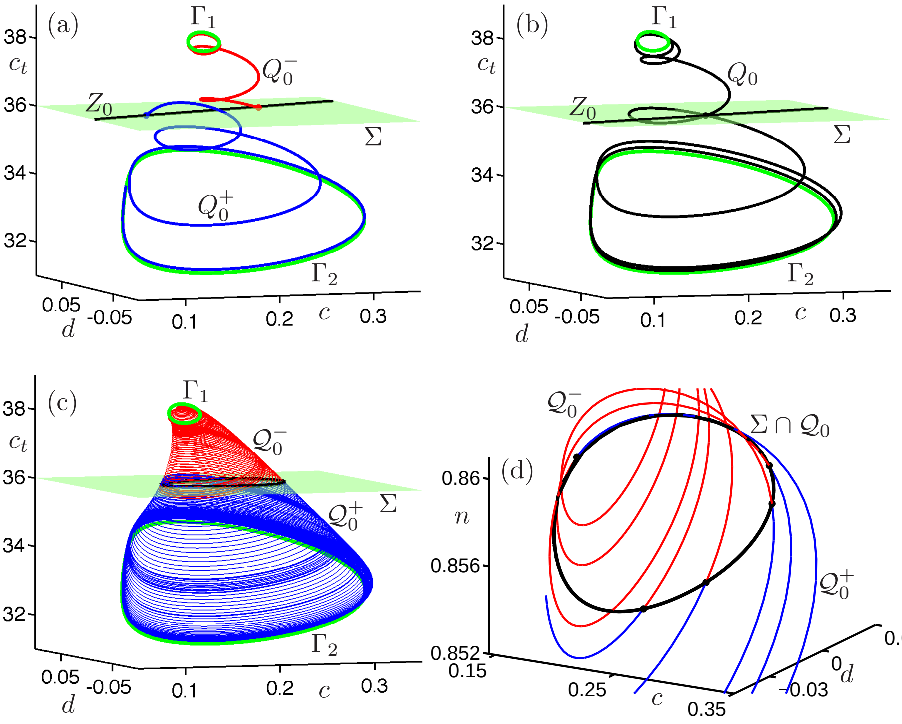

Figure 6.5: Computing the cylinder $\mathcal{Q}_0$ of codimension-zero PtoP connections from Γ_1 to Γ_2 for $s = 9.0$ and $J = 3.02661$. Panel (a) shows two initial orbit segments Q_0^- from Γ_1 to $\Sigma = \{c_t = 36.0\}$ and Q_0^+ from Σ to Γ_2 with a gap in Σ of $\eta_0 = 0.1624$ along the direction Z_0. Panel (b) shows a codimension-zero PtoP connecting orbit Q_0 where $\eta_0 = 0$. Panel (c) shows the one-parameter families $\mathcal{Q}_0^-$ and $\mathcal{Q}_0^+$ that form a cylinder of connecting PtoP orbits, and panel (d) is an enlargement of $\mathcal{Q}_0^-$ and $\mathcal{Q}_0^+$ near their intersection curve $\mathcal{Q}_0 \cap \Sigma$.

overall BVP in the parameter J and thus detect that $\eta_1 = 0$ for $J = 3.02661$. Figure 6.4(b) depicts the corresponding codimension-one PtoP connection Q_1 from Γ_1 to Γ_2, which is the concatenation of the two orbit segments Q_1^- and Q_1^+.

The codimension-zero PtoP connection

We next find the codimension-zero connection Q_0 from Γ_1 to Γ_2 at $(J, s) = (3.02661, 9.0)$. The roles of Γ_1 and Γ_2 are now exchanged in the formulation of the BVP. Furthermore, $n = 4$, $k = 3$ and $l = 3$, so that $W^u(\Gamma_1)$ intersects $W^s(\Gamma_2)$ in a two-dimensional surface. First, we consider an orbit segment Q_0^- whose starting point lies near the base point $g_1 = (0.1405, 0.0020, 38.2727, 0.8708) \in \Gamma_1$ along the associated two-dimensional unstable eigenspace $E^u(\Gamma_1)$, which is spanned by Floquet vectors $\mathbf{v}_1 = (0.8676, -0.3284, 0.1326, -0.3491)$ and $\mathbf{v}_2 = (-0.1038, -0.0434, 0.9936, 0.0092)$ of the unstable Floquet multipliers $\mu_1^u = 1.3045$ and $\mu_2^u = 695.9515$; initial distances along these vectors are $\varepsilon_1 = 10^{-4}$ and $\varepsilon_2 = 10^{-6}$, respectively. Continuation in the integration time T^- is performed until the end point of Q_0^- lies in the section Σ. Secondly and similarly, we find an orbit segment Q_0^+ whose starting point lies in Σ and whose end point lies near the base point $g_2 = (0.0919, 0.0020, 33.9624, 0.8823) \in \Gamma_2$ in the corresponding two-dimensional stable eigenspace $E^s(\Gamma_2)$, which is spanned by associated Floquet vectors $\mathbf{w}_1 = (-0.0059, -0.0001, 0.9914, -0.1310)$ and $\mathbf{w}_2 = (0.2051, -0.1042, 0.9692, 0.0884)$ of the stable Floquet multipliers $\mu_1^s = 0.2757$ and $\mu_2^s = 0.0077$; initial distances along these vectors are $\delta_1 = 10^{-4}$ and $\delta_2 = 10^{-6}$, respectively. The periodic orbits Γ_1 and Γ_2 and the orbit segments Q_0^- and Q_0^+ up to Σ for $(J, s) = (3.02661, 9.0)$ are shown in Fig. 6.5(a) in projection onto (c, d, c_t)-space. To find an actual PtoP connection we adapt a numerical setup that was first employed in Krauskopf and Riess (2008). Specifically, we define the one-dimensional space Z_0 as the direction given by $Q_0^- \cap \Sigma$ and $Q_0^+ \cap \Sigma$, spanned by the vector z_0. While Z_0 is not a Lin space, it plays a similar role during the computation and remains fixed. The initial gap size along Z_0 is $\eta_0 = 0.1624$. The idea is now to continue Q_0^- and Q_0^+ as solutions of this BVP with the gap size η_0 as the main continuation parameter, while all system parameters remain fixed. This continuation for fixed $(J, s) = (3.02661, 9.0)$ yields a zero of η_0, which corresponds to the connecting orbit Q_0 shown in panel (b) of Fig. 6.5.

For fixed closed gap $\eta_0 = 0$, the BVP has six free internal parameters T^-, T^+, ε_1, ε_2, δ_1, δ_2 and five boundary conditions. Hence, a continuation of this BVP with $\eta_0 = 0$ allows us to follow the initial connecting orbit Q_0 (which is not isolated) in internal parameters as it sweeps out the two-dimensional surface $\mathcal{Q}_0$ of connecting orbits from Γ_1 to Γ_2. The surface $\mathcal{Q}_0$ is the topological cylinder bounded by the two periodic orbits that is shown in Fig. 6.5(c) in projection onto (c, d, c_t)-space. It consists of two bounded cylinders, $\mathcal{Q}_0^-$ from Γ_1 to Σ and $\mathcal{Q}_0^+$ from Σ to Γ_2, which connect in the section Σ along the closed curve $\mathcal{Q}_0 \cap \Sigma$. Figure 6.5(d) shows $\mathcal{Q}_0 \cap \Sigma$ in (c, d, n)-space, together with selected orbit segments of $\mathcal{Q}_0^-$ and $\mathcal{Q}_0^+$.

Figure 6.6 shows the entire PtoP cycle between Γ_1 and Γ_2 for $(J, s) = (3.02661, 9.0)$ in projection onto (c, d, c_t)-space. The codimension-one PtoP orbit Q_1 connects Γ_2 to Γ_1. The connection from Γ_1 back to Γ_2, on the other hand, consists of a one-parameter family of connecting PtoP orbits (parameterized, for example, by $\mathcal{Q}_0 \cap \Sigma$); it forms the cylinder $\mathcal{Q}_0 = W^u(\Gamma_1) \cap W^s(\Gamma_2)$, which has been rendered in Fig. 6.6 as a two-dimensional surface.

6.2.3 Continuation of the PtoP cycle

The locus of the codimension-one PtoP heteroclinic connection Q_1 can be continued in the system parameters J and s. The resulting curve, labelled PtoP, is shown in Fig. 6.7. The curve has one end point on the curve of saddle-node of limit cycles bifurcations

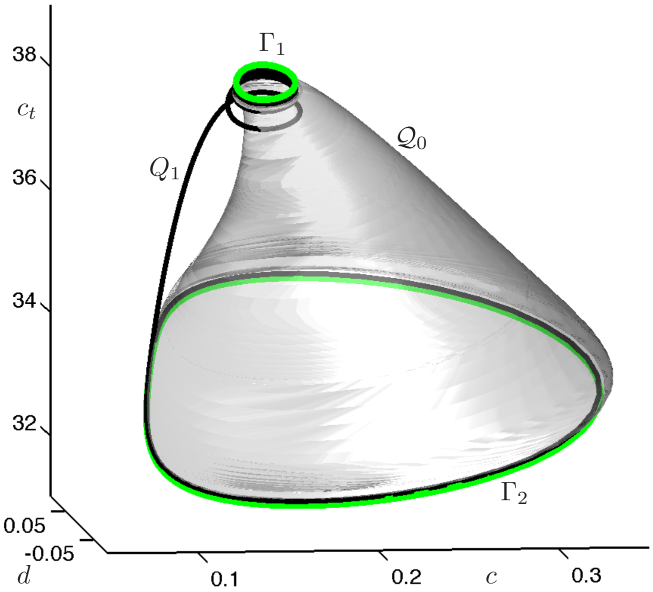

Figure 6.6: The heteroclinic PtoP cycle between Γ_1 and Γ_2 for $(J, s) = (3.02661, 9.0)$, consisting of the the codimension-one PtoP connection Q_1 from Γ_2 to Γ_1 and the bounded cylinder $\mathcal{Q}_0$ of PtoP connections from Γ_1 to Γ_2.

(SL), then follows the Hopf bifurcation curve (H) closely for increasing s and ends on H; see Fig. 6.7(b). Along the curve PtoP we also continued Q_1 and a single connecting orbit Q_0 of the family $\mathcal{Q}_0$ of codimension-zero PtoP connections on the (J, s) parameter plane. This computation confirmed that the entire heteroclinic cycle exists along the curve PtoP in Fig. 6.7.

Figure 6.8(a) shows the heteroclinic PtoP cycle that one finds when $s = 10.0$, and panel (b) shows the heteroclinic cycle for $s = 8.5$. The surface $\mathcal{Q}_0$ was swept out by continuation of the single orbit Q_0. From Fig. 6.8(a) we observe that the amplitude of Γ_1 becomes quite small when s is increased from $s = 9.0$ and the curve PtoP is close to the Hopf bifurcation curve H. At the end point of the curve PtoP on H, the periodic orbit Γ_1 finally disappears in the Hopf bifurcation of the equilibrium p. We found numerically that this happens at $(J, s) = (2.79, 24.64)$. When s is decreased from $s = 9.0$ the periodic orbits Γ_1 and Γ_2 approach one another; see Fig. 6.8(b). Finally, at the end point $(J, s) = (2.98, 8.37)$ of the curve PtoP on the curve SL, the two periodic orbits Γ_1 and Γ_2 meet and disappear.

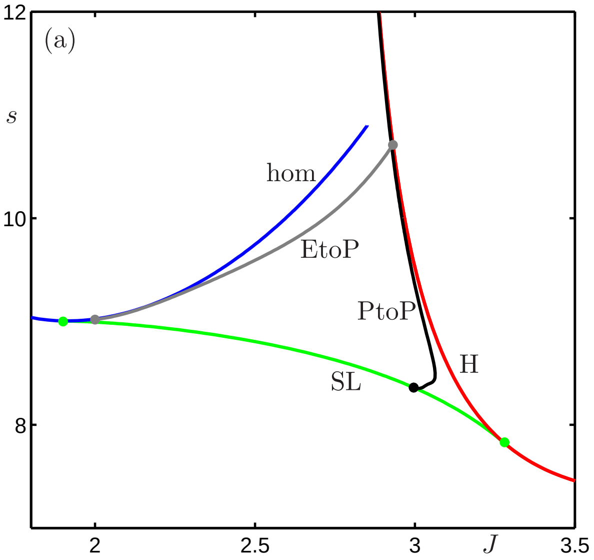

Figure 6.7: Partial bifurcation set in the (J, s) plane of equations (6.8). This figure shows an enlargement of Fig. 6.2(a) with the addition of the curve of codimension-one heteroclinic cycles between Γ_1 and Γ_2 (labelled PtoP), which has end points on the saddle-node of limit cycles bifurcation curve SL and on the Hopf bifurcation curve H. Panel (a) shows the region of interest where the PtoP connection was found, and panel (b) shows the entire PtoP curve.

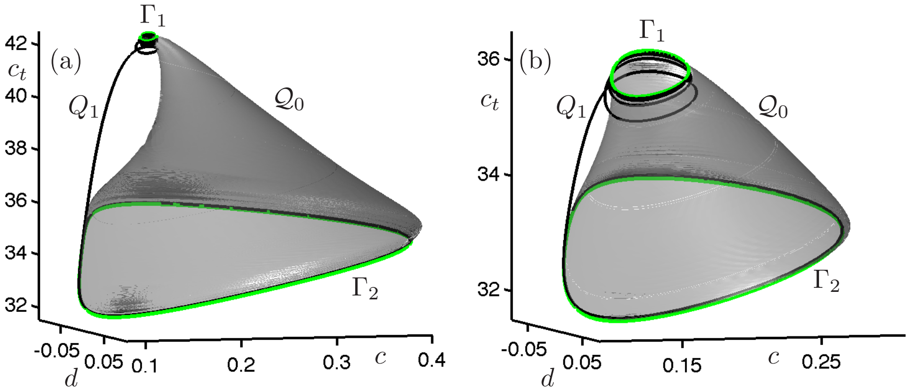

Figure 6.8: The heteroclinic PtoP cycle between Γ_1 and Γ_2 for $(J, s) = (2.95950, 10.0)$ (a) and for $(J, s) = (3.06319, 8.5)$ (b).

6.3 Finding PtoP homoclinic orbits and periodic orbits near the PtoP cycle

In the vicinity of the heteroclinic PtoP cycle between Γ_1 and Γ_2 one can find other dynamical objects, including orbits that are homoclinic to Γ_1 and to Γ_2 and saddle periodic orbits that pass close to Γ_1 and Γ_2. We now show how these objects can be

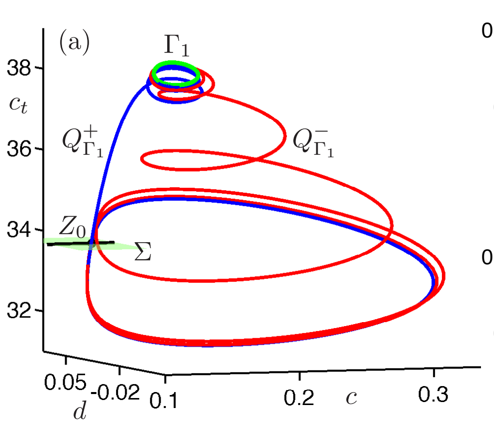

Figure 6.9: Finding a homoclinic PtoP orbit of Γ_1 via the continuation of orbit segments $Q^-_{\Gamma_1}$ and $Q^+_{\Gamma_1}$ that connect Γ_1 with the section $\Sigma = \{c_t = 33.95\}$. Panel (a) shows the start data for $(J, s) = (3.02661, 9.0)$ where $Q^+_{\Gamma_1} = Q_1$ and $Q^-_{\Gamma_1}$ is a connecting orbit in $\mathcal{Q}_0$. Panel (b) shows $Q^-_{\Gamma_1}$ and $Q^+_{\Gamma_1}$ near the direction Z_0 in Σ. In panel (c) the gap along Z_0 has been closed, yielding the homoclinic PtoP orbit Q_{Γ_1} for $(J, s) = (3.02807, 9.0)$.

found numerically with a BVP approach, using the heteroclinic PtoP cycle as start data.

To find a homoclinic orbit connecting Γ_1 to itself we consider two orbit segments: $Q^-_{\Gamma_1}$, which starts near the base point $g_1 \in \Gamma_1$ in the unstable Floquet space and ends at a section Σ near Γ_2, and $Q^+_{\Gamma_1}$, which starts in Σ and ends near g_1 in the stable Floquet space. These orbit segments are readily available from knowledge of the PtoP heteroclinic cycle. Specifically, as start data we set $Q^+_{\Gamma_1} = Q_1$ and $Q^-_{\Gamma_1} \subset \mathcal{Q}_0$. Then the section Σ is chosen to contain the end points of $Q^-_{\Gamma_1}$ and $Q^+_{\Gamma_1}$ near Γ_2. We define the one-dimensional space Z_0 to be the direction in Σ given by these end points; the gap η_0 is measured along Z_0. The setup is the one considered in Krauskopf and Riess (2008) for the computation of homoclinic PtoP orbits, and $Q^-_{\Gamma_1}$ and $Q^+_{\Gamma_1}$ can be represented by and continued as solutions of a BVP. This boundary value problem has a one-dimensional solution manifold, providing five boundary conditions for the six free internal parameters T^-, T^+, ε_1, ε_2, δ_1 and η_0. Figure 6.9(a) and (b) shows the start data for $(J, s) = (3.02661, 9.0)$, given by the orbit segments $Q^-_{\Gamma_1}$ and $Q^+_{\Gamma_1}$, the section $\Sigma = \{c_t = 33.95\}$ and the direction Z_0. In panel (c) the gap along Z_0 has been closed via the continuation of $Q^-_{\Gamma_1}$ and $Q^+_{\Gamma_1}$, and the homoclinic PtoP orbit Q_{Γ_1} has been found as their concatenation.

A homoclinic orbit connecting Γ_2 to itself can be computed in exactly the same

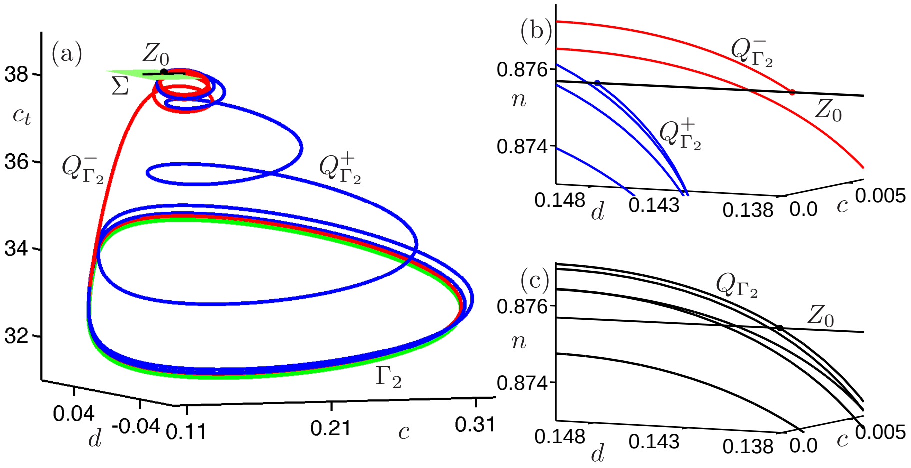

Figure 6.10: Finding a homoclinic PtoP orbit of Γ_2 via the continuation of orbit segments $Q^-_{\Gamma_2}$ and $Q^+_{\Gamma_2}$ that connect Γ_2 with the section $\Sigma = \{c_t = 38.27\}$. Panel (a) shows the start data for $(J, s) = (3.02661, 9.0)$ where $Q^+_{\Gamma_2}$ is a connecting orbit in $\mathcal{Q}_0$ and $Q^-_{\Gamma_2} = Q_1$. Panel (b) shows $Q^-_{\Gamma_2}$ and $Q^+_{\Gamma_2}$ near the direction Z_0 in Σ. In panel (c) the gap along Z_0 has been closed, yielding the homoclinic PtoP orbit Q_{Γ_2} for $(J, s) = (3.02723, 9.0)$.

way, by considering $Q^-_{\Gamma_2}$ and $Q^+_{\Gamma_2}$ from Γ_2 to a section Σ near Γ_1 and back. In fact, the same initial data from the PtoP heteroclinic orbit can be used for these orbits. Specifically, we set $Q^+_{\Gamma_2} \subset \mathcal{Q}_0$ and $Q^-_{\Gamma_2} = Q_1$, with the difference being that Σ is now chosen through the end points of $Q^-_{\Gamma_2}$ and $Q^+_{\Gamma_2}$ near Γ_1. Figure 6.10(a) shows this start data for $(J, s) = (3.02661, 9.0)$, where the section is now $\Sigma = \{c_t = 38.27\}$. Panel (b) shows the direction Z_0 with an initial gap η_0 between the end points of $Q^-_{\Gamma_2}$ and $Q^+_{\Gamma_2}$ in Σ. Continue $Q^-_{\Gamma_2}$ and $Q^+_{\Gamma_2}$ until the gap is closed ($\eta_0 = 0$) to find the homoclinic PtoP orbit Q_{Γ_2}; see Fig. 6.10(c).

In the continuation runs to close the gap η_0 to find the homoclinic PtoP orbits the parameter J was included in the choice of the six free parameters, and Q_{Γ_1} and Q_{Γ_2} were found at the nearby parameter points $(J_{\text{in}}, s) = (3.02807, 9.0)$ and $(J, s) = (3.02723, 9.0)$, respectively. This choice illustrates the general fact that there is considerable flexibility in setting internal and/or system parameters as the free continuation parameters. As such, Q_{Γ_1} and Q_{Γ_2} can be continued (together with the respective periodic orbits and their Floquet vectors) in any system parameter. Figure 6.11 shows results of their continuation in J over the interval $[3.0, 3.04]$, namely, of Q_{Γ_1} in row (a) and of Q_{Γ_2} in row (b). Panels (a1) and (b1) show selected PtoP homoclinic orbits in projection onto (c, d, c_t)-space, demonstrating that they indeed are close to the PtoP heteroclinic cycle between Γ_1 and Γ_2; compare with Fig. 6.6. Notice

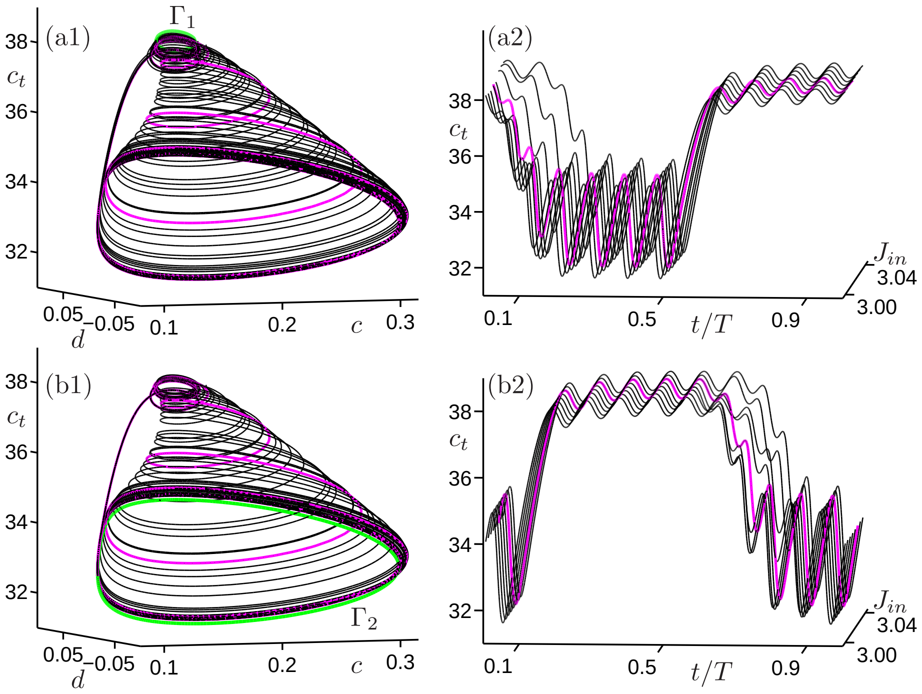

Figure 6.11: PtoP homoclinic orbits of Γ_1 (a1)–(a2) and of Γ_2 (b1)–(b2) continued in the system parameter J over the interval $[3.0, 3.04]$ for fixed $s = 9.0$. Panels (a1) and (b1) shows selected homoclinic orbits in projection onto (c, d, c_t) space, and panels (a2) and (b2) show them as a waterfall diagram of time series of c_t over the unit time interval. The PtoP homoclinic orbits Q_{Γ_1} for $J = 3.02807$ from Fig. 6.9 and Q_{Γ_2} for $J = 3.02723$ from Fig. 6.10 are highlighted.

further from Fig. 6.11(a1) that for any $J \in [3.0, 3.04]$ the PtoP homoclinic orbit Q_{Γ_1} closely follows the codimension-one PtoP connection Q_1 from Γ_2 to Γ_1, while different orbits from the one-parameter family $\mathcal{Q}_0$ of codimension-zero PtoP connections are followed. The waterfall diagram in Fig. 6.11(a2) shows that, as J is increased, the number of loops of Q_{Γ_1} near the periodic orbit Γ_2 decreases from about five to about three; this is consistent with the fact that the computed family Q_{Γ_1} in Fig. 6.11(a1) fills out the entire cylinder of the PtoP heteroclinic cycle in Fig. 6.6 as J varies. The corresponding statement holds for the continuation of the PtoP homoclinic orbits Q_{Γ_2} in Fig. 6.11(b1), where now the number of loops near the periodic orbit Γ_1 increases in panel (b2) from about five to about six.

We finish by showing how saddle periodic orbits near PtoP homoclinic orbits can be computed. As an example we compute a periodic orbit near Q_{Γ_2}. The idea is simply to close the gap between the two end points of Q_{Γ_2}. Therefore, we choose the section $\Sigma = \{c_t = 33.95\}$ and the direction Z_0 defined by these end points, with gap η_0. This initial data is shown in Fig. 6.12(a) and (b). The orbit segment Q_{Γ_2} is a solution of a smaller BVP, which provides one boundary condition for the two free

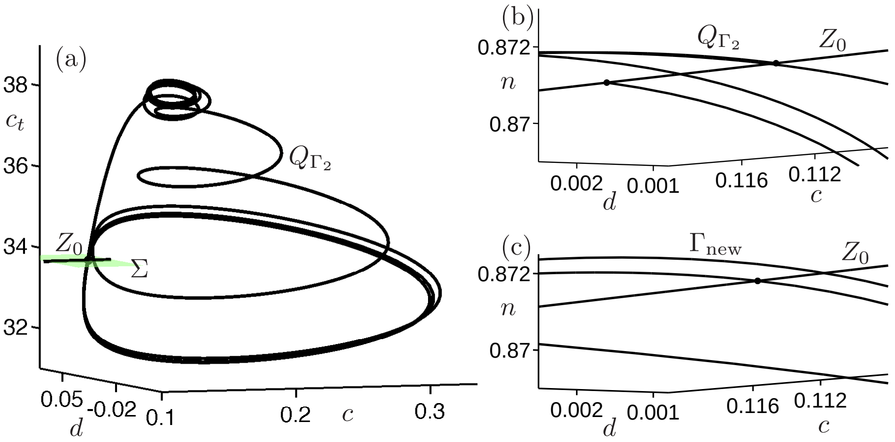

Figure 6.12: Finding a saddle periodic orbit by continuation from the PtoP homoclinic orbit Q_{Γ_2} for $(J, s) = (3.02723, 9.0)$ from Fig. 6.10. Panel (a) shows the orbit segment Q_{Γ_2} whose endpoints lie in the section $\Sigma = \{c_t = 33.95\}$, and panel (b) shows Q_{Γ_2} near the direction Z_0 in Σ. In panel (c) the gap along Z_0 has been closed by continuing in the internal parameters T^- and η_0 until $\eta_0 = 0$, yielding a saddle periodic orbit Γ_{new}.

internal parameters T^- and η_0. Continuing solutions of this BVP until $\eta_0 = 0$ yields a saddle periodic orbit Γ_{new} that closely follows the original PtoP homoclinic orbit Q_{Γ_2}; see Fig. 6.12(c). Once it has been found, Γ_{new} can be continued in system parameters, as usual, as a solution of a standard periodic orbit BVP.

6.4 Summary

We have presented the first example of a concrete vector field in which a non-structurally stable PtoP heteroclinic cycle connecting two saddle periodic orbits has been located numerically. The idea for the algorithm used was developed by Krauskopf and Reiss (Krauskopf and Riess, 2008); the original contribution of the work in this thesis was to find a model in which such a PtoP connection occurs and then to implement the algorithm for this system. Specifically, we showed that a four-dimensional model of intracellular calcium dynamics has a bifurcation structure with the necessary geometric ingredients, and then identified a codimension-one PtoP cycle numerically with an implementation of Lin's method. The PtoP cycle was then continued as a curve in the relevant two parameter plane of the system. We also computed two nearby homoclinic orbits of periodic orbits and a new saddle periodic orbit.

The Lin's method approach that we employed here can be used, in principle, to identify and continue in parameters any homoclinic or heteroclinic chain involving a (finite) number of equilibria and periodic orbits, as well as nearby global objects. The ability to do these kinds of computations can be very useful in the context of applications. For example, it was discussed in chapter 2 that one possible termination mechanism for homoclinic curves in the FHN model was due to a codimension-two EP1t bifurcation point, which was first conjectured in Champneys et al. (2007). However, the EP1t points in the FHN system were not computed previously. Using Lin's method, we were able to find such EP1t points in the FHN model numerically in chapter 2, which helped to explain some complex dynamics observed in the FHN system.

Other global bifurcations such as PtoP heteroclinic bifurcations are also thought to occur near EP1t points, but, similarly, have not been directly computed because of the lack of appropriate numerical algorithms. Thus, the availability of methods such as those outlined in this chapter will enable fuller investigation of models of this type, and may consequently lead to a better understanding of their dynamics.

Chapter 7

Summary and future directions

The work presented in this thesis was primarily motivated by a desire to understand wave solutions in models of intracellular calcium dynamics, specifically in non-excitable cells. We performed detailed numerical experiments on the FitzHugh-Nagumo (FHN) system and various calcium models, and examined singular limits of the models in an attempt to understand the origin of the common features of these models (specifically, the CU bifurcation structure discovered by Champneys et al. (2007)). This work on specific models then inspired more general theoretical work on the validity of reduction methods for biophysical models and some detailed numerical work on implementing a new algorithm for studying global bifurcations. A detailed summary of our results is given below.

In chapter 1, we reviewed some basic cell physiology and discussed some important assumptions for constructing models of intracellular calcium dynamics for non-excitable cells.

In chapter 2, we analyzed the wave solutions of the FHN model. The form of FHN model we study includes a term modelling an applied current and is therefore different from the classical form. With numerical algorithms based on Lin's approach (as discussed in chapter 6), we were able to obtain a more detailed bifurcation set of the FHN model than had previously been obtained. Specifically, we computed the locus of a codimension-two EP1t bifurcation point and some associated curves of global bifurcations which act as organizing centres in the overall dynamics of the FHN equations. The new features of the bifurcation set found in this thesis agree with conjectures made in Champneys et al. (2007) about the FHN model.

The classical form of the FHN model has been widely studied by different people, e.g., Bell and Deng (2002), Deng (1991), Jones et al. (1991), Krupa et al. (1997) and Yanagida (1985). Most analytical results of the FHN model in the classical form were established using the standard techniques of geometric singular perturbation theory (GSPT). In order to make use of the results from previous analysis, we came up with a transformation to change the form of equations we study into the classical form. We found that the numerical results we obtain for the new form are consistent with the previously established theory of the classical form of FHN model for the range of parameter values (especially small ε) for which the theory is valid.

In chapter 3, we analyzed wave solutions of a simplified calcium model which can be regarded as a representative model for a variety of models of intracellular dynamics. Based on numerical observations, it is conjectured that the existence of the CU bifurcation structure in calcium models is not dependent on there being complicated IP_3 receptors dynamics in the model. Therefore, we used algebraic functions rather than differential functions to describe the dynamics of IP_3 receptors as one of our simplifying steps. We performed a numerical bifurcation analysis of the prototypical calcium model. The persistence of the CU structure in this prototypical calcium model supports the conjecture that separation of different time scales between variables and the existence of a cubic-shaped critical manifold in its singular limit are the underlying mechanisms that give rise to the CU bifurcation structure in the calcium models. We studied the dynamics of the calcium model in the singular limit, and made some comparisons between the wave solutions in the singular limit and those in the full system, finding that homoclinic bifurcation and Hopf bifurcation curves of the full system arise as perturbations of singular homoclinic bifurcation and Hopf bifurcation curves. However, it is not yet known in detail how more complex features in the full system (e.g., homoclinic snaking) unfold from the singular limit.

In chapter 4, we compared the wave solutions in the FHN model and the prototypical calcium model. Even though the FHN model and the prototypical calcium model have very similar dynamical behaviour in the absence of spatial diffusion, they display some qualitative differences in the overall bifurcation structure in their singular limits. Specifically, the Hopf bifurcations are generally degenerate in the singular limit of the FHN model, while the Hopf bifurcations are generally not degenerate in the singular limit of calcium models. There are also differences between the homoclinic bifurcations in the singular limit between the FHN model and the calcium model due to the symmetry of the FHN system. However, these differences do not appear to significantly affect the dynamics associated with homoclinic bifurcations in the full systems. Since we find that the canonical FHN system does not capture all the basic features, we maintain that the FHN system should not be used as a prototypical model for understanding wave solutions of calcium models.

In chapter 5, we investigated some model reduction techniques commonly used to simplify biophysical systems and discussed some difficulties that may arise when computing the criticality of Hopf bifurcations in such systems. In particular, the quasi-steady state approximation and GSPT are often used to simplify biophysical systems with multiple time scales. The key idea of the quasi-steady state reduction is to set certain fast variables equal to their equilibrium values, which has the effect of replacing differential equations governing the evolution of such variables by algebraic equations. However, the approach is not in general mathematically justified. We give conditions under which this model reduction technique in a slow-fast system can be justified mathematically. Furthermore, we provide counterexamples to show that this technique may give misleading results near the onset of oscillatory behaviour, i.e., near Hopf bifurcations which play an important role in the overall dynamics of a physiological model.

We then showed that there are potential problems in applying GSPT to a slow-fast system when computing the criticality of Hopf bifurcations. In particular, we showed that the singular limit of the first Lyapunov coefficient of a Hopf bifurcation is not always equal to the first Lyapunov coefficient of the Hopf bifurcation in the corresponding fast subsystem. Consequently, one cannot deduce, in general, the criticality of a Hopf bifurcation from the lower-dimensional fast subsystem in a slow-fast system.

In chapter 6, we outlined a numerical scheme which is helpful for obtaining detailed numerical bifurcation results for some excitable systems. The numerical algorithm is based on Lin's theory (Lin, 1990) and was first developed in Krauskopf and Riess (2008). We discussed how to find the generic codimension-d ($d = 0, 1$) PtoP connection from a saddle periodic orbit to another saddle periodic orbit with Lin's approach. The key idea is to set up a boundary value problem that defines two separate orbit segments up to a specified cross section, where the end points of the orbit segments are restricted to lie in a well-defined d-dimensional space. The two orbit segments give rise to d smooth test functions, known as the Lin gaps. One can find a codimension-d PtoP connection in a systematic way by closing the Lin gaps in consecutive continuation runs. Then we illustrated Lin's method by finding a codimension-one heteroclinic cycle in a four-dimensional prototypical calcium model; this is the first example in which a non-structurally stable PtoP connection has been found in a physical model. We expect similar dynamics can be observed in other models of calcium dynamics.

In summary, we have studied the wave solutions of a number of excitable systems from the viewpoint of bifurcation analysis, mostly using numerical and analytical methods applied to travelling wave coordinates versions of the models of interest.

The work in this thesis has given rise to some possible directions for future work.

1. The existence and stability of solitary wave solutions of the prototypical calcium have been studied from a largely numerical point of view in this thesis. Attempts to prove results theoretically in the singular limit will be reported in Tsai et al. (2012), but it is not yet known how to extend the theoretical results to the non-singular case.

2. Solitary wave solutions with multiple pulses were shown to exist in the FHN

model, but little is known about the solitary wave solutions with multiple pulses in models of calcium dynamics. More work is required to understand the role of multiple pulse solitary waves in calcium models.

3. Some results about the validity of the quasi-steady state approximation were established in chapter 5, but there are outstanding issues to do with the effect of the quasi-steady state approximation on the dynamics of a model when the reduction method is not justified. For instance, how do the amplitude and frequency of periodic orbits created in a Hopf bifurcation in a model compare with the amplitude and frequency of the corresponding periodic orbit in a reduced model obtained by application of the quasi-steady state approximation?

4. In the FHN equations and the prototypical calcium model studied in chapters 2-4, we showed how the CU structure in the bifurcation set arose as a perturbation of a similar CU structure in the singular limit. More work is required to explain how complex features of the bifurcation set (e.g., EP1t points, PtoP heteroclinic cycles, etc.) in these systems unfold from the singular limit.

Appendix A

Parameters and formulae for model definitions

The following parameter values and function definitions were used in numerical integration of the Hodgkin-Huxley model, equations (5.5) in Section 5.2.1.

$$\begin{array}{lllll} \bar{E}_{Na} = 0.5 & \bar{E}_K = -0.77 & \bar{E}_L = -0.544 & \bar{g}_k = 0.3 & \bar{g}_l = 0.0025 \\ k_v = 100\,\mathrm{mV} & \varepsilon = 0.0083 & \tau_m = 1 & \tau_n = 1 & \tau_h = 1 \end{array}$$

$$\begin{array}{lll} a_n(v) = \frac{0.01(k_v v+55)}{1-\exp\left(-\frac{k_v v+55}{10}\right)} & a_m(v) = \frac{0.1(k_v v+40)}{1-\exp\left(-\frac{k_v v+40}{10}\right)} & a_h(v) = 0.07\exp\left(\frac{-k_v v-65}{20}\right) \\ b_n(v) = 0.125\exp\left(\frac{-k_v v-65}{80}\right) & b_m(v) = 4\exp\left(\frac{-k_v v-65}{18}\right) & b_h(v) = \frac{1}{\exp\left(\frac{-k_v v-35}{10}\right)+1} \\ n_\infty(v) = \frac{a_n(v)}{a_n(v)+b_n(v)} & m_\infty(v) = \frac{a_m(v)}{a_m(v)+b_m(v)} & h_\infty(v) = \frac{a_h(v)}{a_h(v)+b_h(v)} \\ t_n(v) = \frac{1}{a_n(v)+b_n(v)} & t_m(v) = \frac{1}{a_m(v)+b_m(v)} & t_h(v) = \frac{1}{a_h(v)+b_h(v)} \end{array}$$

Table A.1: Parameter values and function definitions for the Hodgkin-Huxley model, equations (5.5).

The following parameter values and function definitions were used in numerical integration of the Chay-Keizer model, equations (5.11) in Section 5.3.2.

$$\begin{array}{lll}
C_m = 1\,\mu\mathrm{F/cm}^2 & \bar{g}_{\mathrm{K,Ca}} = 0.09\,\mathrm{mS/cm}^2 & \bar{g}_K = 12\,\mathrm{mS/cm}^2 \\
\bar{g}_{\mathrm{Ca}} = 5\,\mathrm{mS/cm}^2 & \bar{g}_L = 0.04\,\mathrm{mS/cm}^2 & V_K = -75\,\mathrm{mV} \\
V_{\mathrm{Ca}} = 100\,\mathrm{mV} & V_L = -40\,\mathrm{mV} & V^* = 30\,\mathrm{mV} \\
V' = 50\,\mathrm{mV} & K_d = 1\,\mu\mathrm{M} & f = 0.004 \\
k_1 = 0.0275\,\mu\mathrm{Mcm}^2/\mathrm{nC} & k_c = 0.02\,\mathrm{ms}^{-1} &
\end{array}$$

$$\begin{array}{ll}
a_n(V+V^*) = 0.01\left(\frac{10-V-V^*}{\exp(\frac{10-V-V^*}{10})-1}\right) & b_n(V+V^*) = 0.125\exp\left(\frac{-V-V^*}{80}\right) \\
a_m(V+V') = 0.1\left(\frac{25-V-V'}{\exp(\frac{25-V-V'}{10})-1}\right) & b_m(V+V') = 4\exp\left(\frac{-V-V'}{18}\right) \\
a_h(V+V') = 0.07\exp\left(\frac{-V-V'}{20}\right) & b_h(V+V') = \frac{1}{\exp\left(\frac{40-V-V'}{10}\right)}
\end{array}$$

Table A.2: Parameter values and function definitions for the Chay-Keizer model, equations (5.11).

Glossary

ATP

Adenosine triphosphate

BVP

Boundary value problems

CICR

Calcium-induced calcium release

EP1t

A point of intersection between EtoP and PtoE tangency

ER

Endoplasmic reticulum

EtoP

A heteroclinic connection from an equilibrium to a periodic orbit

FHN

FitzHugh-Nagumo

GSPT

Geometric singular perturbation theory

HH

Hodgkin-Huxley

IP$_3$

Inositol $(1, 4, 5)$-trisphosphate

ODE

Ordinary differential equation

PDE

Partial differential equation

PtoE tangency

A heteroclinic connection from a periodic orbit to an equilibrium arising from the tangency between the stable manifold of the equilibrium and the unstable manifold of the periodic orbit

PtoP

A heteroclinic connection from one periodic orbit to another periodic orbit

SR

Sarcoplasmic reticulum

Bibliography

Aguirre, P., Doedel, E. J., Krauskopf, B., Osinga, H. M., 2011. Investigating the consequences of global bifurcations for two-dimensional invariant manifolds of vector fields. Discr. Contin. Dynam. Syst. – Series A 29, 1309–1344.

Atri, A., Amundson, J., Clapham, D., Sneyd, J., 1993. A single-pool model for intracellular calcium oscillations and waves in the Xenopous laevis oocyte. Biophys. J. 65, 1727–1739.

Baer, S. M., Erneux, T., 1986. Singular Hopf bifurcation to relaxation oscillations. SIAM J. Applied Math. 46, 721–739.

Baer, S. M., Erneux, T., 1992. Singular Hopf bifurcation to relaxation oscillations II. SIAM J. Applied Math. 52, 1651–1664.

Bai, Y., Edelmann, M., Sanderson, M. J., 2009. The contribution of inositol 1,4,5-trisphosphate and ryanodine receptors to agonist-induced Ca^{2+} signaling of airway smooth muscle cells. Am. J. Physiol. Lung Cell Mol. Physiol. 297, L347–361.

Bai, Y., Sanderson, M. J., 2006. Airway smooth muscle relaxation results from a reduction in the frequency of Ca^{2+} oscillations induced by a cAMP-mediated inhibition of the IP_3 receptor. Respir. Res. 7, 34.

Bautin, A., 1975. Qualitative investigation of a particular nonlinear system. Applied Mathematical Mechanics 39, 606–615.

Bautin, A., 1977. On the nonlocal application of the method of small parameter. Applied Mathematical Mechanics 41, 910–919.

Beck, M., Jones, C. K. R. T., Schaeffer, D., Wechselberger, M., 2008. Electrical waves in a one-dimensional model of cardiac tissue. SIAM J. Applied Dynamical Systems 7, 1558–1581.

Bell, D., Deng, B., 2002. Singular perturbation of N-front travelling waves in the FitzHugh-Nagumo equations. Nonlinear Analysis 3, 515–541.

Belyakov, L. A., 1980. Bifurcation of system with homoclinic curve of saddle-focus with saddle quantity zero. Mat. Zametki 28, 910–916.

Benoit, E., Callot, J., Diener, F., Diener, M., 1986. Chasse au canard. Collectanea Mathematica 23, 37–119.

Berne, R., Levy, M., Koeppon, B., Stanton, B., 2004. Physiology, 5th Edition. Elsevier Science.

Berridge, M., Galione, A., 1998. Cytosolic calcium oscillators. FASEB 2, 3074–3082.

Bers, D. M., 2002. Cardiac excitation-contraction coupling. Nature 415, 198–205.

Beyn, W. J., 1990. The numerical computation of connecting orbits in dynamical systems. IMA J. Numer. Anal. 10, 379–405.

Braaksma, B., 1998. Singular Hopf bifurcation in systems with fast and slow variables. J. Nonlinear Sci. 8, 457–490.

Champneys, A. R., Kirk, V., Knobloch, E., Oldeman, B., Rademacher, J., 2009. Unfolding a tangent equilibrium-to-periodic heteroclinic Cycle. SIAM J. Applied Dynamical System 8, 1261–1304.

Champneys, A. R., Kirk, V., Knobloch, E., Oldeman, B., Sneyd, J., 2007. When Shi'nikov meets Hopf in excitable systems. SIAM J. Applied Dynamical System 6, 663–693.

Champneys, A. R., Kuznetsov, Y. A., Sandstede, B., 1996. A numerical toolbox for homoclinic bifurcation analysis. Int. J. Bifurc. Chaos 6, 867–887.

Chay, T. R., Keizer, J., 1983. Minimal model for membrane oscillations in the pancreatic β-cell. Biophys. J. 42, 181–190.

Colegrove, S. L., Albrecht, M. A., Friel, D. D., 2000. Quantitative analysis of mitochondrial Ca^{2+} uptake and release pathways in sympathetic neurons. Reconstruction of the recovery after depolarization-evoked $[Ca^{2+}]_i$ elevations. J. Gen. Physiol. 115, 371–388.

Constantin, J., Charles, A., 1999. Spontaneous action potentials initiate rhythmic intercellular calcium waves in immortalized hypothalamic (GT1-1) neurons. J. Neurophysiol. 82, 429–435.

Crank, J., Nicolson, P., 1947. A practical method for numerical evaluation of solutions of partial differential equations of the heat conduction type. Proc. Camb. Phil. Soc. 43, 50–67.

Deng, B., 1991. The existence of infinitely many travelling front and back waves in the FitzHugh-Nagumo equations. SIAM J. Math. Anal. 22, 1631–1650.

Deng, B., Sakamoto, K., 1995. Shil'nikov-Hopf bifurcation. J. Differential Equations 119, 1–23.

Dieci, L., Rebaza, J., 2004. Point-to-periodic and periodic-to-periodic connections. BIT Numerical Mathematics 44, 41–62.

Doedel, E. J., Friedman, M. J., 1989. Numerical computation of heteroclinic orbits. J. Comput. Appl. Math. 26, 155–170.

Doedel, E. J., Kooi, B. W., Kuznetsov, Y. A., Voorn, G. A. K., 2008. Continuation of connecting orbits in 3D-ODES: (I) : point-to-cycle connections. Int. J. Bifurc. Chaos 18, 1889–1903.

Doedel, E. J., Kooi, B. W., van Voorn, G. A. K., Kuznetsov, Y. A., 2009. Continuation of connecting orbits in 3D-ODES (II) : cycle-to-cycle connections. Int. J. Bifurc. Chaos, 159–169.

Doedel, E. J., Krauskopf, B., Osinga, H. M., 2006. Global bifurcations of the Lorenz manifold. Nonlinearity 19, 2947–2972.

Doedel, E. J., Paffenroth, R. C., Champneys, A. R., Fairgrieve, T. F., Kuznetsov, Y. A., Oldeman, B. E., Sandstede, B., Wang, X. J., Zhang, C., 2007. AUTO07P: Continuation and bifurcation software for ordinary differential equations. Technical Report.

Domijan, M., Murray, R., Sneyd, J., 2006. Dynamical probing of the mechanisms underlying calcium oscillations. J. Nonlinear Sci. 16, 483–506.

Evans, J. W., Fenichel, N., Feroes, J. A., 1982. Double impulse solutions in nerve axon equations. SIAM J. Applied Math. 42, 219–234.

Evans, J. W., Feroe, J., 1977. Local stability theory of the nerve impulse. Math. Biosci. 37, 23–50.

Evans, R. L., Park, K., Turner, R. J., Watson, G. E., Nguyen, H. V., Dennett, M. R., Hand, A. R., Flagella, M., Shull, G. E., Melvin, J. E., 2000. Severe impairment of salivation in $Na^+/K^+/2Cl^-$-cotransporter (NKCC1)-deficient mice. J. Biol. Chem. 275, 26720–26726.

Falcke, M., 2004. Reading the patterns in living cells. Advances in Physics 53, 255–440.

Feng, Z. S., 2002. On explicit exact solutions to the compound Burgers-KdV equations. Phys. Lett. 293, 57–66.

Fenichel, N., 1979. Geometric singular perturbation theory. J. Differential Equations 31, 53–98.

Fitzhugh, R., 1961. Impulses and physiological states in theoretical models of nerve membrane. Biophys. J. 1, 445–446.

Franzini-Armstrong, C., Protasi, F., Ramesh, V., 1999. Shape, size, and distribution of Ca^{2+} release units and couplons in skeletal and cardiac muscles. Biophys. J. 77, 1528–1539.

Friedman, M., Doedel, E. J., 1993. Computational methods for global analysis of homoclinic and heteroclinic orbits: a case study. J. Dyn. and Diff. Eq. 5, 37–57.

Gin, E., Crampin, E. J., Brown, D. A., Shuttleworth, T. J., Yule, D. I., Sneyd, J., 2007. A mathematical model of fluid secretion from a parotid acinar cell. J. Theor. Biol. 248, 64–80.

Gin, E., Falcke, M., Wagner, L. E., Yule, D. I., Sneyd, J., 2009. A kinetic model of the inositol trisphosphate receptor based on single-channel data. Biophys. J. 96, 4053–4062.

Giovannucci, D. R., Sneyd, J., Groblewski, G. E., Yule, D. I., 2000. Targeted phosphorylation of inositol 1,4,5-trisphosphate receptors selectively inhibits localized Ca^{2+} release and shapes oscillatory Ca^{2+} signals. J. Biol. Chem. 275, 33704–33711.

Goel, P., Sneyd, J., Friedman, A., 2006. Homogenization of the cell cytoplasm: the calcium bidomain equations. Multiscale Model. Simul. 5, 1045–1062.

Govaerts, W., Kuznetsov, Y. A., 2008. Matcont. Technical report.

Grubelnik, V., Larsen, A. Z., Kummer, U., Olsen, L. F., Marhl, M., 2001. Mitochondria regulate the amplitude of simple and complex calcium oscillations. Biophysical Chemistry 94, 59–74.

Guckenheimer, J., 2008. Singular Hopf bifurcation in systems with two slow variables. SIAM J. Applied Dynamical System 7, 1335–1377.

Guckenheimer, J., Holmes, P., 1983. Nonlinear oscillations, dynamical systems, and bifurcation of vector fields. Springer-Verlag, New York.

Guckenheimer, J., Kuehn, C., 2009. Homoclinic orbits of the FitzHugh-Nagumo equation: the singular-limit. Discr. Contin. Dynam. Syst. – Series S 2, 851–872.

Guckenheimer, J., Osinga, H. M., 2012. The singular limit of a Hopf bifurcation. Discr. Contin. Dynam. Syst. – Series A, in press.

Harvey, E., Kirk, V., Sneyd, J., Wechselberger, M., 2010. Multiple time scales, mixed-mode oscillations and canards in models of intracellular calcium dynamics. Chaos 20, 045104.

Harvey, E., Kirk, V., Sneyd, J., Wechselberger, M., 2011. Understanding anomalous delays in a model of intracellular calcium dynamics. J. Nonlinear Sci. 21, 639–683.

Higgins, E. R., Goel, P., Puglisi, J. L., Bers, D. M., Cannell, M., Sneyd, J., 2007. Modelling calcium microdomains using homogenisation. J. Theor. Biol. 247, 623–644.

Hirschberg, P., Knobloch, E., 1993. Shil'nikov-Hopf bifurcation. Physica D 62, 202–216.

Hodgkin, A. L., Huxley, A. F., 1952a. Currents carried by sodium and potassium ions through the membrane of the giant axon of Loligo. J. Physiol. 116, 449–472.

Hodgkin, A. L., Huxley, A. F., 1952b. A quantitative description of membrane current and its application to conduction and excitation in nerve. J. Physiol. 116, 507–544.

Hodgkin, A. L., Huxley, A. F., 1952c. The components of membrane conductance in the giant axon of Loligo. J. Physiol. 116, 473–496.

Hodgkin, A. L., Huxley, A. F., 1952d. The dual effect of membrane potential on sodium conductance in the giant axon of Loligo. J. Physiol. 116, 497–506.

Jones, C. K. R. T., 1984. Stability of the travelling wave solution of the FitzHugh-Nagumo system. Trans. Amer. Math. Soc. 286, 431–469.

Jones, C. K. R. T., Kopell, N., Langer, R., 1991. Construction of the Fitzhugh-Nagumo pulse using differential forms. IMA Vol. Math. Appl. 37, 101–115.

Keener, J., Sneyd, J., 2008. Mathematical physiology, 2nd Edition. Springer-Verlag, New York.

Knobloch, J., 2000. Lin's method for discrete dynamical systems. J. Difference Equations and Applications 6, 577–623.

Knobloch, J., Riess, T., 2010. Lin's method for heteroclinic chains involving periodic orbits. Nonlinearity 23, 23–54.

Krauskopf, B., Osinga, H. M., Galan-Vioque, J., 2007. Numerical continuation methods for dynamical systems. Springer-Verlag, New York.

Krauskopf, B., Riess, T., 2008. A Lin's method approach to finding and continuing heteroclinic connections involving periodic orbits. Nonlinearity 21, 1655–1690.

Krupa, M., Sandstede, B., Szmolyan, P., 1997. Extending geometric singular perturbation theory to nonhyperbolic points - fold and canard points in two dimensions. J. Differential Equations 133, 49–97.

Kuznetsov, Y. A., 1998. Elements of applied bifurcation theory, 2nd Edition. Springer-Verlag, New York.

Kuznetsov, Y. A., Feo, O. D., Rinaldi, S., 2001. Belyakov homoclinic bifurcations in a tritrophic food chain model. SIAM J. Applied Math., 462–487.

LeBeau, A. P., Yule, D. I., Groblewski, G. E., Sneyd, J., 1999. Agonist-dependent phosphorylation of the inositol 1,4,5-trisphosphate receptor: A possible mechanism for agonist-specific calcium oscillations in pancreatic acinar cells. J. Gen. Physiol. 113, 851–872.

Lee, K., Duan, W., Sneyd, J., Herbison, A. E., 2010. Two slow calcium-activated afterhyperpolarization currents control burst firing dynamics in gonadotropin-releasing hormone neurons. J. Neurosci. 30, 6214–6224.

Li, H., Guo, Y., 2006. New exact solutions to the Fitzhugh-Nagumo equation. Applied Mathematics and Computation 180, 524–528.

Lin, X. B., 1990. Using Melnikov's method to solve Shilnikov's problems. Proc. R. Soc. Edinb. 116, 295–325.

Lodish, H., Berk, A., Matsudaira, P., Kaiser, C. A., Krieger, M., Scott, M. P., Zipursky, L., Darnell, J., 2003. Molecular cell biology, 5th Edition. W. H. Freeman.

Mckean, H. P., 1970. Nagumo's equations. Advances in Mathematics 4, 209–233.

Nagumo, J. S., Arimoto, S., Yoshizawa, S., 1962. An active pulse transmission line stimulating nerve axon. Proc. IRE 50, 2061–2070.

Palk, L., Sneyd, J., Shuttleworth, T. J., Yule, D. I., Crampin, E. J., 2010. A dynamical model of saliva secretion. J. Theor. Biol. 266, 625–640.

Pampel, T., 2001. Numerical approximation of connecting orbits with asymptotic rate. Numerische Mathematik 90, 309–348.

Pate, E., 2005. Mathematical analysis of the generation of force and motion in contracting muscle. In: Sneyd, J. (Ed.), Tutorials in mathematical biosciences II. mathematical modeling of calcium dynamics and signal transduction. Lecture Notes in Mathematics. Springer-Verlag, pp. 133–152.

Perez, J. F., Sanderson, M. J., Jun 2005a. The contraction of smooth muscle cells of intrapulmonary arterioles is determined by the frequency of Ca^{2+} oscillations induced by $5-\mathrm{HT}$ and KCl. J. Gen. Physiol. 125, 555–567.

Perez, J. F., Sanderson, M. J., Jun 2005b. The frequency of calcium oscillations induced by $5-\mathrm{HT}$, ACH, and KCl determine the contraction of smooth muscle cells of intrapulmonary bronchioles. J. Gen. Physiol. 125, 535–553.

Politi, A. Z., Donovan, G. M., Tawhai, M. H., Sanderson, M. J., Lauzon, A. M., Bates, J. H., Sneyd, J., 2010. A multiscale, spatially distributed model of asthmatic airway hyper-responsiveness. J. Theor. Biol. 266, 614–624.

Rademacher, J. D. M., 2005. Homoclinic orbits near heteroclinic cycles with one equilibrium and one periodic orbit. J. Differential Equations 218, 390–443.

Rinzel, J., 1978. On repetitive activity in nerve. Federation Proceedings 37, 2793–2802.

Rinzel, J., 1985. Excitation dynamics: insights from simplified membrane models. Federation Proceedings 44, 2944–2946.

Rinzel, J., Lee, Y. S., 1986. On different mechanisms for membrane potential bursting. In: Othmer, H. G. (Ed.), Lecture Notes in Biomathematics. Springer-Verlag.

Rocsoreanu, C., Georgescu, A., Giurgiteanu, N., 2000. The FitzHugh-Nagumo model - bifurcation and dynamics. Kluwer.

Romeo, M. M., Jones, C. K. R. T., 2003. The stability of travelling calcium pulses in a pancreatic acinar cell. Physica D 177, 242–258.

Rooney, T. A., Thomas, A. P., 1993. Intracellular calcium waves generated by $\mathrm{Ins}(1,4,5)P_3$-dependent mechanisms. Cell Calcium 14, 674–690.

Rottingen, J., Iversen, J. G., 2000. Ruled by waves? Intracellular and intercellular calcium signalling. Acta Physiologica Scandinavica 169, 203–219.

Rubin, J., Wechselberger, M., 2007. Giant squid - hidden canard: the 3D geometry of the Hodgkin-Huxley model. Biological Cybernetics 97, 5–32.

Rubin, J., Wechselberger, M., 2008. The selection of mixed-mode oscillations in a Hodgkin-Huxley model with multiple timescales. Chaos 18, 015105.

Sneyd, J., 2005. Modeling IP_3-dependent calcium dynamics in non-excitable cells. In: Sneyd, J. (Ed.), Tutorials in mathematical biosciences II. mathematical modeling of calcium dynamics and signal transduction. Lecture Notes in Mathematics. Springer-Verlag, pp. 15–61.

Sneyd, J., Dufour, J. F., 2002. A dynamic model of the type-2 inositol trisphosphate receptor. Proc. Natl. Acad. Sci. 99, 2398–2403.

Sneyd, J., Tsaneva-Atanasova, K., Bruce, J. I. E., Straub, S. V., Giovannucci, D. R., Yule, D. I., 2003. A model of calcium waves in pancreatic and parotid acinar cells. Biophys. J. 85, 1392–1405.

Sneyd, J., Tsaneva-Atanasova, K., Reznikov, V., Bai, Y., Sanderson, M. J., Yule, D. I., 2006. A method for determining the dependence of calcium oscillations on inositol triphosphate oscillations. Proc. Natl. Acad. Sci. U.S.A. 103, 1675–1680.

Sneyd, J., Tsaneva-Atanasova, K., Yule, D. I., Thompson, J. L., Shuttleworth, T. J., 2004. Control of calcium oscillations by membrane fluxes. Proc. Natl. Acad. Sci. U.S.A. 101, 1392–1396.

Spergel, D., Kruth, U., Hanley, D., Sprengel, R., Seeburg, P., 1999. GABA- and glutamate-activated channels in green fluorescent protein-tagged gonadotropin-releasing hormone neurons in transgenic mice. J. Neurophysiol. 19, 2037–2050.

Stephens, N. L., 2001. Airway smooth muscle. Lung 179, 333–373.

Szmolyan, P., Wechselberger, M., 2001. Canards in R^3. J. Differential Equations.

Toyoshima, C., Nakasako, M., Nomura, H., Ogawa, H., 2000. Crystal structure of the calcium pump of sarcoplasmic reticulum at 2.6 A resolution. Nature 405, 647–655.

Tsai, J. C., Zhang, W., Kirk, V., Sneyd, J., 2012. Travelling waves in a simplified model of calcium dynamics, submitted.

Wang, I., Bai, Y., Sanderson, M. J., Sneyd, J., 2010. A mathematical analysis of agonist- and KCl-induced Ca^{2+} oscillations in mouse airway smooth muscle cells. Biophys. J. 98, 1170–1181.

Wang, I., Politi, A. Z., Tania, N., Bai, Y., Sanderson, M. J., Sneyd, J., 2008. A mathematical model of airway and pulmonary arteriole smooth muscle. Biophys. J. 94, 2053–2064.

Winslow, R. L., Hinch, R., Greenstein, J. L., 2005. Mechanisms and models of cardiac excitation-contraction coupling. In: Sneyd, J. (Ed.), Tutorials in mathematical biosciences II. mathematical modeling of calcium dynamics and signal transduction. Lecture Notes in Mathematics. Springer-Verlag.

Yanagida, E., 1985. Stablity of fast travelling wave solutions of the FitzHugh-Nagumo equations. J. Math. Biol. 22, 85–104.

Yew, A. C., 2001. Multipulses of nonlinearly-coupled Schrodinger equations. J. Differential Equations 173, 92–137.

Zhang, W., Kirk, V., Sneyd, J., Wechselberger, M., 2011. Changes in the criticality of Hopf bifurcations due to certain model reduction techniques in systems with multiple timescales. J. Mathematical Neuroscience 1:9.

Zhang, W., Krauskopf, B., Kirk, V., 2012. Continuation of a codimension-one heteroclinic cycle between two periodic orbits in an intracellular calcium model. Discr. Contin. Dynam. Syst. – Series A, in press.